UNIVERSIDAD DE JAÉN

ESCUELA POLITÉCNICA SUPERIOR DE JAÉN

DEPARTAMENTO DE INGENIERÍA MECÁNICA Y MINERA

TESIS DOCTORAL

BUBBLE FORMATION AND RISING DYNAMICS ANALYSES

PRESENTADA POR:

JOSÉ CARLOS CANO LOZANO

DIRIGIDA POR:

DR. D. CARLOS MARTÍNEZ BAZÁN

JAÉN, 6 DE NOVIEMBRE DE 2015

ISBN 978-84-8439-992-6

UNIVERSIDAD DE JAÉN

Bubble formation and rising dynamics analyses

Tesis Doctoral

Autor
José Carlos Cano Lozano

Director
Prof. Carlos Martínez Bazán

Jaén, Noviembre 2015

DEPARTAMENTO DE INGENIERÍA MECÁNICA Y MINERA
Escuela Politécnica Superior

Bubble formation and rising dynamics analyses

Análisis de la formación de burbujas y de la dinámica de su ascensión

Autor
José Carlos Cano Lozano

Director de Tesis
Prof. Carlos Martínez Bazán

Jaén, Noviembre 2015

A mis padres

El hombre de ciencia no aspira a un resultado inmediato. No espera que sus avanzadas ideas estén listas para ser asumidas. Su trabajo es como el del sembrador: para el futuro. Su deber es poner cimientos para los que están por venir y señalar el camino.
Nikola Tesla.

La gente que me gusta

Me gusta la gente que vibra, que no hay que empujarla, que no hay que decirle que haga las cosas, sino que sabe lo que hay que hacer y que lo hace en menos tiempo de lo esperado.

Me gusta la gente con capacidad para medir las consecuencias de sus acciones, la gente que no deja las soluciones al azar.

Me gusta la gente estricta con su gente y consigo misma, pero que no pierda de vista que somos humanos y nos podemos equivocar.

Me gusta la gente que piensa que el trabajo en equipo, entre amigos, produce más que los caóticos esfuerzos individuales.

Me gusta la gente que sabe la importancia de la alegría.

Me gusta la gente sincera y franca, capaz de oponerse con argumentos serenos y razonables.

Me gusta la gente de criterio, la que no se avergüenza de reconocer que no sabe algo o que se equivocó.

Me gusta la gente que al aceptar sus errores, se esfuerza genuinamente por no volver a cometerlos.

Me gusta la gente capaz de criticarme constructivamente y de frente; a estos los llamo mis amigos.

Me gusta la gente fiel y persistente, que no fallece cuando de alcanzar objetivos e ideas se trata.

Me gusta la gente que trabaja por resultados. Con gente como ésa, me comprometo a lo que sea, ya que con haber tenido esa gente a mi lado me doy por bien retribuido.

Mario Benedetti.

Tesis doctoral

Bubble formation and rising dynamics analyses

Autor: José Carlos Cano Lozano

Director de Tesis:
Prof. Carlos Martínez Bazán

Firma del Tribunal Calificador:

Firma

Presidente: Devaraj van der Meer
Vocal: José Manuel Gordillo Arias de Saavedra
Secretario: Rocío Bolaños Jiménez
Suplente: Guillaume Maurice Riboux
Suplente: Javier Rodríguez Rodríguez

Calificación:

Jaén, de Noviembre de 2015

Agradecimientos

A lo largo de las siguientes líneas me gustaría agradecer a todas aquellas personas que me han ayudado y enriquecido académica y personalmente durante estos años. Sin todos y cada uno de Vosotros, hoy no estaría escribiendo estos agradecimientos que me hacen consciente de que estoy alcanzando la meta.

En primer lugar, quiero dedicar unas palabras a la persona que supo despertar en mí la curiosidad por una de las ramas más complejas, pero a la vez más gratificantes que he encontrado a lo largo de mi carrera universitaria, mi *maestro* de Mecánica de Fluidos, Carlos Martínez. Gracias por tus clases, tu dedicación, tus innumerables aportaciones a este trabajo y tus aclaraciones a todas aquellas dudas que han surgido a lo largo de estos cortos, pero intensos años. Me ha encantado trabajar codo con codo contigo, y más aún, que hayas sido, como director de esta tesis, la persona que me ha iniciado en el mundo de la investigación, dando siempre buenos consejos y mostrándome el camino correcto.

Dentro de esta pequeña gran familia que es la Universidad, tengo que agradecer también a los que comenzaron siendo mis compañeros del LAB-913 y, a día de hoy, considero mis amigos/as. Muchas gracias Rocío y José Ignacio, por todos los momentos que hemos compartido juntos. Me ha encantado, me encanta y seguirá encantándome discutir de ciencia con vosotros (y de otras muchas cosas). Rocío, si miro atrás en el tiempo, me doy cuenta de que tu ayuda estuvo ahí desde el inicio, hasta tal punto que te he sentido como una codirectora, además de un referente. Llegado este punto, no puedo más que darte las gracias. Las mismas gracias que merece José Ignacio. No podría haber tenido un mejor compañero de laboratorio. He disfrutado mucho trabajando contigo y admirando el trabajo que realizas a diario. Asimismo, en este grupo no puedo olvidar a mi amigo Cosme, nuestro técnico. Muchas gracias por tu paciencia ante todos los retos experimentales que te propuse y, sobre todo, por estar disponible para ayudarme en todo momento. Me ha encantado dialogar contigo acerca del procedimiento a seguir para llevar a cabo las tareas, lo que en muchas ocasiones me ha ayudado a clarificar mis ideas.

En general, a todos los miembros del grupo de investigación de Mecánica de Fluidos, por aguantar mis quejas y por vuestro ánimo y apoyo continuo, sobre todo en estas últimas semanas especialmente intensas. En primer lugar, quisiera agradecer a mi compañero y amigo Cándido su participación en parte de esta tesis y reconocer su esfuerzo y dedicación a la misma, además de intentar siempre despertar una sonrisa por medio de un buen chiste, lo que sin duda alguna ayuda en ciertos momentos. A Javi y Manu, a quienes tengo que reconocer su colaboración en el laboratorio para realizar los experimentos. Igualmente, gracias por hacerme recordar mis inicios, la ilusión del comienzo y darme impulso en esta última etapa.

No puedo olvidarme de Javier, Alejandro y José Manuel, que han acrecentado mi motivación e interés por el tema gracias a sus charlas sobre las teorías, experiencias, anécdotas, y curiosidades que envuelven este mundo de la Mecánica de Fluidos. Agradecerles a ellos y a Carlos que pen-

saran en mí para realizar las simulaciones del Annual Review. Igualmente, no puedo dejar de estar agradecido a los compañeros de la Universidad Carlos III: Elena, Mariano, Wil y Ana, entre otros, con los que he disfrutado de grandes experiencias durante los congresos y workshops.

Quiero expresar mi más sincera gratitud a Jacques Magnaudet, por mostrar un gran interés en el trabajo que he realizado, además de haberme permitido trabajar y colaborar con él en el Institut de Mécanique des Fluides de Toulouse (IMFT) durante estos años. A Joël, por la gran ayuda que me brindó, tanto a nivel personal como profesional, durante mis estancias en Toulouse.

A todo el equipo técnico que ha intervenido en algún momento en esta tesis: al técnico del departamento, Agustín, y al personal del Centro de Servicios de Informática y Redes de Comunicaciones (CSIRC) de la Universidad de Granada (UGR), por permitir que realizase gran parte de las simulaciones en el clúster ALHAMBRA.

Habiendo expresado mi gratitud a todas aquellas personas que he conocido a lo largo de estos años y han contribuido a mi desarrollo académico, es el turno de dedicar unas palabras a mis personas más cercanas.

Me gustaría agradecer a nivel personal a Mi Familia por el apoyo que me han brindado en todo aquello que me he propuesto en mi vida. A mis padres, por su entrega y sacrificio para darme la mejor educación, inculcándome desde la niñez el valor de la constancia y la filosofía del trabajo diario. Gracias por haberme escuchado en todo momento y aconsejado siempre lo mejor para mí. A mi hermano, por estos años en la Universidad que me han permitido estar más unido a tí, disfrutando inmensamente de nuestras largas charlas, discusiones políticas, descubrimientos arqueológicos y más de una carcajada. Además, no puedo dejar de reconocer a mi tío Cristóbal su apoyo y consejos durante esta etapa de mi vida. Sin duda, su experiencia y pasión por el mundo de la investigación me han animado a recorrer con ilusión este largo camino.

Por último, por ser lo mas importante para mí, a mi princesa Beatriz. Muchas gracias por tu inmensa paciencia, escucha, comprensión, ayuda diaria y esfuerzo por intentar alegrarme en los malos momentos. Pero, sobre todo, por compartir experiencias y momentos inolvidables a lo largo de todos estos años, tanto a nivel académico como personal. Por estar ahí siempre que te he necesitado y enseñarme el valor de la incondicionalidad, simplemente GRACIAS.

Resumen

Actualmente, los sistemas multifásicos, en especial aquellos en los que aparecen burbujas, son ampliamente utilizados en gran variedad de procesos industriales. Con el desarrollo de la nanotecnología, la aplicabilidad de dichos sistemas ha aumentado considerablemente extendiéndose a otros campos tecnológicos como la medicina. No obstante, sigue siendo necesario profundizar en el estudio de los procesos físicos que rigen la formación y posterior ascensión de las burbujas para poder entender completamente el comportamiento hidrodinámico, y por consiguiente, conseguir una mejora del funcionamiento de dichos sistemas, aumentando su eficiencia.

Así, la primera parte de esta Tesis se centra en la formación de burbujas, en especial en la formación bajo condiciones mixtas de caudal y presión, es decir, mediante la ayuda de una cámara de gas de tamaño medio para no incurrir en condiciones de caudal o presión constantes. Bajo esta premisa, se ha llevado a cabo un estudio analítico y experimental de dicha formación desde agujas sumergidas en posición vertical, lo cual ha sido poco estudiado hasta el momento, centrándose los estudios previos en sistemas a caudal o presión constante. El análisis de los experimentos ha permitido conocer y modelar la variación temporal de la presión en el interior de la cámara de inyección. Es importante destacar la incorporación al modelo de la evolución del menisco en el interior de la aguja, como consecuencia de la columna de líquido que penetra en la aguja durante el proceso de formación para ayudar a presurizar la cámara. Además, se ha analizado la evolución del tamaño y forma de las burbujas producidas durante el proceso.

La segunda parte está centrada en el estudio numérico del ascenso de burbujas en líquidos en reposo en función de las propiedades de los fluidos y del tamaño de la propia burbuja. Inicialmente, se ha realizado un extenso estudio del estado del arte en relación a dicho fenómeno, obteniendo una correlación que permite identificar si el movimiento es estable o inestable, determinando el punto de transición. Seguidamente, se han analizado distintas técnicas numéricas para rastrear la entrefase, así como los códigos de libre acceso existentes en la actualidad, para determinar la opción más idónea y ajustada al estudio a realizar, decidiéndose por la técnica Volume of Fluid (VOF) implementada en el código Gerris Flow Solver, que conserva la masa y evita la formación de corrientes espurias como principales ventajas. A continuación se han realizado simulaciones bidimensionales axisimétricas de las cuales se ha obtenido información de la forma real de la burbuja, así como del campo de presiones y velocidades. Complementariamente, se ha examinado la influencia del gas interior en el comportamiento de la burbuja. Al mismo tiempo, estos resultados han posibilitado el estudio del efecto de la forma de la burbuja en el desarrollo tridimensional de la estela durante la transición, por medio de simulaciones del flujo exterior, fijando la forma de la burbuja. Por último, se han realizado simulaciones tridimensionales, permitiendo la deformación de la burbuja durante el movimiento ascendente. Los resultados numéricos han servido para caracterizar la evolución de la forma de la burbuja y la trayectoria descrita durante su ascensión, así como la evolución de las estructuras vorticales que se forman en la estela, permitiendo clasificar y definir la transición de las burbujas desde el punto de vista de la estabilidad. Durante este estudio se han reportado nuevos modos de inestabilidad no observados previamente en burbujas, pero que

presentan similitud con los descritos en inestabilidades de cuerpos sólidos.

Adicionalmente, se ha realizado un Análisis de Estabilidad Lineal (LSA, Linear Stability Analysis) considerando la forma real de las burbujas y su velocidad terminal de ascensión, obtenidas por medio de las simulaciones bidimensionales axisimétricas. Dicho análisis se ha llevado a cabo por medio del código FreeFem++. Los resultados obtenidos permiten comparar la curva neutra de transición con los resultados numéricos anteriormente mencionados, así como realizar un análisis de la influencia de la forma de burbuja en la estabilidad de la misma.

Los resultados presentados en esta memoria están recogidos parcialmente o en su totalidad en las siguientes publicaciones:

- **Publicación 1.** J.C. Cano-Lozano, P. Bohorquez and C. Martínez-Bazán, 2013. Wake instability of a fixed axisymmetric bubble of realistic shape. *Int. J. Multiphase Flow* **51**, 11-21.
- **Publicación 2.** J.C. Cano-Lozano, R. Bolaños-Jiménez, C. Gutiérrez-Montes and C. Martínez-Bazán, 2015. The use of Volume of Fluid technique to analyze multiphase flows: Specific case of bubble rising in still liquids. *Appl. Math. Model.* **39**, 3290-3305.
- **Publicación 3.** J.C. Cano-Lozano, C. Gutiérrez-Montes and C. Martínez-Bazán, 2015. Influence of gas chamber conditions on the formation of bubbles from a submerged vertical needle. Enviado al *Int. J. Heat Mass Transfer.*
- **Publicación 4.** J.C. Cano-Lozano, J. Tchoufag, J. Magnaudet and C. Martínez-Bazán, 2015. A global stability approach to wake and path instabilities of rising bubbles with a fore-aft asymmetric shape. Enviado al *Phys. Fluids.*
- **Publicación 5.** J.C. Cano-Lozano, C. Martínez-Bazán, J. Tchoufag and J. Magnaudet, 2015. Wakes and paths of bubbles with fore-aft asymmetry. En preparación para ser enviado al *Phys. Fluids.*

Palabras clave: Formación de burbujas, paradoja de Leonardo, ascensión de burbujas, forma de la burbuja, estabilidad de estelas.

Abstract

Nowadays, multiphase systems, particularly those interacting with bubbles, are widely used in many industrial processes. With the development of nanotechnology, the applicability of these systems has significantly increased and is being extended to other technological fields such as medicine, among others. However, a further analysis of the physical processes, including the bubble dynamics, is still required for a complete understanding of their behavior and, consequently, to improve the performance and efficiency of bubbly systems.

The first part of this dissertation focuses on the formation of bubbles, especially on their generation under mixed conditions in terms of gas injection flow rate and feeding pressure (bubble formation through the use of a gas chamber where neither the gas flow rate nor the chamber pressure remain constant during the bubbling process). Under this premise, an analytical and experimental study of the formation of bubbles from vertical submerged needles connected to a gas chamber has been conducted, a configuration very little explored since previous studies have been mainly focused on the formation of bubbles from a submerged orifice under either constant flow rate or constant pressure. The analysis of the results has allowed us to model the time evolution of the pressure inside the injection chamber. It is important to emphasize the inclusion to the model of the effect of the evolution of the water column penetrating inside the needle during bubble generation process; a phenomenon that contributes to the pressurization of the chamber. Moreover, the evolution of the size and shape of the bubbles produced has also been assessed.

The second part of the dissertation is focused on the numerical study of bubbles rising in stagnant liquids, and its dependence on the fluids properties and the bubble size. Initially, the state of the art of this phenomenon has been revisited, obtaining a correlation that identifies whether the bubbles ascending motion is stable or unstable and determines the transition point. Next, different techniques to track the interface have been analyzed, as well as, open-access codes, to determine which of them show the best results for this study. The Volume of Fluid (VOF) technique implemented in the Gerris Flow Sover software was chosen since it preserves mass conservation and avoids the formation of spurious currents, among other reasons. Then, two-dimensional axisymmetric simulations have been carried out obtaining information about bubble shape, as well as, the velocities and pressure fields. Additionally, the influence of the gas properties has been considered in the behavior condition. At the same time, these results have allowed to analyze how the bubble shape affects to the three-dimensional development of the wake during the transition through the use of simulations of the outer flow, setting the real shape of the bubble. Finally, three-dimensional Direct Numerical Simulations (DNS) have been performed, allowing the deformation of the bubble as it rises. The three-dimensional results have allowed us to observe the evolution of the shape, the path described by the bubble, and the evolution of the vortical structures developed in the wake, thus allowing to classify and define the transition from the stability point of view. It is worth noting that new modes of instability have been observed which, in some cases, share similarities with those observed in solid bodies.

Additionally, a global Linear Stability Analysis (LSA) has been conducted with FreeFem++ code, considering the actual shape of the bubbles and their terminal velocity, being both obtained through the axisymmetric two-dimensional simulations. The results have permitted us to compare the neutral curves obtained from the Direct Numerical Simulations and the stability analyses, as well as to perform a detailed study of the influence of the bubble shape on the stability of the established wake and and bubble trajectory.

The results presented in this dissertation are partially or totally comprised in the following publications:

- **Paper 1.** J.C. Cano-Lozano, P. Bohorquez and C. Martínez-Bazán, 2013. Wake instability of a fixed axisymmetric bubble of realistic shape. *Int. J. Multiphase Flow* **51**, 11-21.
- **Paper 2.** J.C. Cano-Lozano, R. Bolaños-Jiménez, C. Gutiérrez-Montes and C. Martínez-Bazán, 2015. The use of Volume of Fluid technique to analyze multiphase flows: Specific case of bubble rising in still liquids. *Appl. Math. Model.* **39**, 3290-3305.
- **Paper 3.** J.C. Cano-Lozano, C. Gutiérrez-Montes and C. Martínez-Bazán, 2015. Influence of gas chamber conditions on the formation of bubbles from a submerged vertical needle. Submitted to the *Int. J. Heat Mass Transfer.*
- **Paper 4.** J.C. Cano-Lozano, J. Tchoufag, J. Magnaudet and C. Martínez-Bazán, 2015. A global stability approach to wake and path instabilities of rising bubbles with a fore-aft asymmetric shape. Submitted to the *Phys. Fluids.*
- **Paper 5.** J.C. Cano-Lozano, C. Martínez-Bazán, J. Tchoufag and J. Magnaudet, 2015. Wakes and paths of bubbles with fore-aft asymmetry. Under preparation to be submitted to the *Phys. Fluids.*

Keywords: Bubble formation, Leonardo's paradox, bubble rising, bubble shape, stability wake.

Contents

List of Tables

List of Figures

CHAPTER
ONE

Introduction

1.1 Motivation

Bubble formation, analyses of bubbly flows and gas-liquid contact line description are examples in which it is important to understand the dynamics of interfaces owing to their relevance in a great number of current applications. In general, bubbles are employed in many industrial processes, such as mineral purification by flotation, gas-liquid contactors and absorbers in the chemical industry by means of bubble columns reactors [152], water treatment by aeration of chemical and biological reactors, diffusers and induced gas flotation [120], as well as in several applications in the pharmaceutical and food industries, among many others. In addition, new developments and innovative implementations are also emerging based on multiphase systems, for instance, bubbles might be used to reduce the drag of ships [21, 72]. In this regard, the injection of bubbles along the boat hull may contribute to decrease between 10% and 20% the total resistance of the ship, reducing the energy consumption and saving fuel. The latter leads to a reduction in emissions which entails economic and environmental benefits. Among other new applications, bubbles are also employed with biomedical purposes as contrast agents in ultrasound diagnosis or in therapeutic treatments [41, 58]. They can also be used in drug delivery systems, releasing them upon ultrasound-mediated microbubble destruction, and thus permitting to locally deliver the drug, as well as simultaneously enhance the vascular permeability to increase drug deposition in tissue, which has a high potential in clinical applications [32]. However, the bubble behavior during its formation and rising motion, is a complex process, not fully understood, which reduces its applicability nowadays.

Consequently, the aim of this dissertation is to contribute to improve the knowledge of bubble dynamics behavior and to develop appropriate tools to allow the study and description of the bubble formation phenomenon and its subsequent ascending motion under different situations.

1.2 Background and previous works

In the study of bubble dynamics, it is necessary to focus on two fundamental aspects: the formation process and the ascending motion in liquids. Both processes have been widely studied with the goal of understanding the bubble behavior, the role played by the gas-liquid interface and the influence that the flow exerts on the bubble. However, despite being a well studied phenomenon, there are still important unknown physical aspects that hinder their complete knowledge. In the following, a brief summary of the major features taking place during the bubble formation and the

subsequent rising motion is provided.

1.2.1 Bubble formation

Optimal bubble generation is of great relevance in a countless number of industrial applications, such as, bubble columns, fermentation vessels, airlifts, aerated bioreactors, or extraction equipment, among others. The simple bubble formation through submerged orifices or nozzles under different injection conditions [25, 71], i.e. constant flow rate, intermediate and constant pressure (see Fig. 1.1 extracted from [25]), has been replaced by new bubble generation techniques, e.g. co-flows, cross-flows, flow-focusing, etc., due to the *micro* and *nano* requirements in current industrial processes[1]. Unlike the situations where the gas is supplied either at constant flow rate or constant pressure conditions, very little attention has been paid to the traditional bubble formation at intermediate conditions, even though it has been shown that the chamber volume plays an important role in the bubble dynamics [4, 62, 69, 106, 153]. Moreover, this process is currently being used to produce metal foams, which are cellular structures consisting of a solid metal, frequently aluminium, containing a large volume fraction of gas-filled pores produced by the intermediate injection conditions [39, 45, 80, 79].

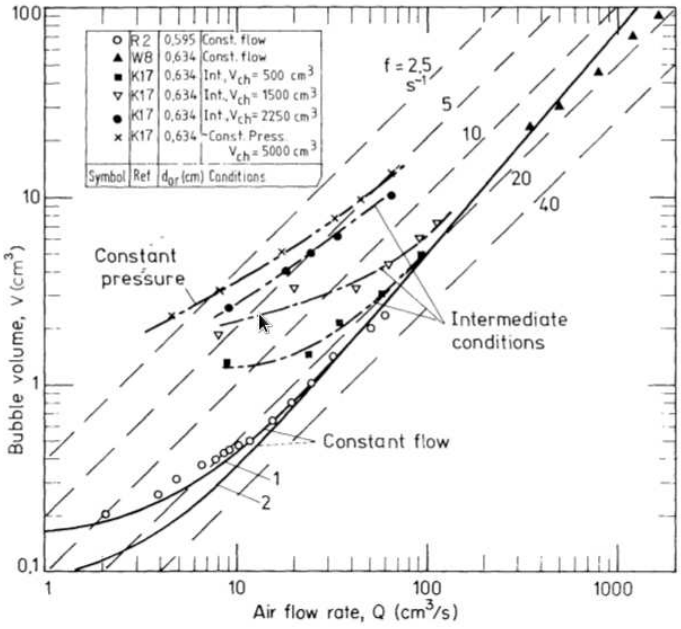

Figure 1.1: Bubble volume versus the gas flow rate for the case of air injection into water. Experimental results obtained at constant flow rate, intermediate, and constant pressure conditions. Reprint from [25].

As already mentioned above, a few studies have addressed the bubble formation under intermediate injection conditions. In this case, it is important to be able to control the process to periodically generate bubbles of a given size, avoiding the weeping phenomenon. In the late 60s,

[1] See the review by Rodríguez-Rodríguez *et al.* [119] for a description of these techniques.

Khurana & Kumar [69] modeled the bubble formation process following the two-stage expansion-detachment approach traditionally applied to the cases of constant flow rate and pressure conditions [115, 134]. However, they did not adequately determine the time evolution of the bubble volume, because the expansion stage was not dynamically treated, as pointed out by LaNauze & Harris [74]. Later on, Tsuge & Hibino [162] proposed an improved model, introducing the viscosity effects, which provided the bubble size and the pressure fluctuations during the bubble growth, considering spherical bubble shapes. Nevertheless, although other authors assumed non-spherical bubble shapes, they did not characterize the formation period, describing only the part of the process in which the gas is injected through submerged orifices [85, 86, 108, 147, 153]. A review of the aforementioned models describing the formation of bubbles from a submerged orifice under intermediate or constant pressure conditions has been provided by [176]. However, these studies do not consider the situation where the air is injected through a vertical needle or nozzle, differently from the case of constant flow rate conditions where they are commonly used [16].

1.2.2 Bubble rising

Bubble dynamics rising motion constitutes another of the main aspects that characterizes its behavior. It is known that the bubble shape, path and wake should not be considered independently but as interrelated parts of the same phenomenon. Leonardo Da Vinci was the first reporting this idea [113, 114], denoted as "Leonardo's paradox" by the scientific community. In general, the analysis of bubbles ascending in still liquids has been carried out by numerous researchers theoretically, experimentally or numerically since the 50s [25, 71, 83]. However, only a few studies have linked the shape, the wake and the path to accurately determine the bubble stability, i.e. the transition from stable to unstable motion, and the physical mechanisms that produce such transition.

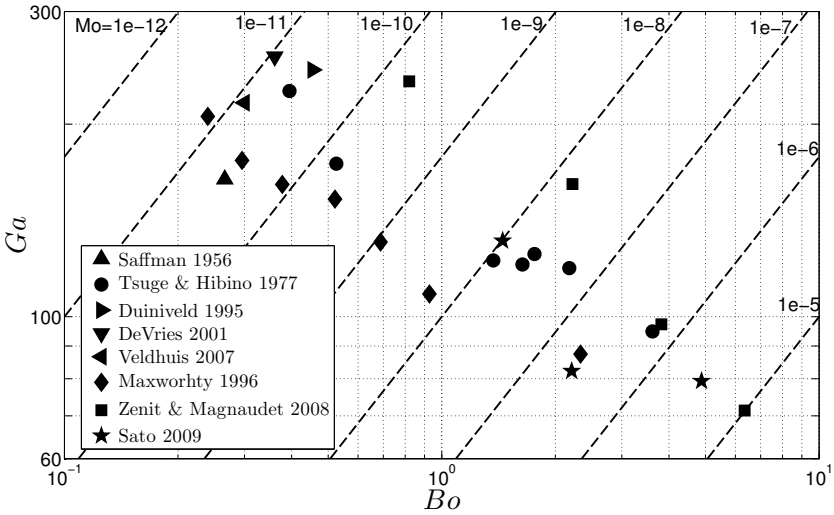

Figure 1.2: Phase diagram showing the Bond and Galilei numbers of bubbles in the neighbourhood of the transition from stable to unstable motion experimentally described by [29, 34, 88, 125, 133, 163, 170, 182].

On the one hand, from the experimental point of view, the existing studies have permitted to describe and understand the main flow features. Initially, Haberman & Morton [53] showed the evolution of the bubble shape and the terminal velocity as a function of the liquid properties and the bubble size. Later on, other studies described the bubble trajectory [34, 103, 125, 140, 163, 182] and the time evolution of the bubble shape [13, 76]. Moreover, experimental measurements have shown that the topology of the bubble wake and the bubble trajectory are coupled, being the unstable path associated to the development of a pair of counter-rotating vortices. The latter was also confirmed numerically by Mougin & Magnaudet [98] and Yang & Prosperetti [179]. However, the experimental measurements might present drawbacks. These tests are commonly performed by means of flow visualizations [81, 128, 133], particle image velocimetry [18, 183], laser doppler anemometry [36], thermographic Schlieren technique [29, 170] and planar laser-induced fluorescence [126, 142]. Some of these techniques require the use of seeding particles that accumulate on the bubble surface and modify the boundary condition at the gas-liquid interfase from slip (in the case of clean liquids) to non-slip (in the case of contaminated liquids). Other techniques introduce temperature gradients over the bubble surface, inducing surface tension gradients and, consequently, secondary currents caused by the Marangoni effect. The contamination of the bubble surface substantially changes the dynamics of the bubble wake and the development of the wake instabilities [145] making extremely difficult to perform clean and well controlled experiments.

Figure 1.2 shows a collection of experimental measurements determining the transition from stable to unstable rising motion of bubbles in the Bond-Galilei parametric space. The Bond number, $Bo = \rho_l \, g \, D^2/\sigma$, is a dimensionless measure of the bubble size and the Galilei number, $Ga = \rho_l \, g^{1/2} \, D^{3/2}/\mu_l$, a dimensionless number that characterizes the bubble terminal velocity. Here, σ is the surface tension, g the gravitational acceleration, D the bubble equivalent diameter, and ρ_l and μ_l the liquid density and viscosity respectively. The trigger of the path instability was first associated to shape oscillations, i.e. wobbling bubble, however Meiron [92] demonstrated that shape oscillations did not cause the path instability. In fact, Lunde & Perkins [82], and later on Veldhuis *et al.* [169], experimentally established that the shape oscillations were always observed after the wake and path instabilities were present. Maxworthy *et al.* [88] observed that the terminal velocity of a bubble injected in a liquid of a given Morton number, $Mo = g\mu_l^4/\rho_l\sigma^3$, increases with the diameter of the bubble, until it reaches a maximum value and begins to decrease for larger bubbles. Thus, they identified the maximum terminal velocity with the onset of the path instability, since it is known that the bubble rising velocity decreases when the wake becomes unstable [37]. Other authors defined the transition visually, by observing the bubble trajectory and identifying the conditions for which the bubble did no longer followed a vertical, straight path [29, 34, 125, 133, 163, 170, 182]. The lack of a unified criterion, together with the experimental limitations causing the bubble surface contamination, have made difficult to establish a clear transition curve, giving rise to the dispersion of data points displayed in Fig. 1.2.

On the other hand, to avoid the contamination of the experiments, the onset to unstable motion has been studied by means of numerical simulations. The results showed that the instability onset corresponded to the loss of the flow axisymmetry and the development of a pair of counter-rotating vortices in the bubble wake, inducing a non-vertical trajectory, as reported by Mougin & Magnaudet [98]. Furthermore, Magnaudet & Mougin [84] determined the neutral curve in terms of

the bubble aspect ratio, defined as the mayor-to-minor bubble diameter ratio, χ, and the Reynolds number $Re = \rho_l D U_T / \mu_l$, where U_T is the terminal velocity (see the solid line in the Fig. 1.3). In most numerical studies the bubble shape has been prescribed to simplify the computations, assuming either spherical or spheroidal bubbles instead of using their real shape. However, such assumption may affect the vorticity generation along the bubble surface and, consequently, the stability characteristics of the flow established.

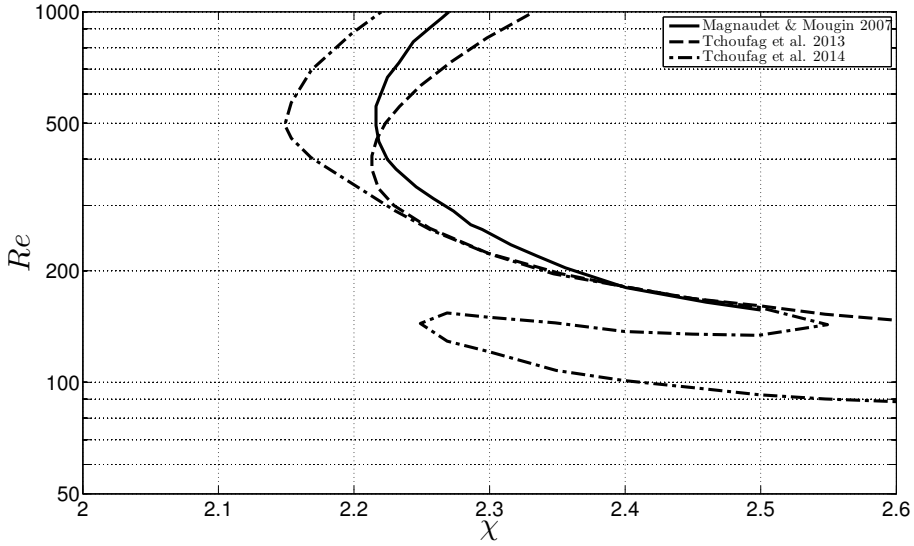

Figure 1.3: Stability diagram with the neutral curves obtained from Direct Numerical Simulations performed by Magnaudet & Mougin [84] assuming spheroidal bubble shapes (solid line), Linear Stability Analysis considering a fixed spheroidal bubble by Tchoufag *et al.* [150] (dashed line), and Linear Stability Analysis considering a freely moving spheroidal bubble by Tchoufag *et al.* [151] (dash-dotted line).

An alternative approach also used to determine the transition curve is the Linear Stability Analysis (LSA). This technique has been applied to spheroidal bodies implementing the kinematic and dynamic boundary conditions at the bubble surface to describe the stability characteristics of the base flow [179]. Recently, LSA has been used to determine the neutral curve by Tchoufag *et al.* [150], considering bubbles whose velocity and orientation were kept fixed and, consequently, which interacted with the fluid only as fixed bodies. Later on, they extended their study considering bubbles free to move and rotate, which required the coupled fluid+bubble system of linearized governing equations to be solved [151]. The results from the LSA by Tchoufag *et al.* [150, 151] are also shown Fig. 1.3 with dashed and dash-dotted lines respectively. However, as in previous Direct Numerical Simulations, the bubble shape was assumed to be spheroidal in the Linear Stability Analysis, and the influence of the bubble shape, i.e. the fore-aft asymmetry adopted in the bubble shape as it rises, was not taken into account in those studies.

1.3 Outline of the dissertation

The present dissertation is organized as follows. Chapter 2 is devoted to study the bubble formation from a submerged vertical needle under intermediate conditions, and a model to describe the time evolution of the chamber pressure is proposed. Chapter 3 includes an overview of the main techniques used to track the interface, with especial attention to those that minimize the presence of parasitic currents. The motion of a stable bubble rising with a rectilinear path is also described in this chapter by means of two-dimensional axisymmetric simulations, also considering the effects of the gas properties. Chapter 4 describes in detail the different shapes adopted by the bubbles as a function of their characteristic dimensionless parameters. Additionally, this chapter also presents a description of the bubble wake, identifying the flow conditions which lead to the formation of a standing eddy behind the bubble and determining the transition curve when the real bubble shape is taken into account. Chapter 5 includes a Linear Stability Analysis applied to real shape bubbles rising in still liquids. The stability analysis is carried out considering two different scenarios: first, bubbles whose velocity and orientation are kept fixed, and second, bubbles free to move and rotate, which requires the coupled fluid+bubble system of linearized governing equations to be solved. Furthermore, the effect of the fore-and-aft asymmetry of the bubbles on the wake instability is also assessed. Chapter 6 describes the different flow patterns observed from Direct Numerical Simulations of bubbles of different Morton numbers in a wide range of Bond and Galilei numbers. The transition curve is also determined numerically and compared with the transition curves obtained in Chapters 4 and 5. Finally, Chapter 7 summarizes the main conclusions of the dissertation and proposes future works.

CHAPTER
TWO

Analysis of the bubble formation from a submerged vertical needle connected to a pressurized chamber

In this chapter, an analytical and experimental study of the formation of bubbles from a submerged vertical needle under mixed conditions, where neither the gas flow rate nor the feeding pressure remain constant during the process, is performed. In particular, focusing on the time evolution of the pressure inside the gas injection chamber during the formation process, modeling the pressure signal and analyzing the bubble size and shape as functions of the volume of the chamber, V_c, the needle radius, a, and the mean gas flow rate, Q_i. Unlike in the case of bubble formation from orifices, the study highlights the importance of the evolution of the column of water penetrating inside the injection needle on the bubble formation process. Consequently, the model proposed includes the description of the time evolution of the liquid column penetrating inside the needle after the separation of a bubble, and the subsequent pressurization of the gas chamber.

This chapter is included in the paper "Influence of gas chamber conditions on the formation of bubbles from a submerged vertical needle", by J.C. Cano-Lozano, C. Gutiérrez-Montes and C. Martínez-Bazán, submitted to the Int. J. Heat Mass Transfer.

2.1 Introduction

Nowadays, the diversity of industrial, medical and pharmaceutical necessities have incentivized the development of new techniques to generate bubbles, and more recently, micro- or nano-bubbles, i.e co-flows, cross-flows, flow-focusing, among other methods [119]. However, the traditional way of forming bubbles from a submerged orifice, nozzle or needle in a stagnant liquid is still widely used. In this case, the bubble generation can be driven at constant flow rate, at constant injection pressure or at mixed conditions. The two first cases, constant gas flow rate and constant injection pressure conditions, have been extensively analyzed (see for example [25, 71]), but the formation of bubbles under conditions where neither the gas flow rate nor the injection pressure are prescribed has been less studied. In fact, under these conditions the bubble formation process becomes more complex because the pressure inside the gas chamber, and consequently the flow rate feeding the bubble, vary with time [69, 89], impeding the controlled periodic generation of bubbles of a given size [96, 35]. Nevertheless, despite these difficulties, injection conditions where both the gas flow rate and the chamber pressure vary during the bubble formation process are very common in many industrial applications, such as the fabrication of aluminum foams [39, 79].

The gas chamber plays a significant role when the gas flow rate and the injection pressure do

not remain constant, a phenomenon first reported by Hughes *et al.* [62] and Davidson & Schuler [28]. In fact, Park *et al.* [106] classified the formation regimes in terms of the gas chamber volume as *small chamber region*, *medium chamber region* and *large chamber region*, being $V_c > 800$ cm^3 the upper limit for which the volume of the chamber no longer affected the bubble size, and remaining its pressure constant during the bubble formation. Nevertheless, the gas chamber volume can be classified in terms of the dimensionless capacitance number [62], defined as

$$N_c = \frac{g(\rho_l - \rho_g)V_c}{\pi\, a^2 \rho_g\, c^2} = \frac{g(\rho_l - \rho_g)V_c}{\pi\, a^2\, \gamma\, P_m}, \tag{2.1}$$

where c is the speed of sound in the gas, g is the gravitational acceleration, ρ_l and ρ_g the liquid and gas densities respectively, γ the ratio of specific heats (isentropic coefficient), a the radius of the orifice and P_m the mean absolute pressure inside the chamber. In fact, in their study, Hughes *et al.* [62] concluded that the effect of the chamber volume was negligible for $N_c < 0.85$.

Furthermore, the bubble formation from an orifice that connects a liquid pool with a gas chamber has been divided into two different stages, i.e. a holding stage and a formation stage [69, 162], with the holding stage finishing when the pressure in the gas chamber rises to match the sum of the hydrostatic and the surface tension pressures. Thus, during the holding stage, the gas feeding the chamber makes the pressure increase until the bubble starts to growth. At this point, during the formation stage, the bubble inflates and the chamber pressure decreases rapidly.

The pressure fluctuations inside the gas chamber during the entire bubble generation process have been registered using microphones [178, 177] or pressure transducers [106, 122]. However, the experimental measurements do not always agree with the time evolution of the chamber pressure provided by the analytical models. In addition, under certain conditions, during the formation stage, the chamber pressure can decrease below the pressure inside the bubble, inducing a flow rate from the bubble to the chamber which makes the bubble deflate [162, 153].

The aim of this chapter is to describe the bubble generation from a submerged vertical needle in a stagnant liquid under mixed conditions, determining the bubble production frequency and the bubble size, as a function of the gas chamber volume, V_c, and the needle radius, a. Thus, the experimental facility is described in section 2.2; a mathematical model developed to determine the time evolution of the gas pressure is given in section 2.3, and the experimental results are discussed in section 2.4. Finally, conclusions are provided in section 2.5.

2.2 Experimental set-up

The experimental facility used in the present work is sketched in Fig. 2.1. It is similar to those used to study the formation of bubbles from an orifice in previous works [4, 69, 106, 153, 162], but using in this case a submerged vertical needle to inject the gas into the liquid pool [132]. It basically consists of a 30×30 cm^2 base Plexiglas cubic pool filled with distilled water (liquid), where the gas (air in this case) was supplied through a short needle connected to the gas feeding chamber also made of Plexiglass, what allowed us to observe if water penetrated inside the chamber during

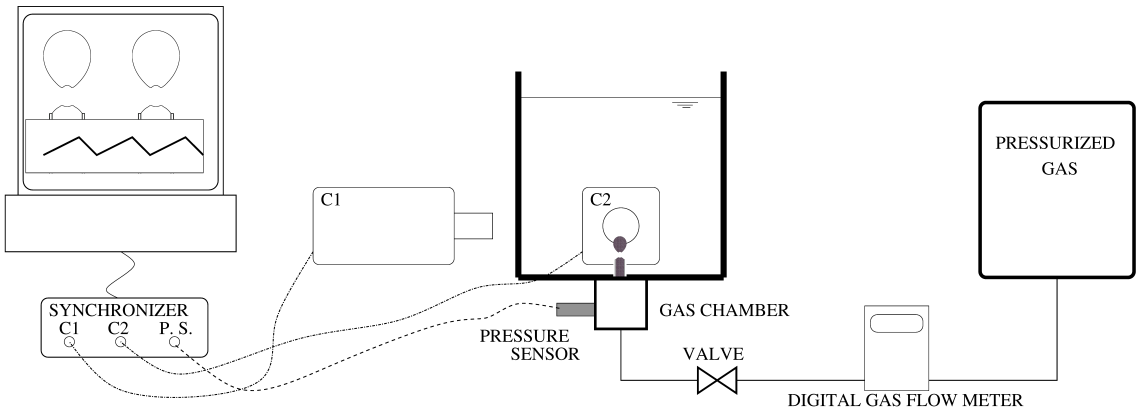

Figure 2.1: Sketch of the experimental facility.

the process (weeping). The size of the liquid pool was much larger than the bubble size, ensuring that wall effects were always negligible on the experimental measurements presented. The gas chamber was pressurized by injecting a constant flow rate of gas, Q_i, through a long capillary tube avoiding, therefore, that the air-supply line behaved as a secondary chamber. The air was supplied from a compressed air bottle to the feeding chamber through a gas line equipped with a filter, a regulator valve and a mass flow meter Aalborg ($0 - 100$ ml/min). The range of gas flow rates covered in the experiments reported here varied from 10 to 50 ml/min, to avoid the formation of groups of bubbles and possible coalescence phenomena [90], as well as the weeping phenomenon. Four cylindrical gas chambers of diameter 2 cm and volumes 10, 20, 30 and 40 cm^3 respectively were employed. As for the injection needles, two stainless steel needles of inner radii $a = 0.42$ and 0.81 mm, and total volumen of 1.25 cm^3, including the needle holder, were used. It should be mentioned that the experimental observations indicated that the solid-liquid-gas contact line was always pinned at the inner edge of the needle when the bubble was growing. Finally, the liquid level was kept constant at $H = 17$ cm above the needle (see Fig. 2.2a).

Images were recorded at frame rates that varied from 10000 to 15000 fps, depending on the conditions, with two high speed cameras FASTCAM Photron placed at 90^o from each other, as shown in Fig. 2.1. A pressure transducer UNIK 5000 GE, synchronized with the two high speed cameras, was used to register the time evolution of the pressure inside the chamber during the bubble generation process. Thus, the pressure evolution has been mesured and correlated with the bubble growth. In addition, the use of two cameras focusing at two perpendicular planes allowed to ensure that the conditions under which the bubble formation ocurred are axisymmetric.

With the above description, the different parameters characterizing the experiments performed were: the inner radius of the needle, a, the surface tension, σ, the liquid density, ρ_l, the gas density considered at ambient conditions, ρ_g, the liquid viscosity, μ, the gravitational acceleration, g, the constant gas flow supplied to the gas chamber, Q_i, and the chamber volume, V_c. Thus, provided that the bubble formation is inviscid in this case, the dimensionless parameters are given by the Bond number, $Bo = (\rho_l - \rho_g)\, g\, a^2/\sigma$, the Weber number, $We = \rho_l Q_i^2/(\pi^2 a^3 \sigma)$, and the capacitance number, N_c. Hereafter, in this chapter, the characteristic scales for the bubble volume, time and pressure, will be the Fritz volume, $V_F = 2\pi\sigma a/(\rho_l g)$, the capillary time, $t_c = (\rho_l a^3/\sigma)^{1/2}$, and the

capillary pressure, $p_c = \sigma/a$, and the dimensionless bubble volume, time and chamber pressure will be denoted with asterisk as, $V_b^* = V_b/V_F$, $t^* = t/t_c$ and $p^* = p/p_c$ respectively.

2.3 Theoretical model

The chamber-orifice interaction during the formation process of bubbles was described by Park *et al.* [106] for different chamber volumes. In the case of small chambers, they observed that the pressure decreased rapidly as the bubble grew and that, for sufficiently small reservoirs, the chamber pressure matched that of the bubble before detachment. After the bubble release, the gas pressure increased linearly with time due to the constant gas flow rate injected into the chamber. However, if the bubble is formed from a needle instead of an orifice, some differences are observed. In fact, Fig. 2.2(b) shows the time evolution of the chamber pressure (grey line) when a reservoir of volume V_c= 11.75 cm^3 is used to form bubbles from a transparent needle of radius a= 0.5 mm by injecting a gas flow rate of Q_i= 23.5 ml/min. It can be observed that, after the detachment of a bubble at point A, the pressure increases until the bubble starts to grow at point B. However, unlike the case of bubble formation from an orifice, in this case the chamber pressure does not increase linearly with time. In addition, once the bubble starts to grow, the chamber depressurizes very fast because, during this stage, the bubble growth rate, dV_b/dt, is greater than the gas flow rate injected into the chamber, Q_i. Thus, the period of time between points A and B will be denoted *holding stage* and that between B and A *formation stage*.

In the following, the time evolution of the pressure inside the chamber will be moldeled. First, it will be assumed that the density inside the chamber, $\rho_c(t)$, is always equal to that of the bubble, $\rho_b(t)$, considering $\rho_c(t) = \rho_b(t) = \rho(t)$. On the one hand, applying the mass conservation equation in the chamber, one gets

$$\frac{\partial\left[\rho(t)\,V_c\right]}{\partial t} = G_i - G(t), \tag{2.2}$$

where $G_i = \rho_g\,Q_i$ is the constant mass flow rate injected into the chamber and $G(t)$ the time varying mass flow rate flowing from the chamber to the bubble. On the other hand, the mass conservation equation in the bubble, is given by

$$\frac{\partial\left[\rho(t)\,V_b(t)\right]}{\partial t} = G(t), \tag{2.3}$$

where $V_b(t)$ is the bubble volume which changes with time. Combining Eqs. (2.2) and (2.3) provides

$$\frac{\partial\left[\rho(t)V_b(t) + \rho(t)V_c\right]}{\partial t} = G_i. \tag{2.4}$$

Integrating Eq. (2.4), the time evolution of the gas density, $\rho(t)$, can be obtained as

$$\rho(t) = \rho_0\left(\frac{V_c}{V_c + V_b(t)}\right) + \frac{G_i\,t}{V_c + V_b(t)}, \tag{2.5}$$

where ρ_0 represents the gas density inside the chamber after the release of a bubble. Equation (2.5) indicates that, during the *holding stage*, since V_b=0, the density inside the chamber increases

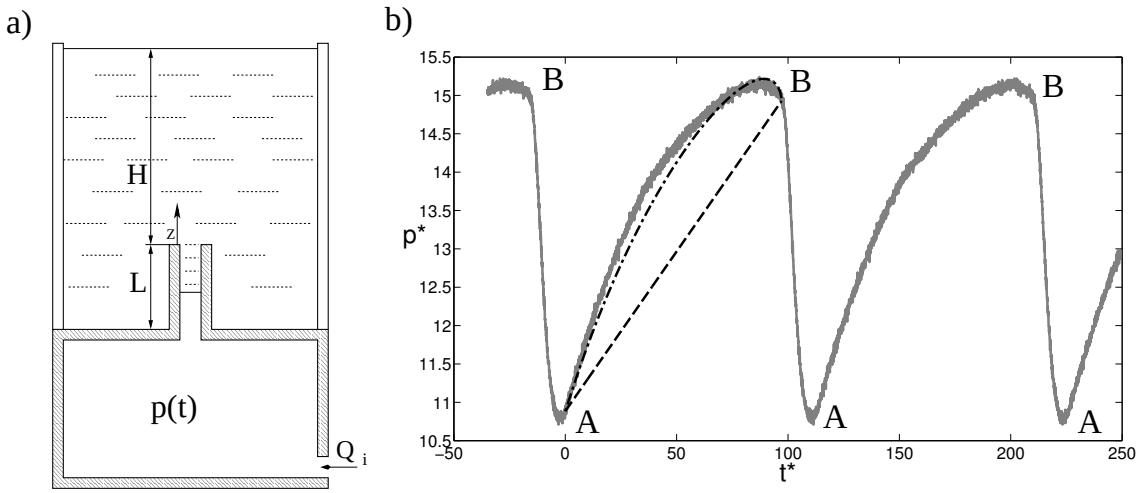

Figure 2.2: a) Model scheme. b) Experimental (grey line) and analytical (dashed and dash-dotted lines) pressure signals for a bubble with $Bo = 0.034$, $We = 1.73$ and $N_c = 1.05$.

linearly with time as $\rho(t) = \rho_0 + G_i\, t/V_c$. In addition, the energy equation allows to determine the evolution of the chamber pressure as,

$$p(t) = \rho^{\gamma}(t) \left(\frac{p_0}{\rho_0^{\gamma}} \right), \tag{2.6}$$

where p_0 is the chamber pressure after the release of a bubble at $t = 0$, and γ the isentropic coefficient. In this study, $\gamma = 1.4$ was employed, although the process can be assumed polytropic with γ going from $\gamma = 1$ (isothermal) to $\gamma = 1.4$ (isentropic).

Although the above described model reproduces the *formation stage* accurately with $V_b(t)$ obtained from the experimental measurements, it provides a linear increase of the chamber pressure during the *holding stage* as shown by the dashed line in Fig. 2.2(b). However, the experimental measurements show that the pressure in the gas chamber (grey line in Fig. 2.2b) is higher than that given by Eqs. (2.5)-(2.6) (dashed line), indicating that there is a mechanism, additional to the gas injection, that contributes to rise the pressure over the linear increase taking place in the case of bubble formation from an orifice and predicted by the model. What happens in the formation of bubbles from a vertical needle is that, under certain conditions, after the formation of a bubble, the liquid penetrates inside the injection needle forming a meniscus that goes down towards the gas chamber as shown in Fig. 2.2(a), contributing to pressurize it. Accordingly, this effect has been included in the model developed to describe the time evolution of the pressure inside the gas chamber. Thus, it has been considered that, when a bubble pinches-off, the liquid-gas interface which is initially at the needle tip, $z = 0$, starts to move down towards the chamber, until reaching an equilibrium position at which the liquid hydrostatic pressure matches the pressure inside the chamber. At this point, since the chamber pressure keeps increasing due to the gas supplied, G_i, the meniscus begins to rise towards the needle tip.

The evolution of the meniscus inside the needle can be modeled considering the pressure drop

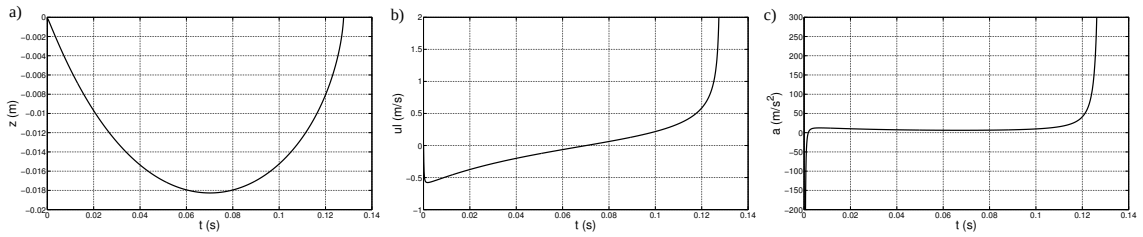

Figure 2.3: Meniscus motion inside the needle during the holding stage of a bubble formation process corresponding to $Bo = 0.034$, $We = 1.73$ and $N_c = 1.05$. a) Meniscus position. b) Velocity. c) Acceleration.

of the water column as,

$$\frac{\partial u_l}{\partial t} + \frac{\partial}{\partial z}\left(\frac{p_l}{\rho_l} + gz\right) = -\frac{\lambda u_l^2}{4a} = -\frac{32\nu u_l}{4a^2}, \tag{2.7}$$

where $\lambda = 64/Re$, p_l is the liquid pressure and $u_l = dz/dt$ the meniscus velocity inside the needle. Integrating Eq. (2.7) with respect to z one gets,

$$\frac{\partial u_l(t)}{\partial t} - \left[\frac{p_a - p(t) - \rho_l u_l^2/2 + \rho_l g(H - z(t))}{\rho_l\, z(t)}\right] + \frac{8\nu}{a^2}\, u_l(t) = 0, \quad \text{if} \quad u_l < 0, \tag{2.8}$$

with p_a the atmospheric pressure, if the water column is penetrating inside the needle and,

$$\frac{\partial u_l(t)}{\partial t} - \left[\frac{p_a - p(t) + \rho_l g(H - z(t))}{\rho_l\, z(t)}\right] + \frac{8\nu}{a^2}\, u_l(t) = 0, \quad \text{if} \quad u_l > 0, \tag{2.9}$$

if the meniscus rises up, ejecting the water that has previously penetrated inside the needle. Notice that, in Eqs. (2.8) and (2.9) the values of z are negative, $z < 0$, and that the liquid pressure at the entrance of the needle in Eq. (2.8) has been considered $p_l(z = 0) = p_a + \rho_l g H - \rho_l u_l^2/2$, while the pressure at the end of the meniscus has been assumed to be the chamber pressure, $p_l(z) = p(t)$, neglecting surface tension effects. Similarly, in Eq. (2.9), where the liquid column is ascending, the pressure at the air-water interface is also the chamber pressure, $p_l(z) = p(t)$, but the pressure at the needle tip is $p_l(z = 0) = p_a + \rho_l g H$, since the water inside the needle discharges into the liquid pool.

The evolution of the liquid column penetrating inside the needle was analyzed using a transparent needle. It was observed that, after the formation of a bubble, the liquid meniscus penetrated rapidly inside the needle achieving a maximum penetration depth at the position where the liquid pressure became equal to the pressure in the gas chamber, $p_a + \rho_l g[H - z(t)] = p(t)$ (Fig. 2.3a). After this point, the chamber pressure becomes larger than the hydrostatic pressure and the liquid column begins to drain at a velocity that increases with time, as shown in Fig. 2.3(b). Figure 2.3(c) shows that the motion of the water column inside the needle is driven by a nearly constant acceleration during almost 90% of the time. Only during the initial (final) instants the meniscus decelerates (accelerates) very rapidly. It should be noted that, as the water column moves inside the needle, the contact angle at the air-water-wall contact line might vary, an effect that will be commented later in section 2.4.

Finally, considering that the effective volume of the gas chamber varies with the motion of the liquid column, decreasing it an amount equal to $\pi a^2\, z(t)$, Eq. (2.5) can be modified as,

$$\rho(t) = \rho_0 \left(\frac{V_c}{V_c + \pi a^2\, z(t) + V_b(t)}\right) + \frac{G_i\, t}{V_c + \pi a^2\, z(t) + V_b(t)}, \tag{2.10}$$

where $z(t)$ is given by Eqs.(2.8)-(2.9). Eqs. (2.6), (2.8), (2.9) and (2.10) determine the time evolution of the density and pressure in the gas chamber and the position of the water column inside the needle. In addition, the mass flow rate injected into the forming bubble can be obtained from Eq. (2.3) and, consequently, the temporal evolution of the pressure inside the bubble can be calculated as

$$p_b(t) = p(t) - \frac{1}{2}\frac{|G(t)|G(t)}{\rho(t)(\pi a^2)^2}, \tag{2.11}$$

indicating that if $G(t) > 0$ the gas flows from the chamber to the bubble with $p(t) > p_b(t)$. However, if the pressure inside the bubble becomes larger than that of the chamber, $p_b(t) > p(t)$, the gas will flow from the bubble to the chamber with $G(t) < 0$ as will be shown later in some of the experimental cases reported.

The time evolution of the pressure inside the gas chamber for a case corresponding to $Bo = 0.034$, $We = 1.73$ and $N_c = 1.05$ (a= 0.5 mm, V_c= 11.75 cm^3 and Q_i = 23.5 ml/min) obtained from the model including the evolution of the water column inside the needle is shown in Fig. 2.2(b) by a dash-dotted line. It can be observed that the model reproduces accurately the gas chamber pressure when the pressurization effect of the water column penetrating inside the injection needle is taken into account. Nevertheless, it is important to mention that if the liquid penetration depth was larger than the length of the needle, $L < max(|z(t)|)$, the water would leak inside the gas chamber, leading to the weeping phenomenon.

2.4 Results

In this section, the experimental results obtained using four different gas chambers and two injection needles will be discussed. First, the experimental pressure signals will be compared with the pressure evolution provided by the model described in section 2.3. In addition, the time evolution of the bubble volume and injection pressure will be discussed in terms of the chamber volume, the radius of the needle and the gas flow-rate in dimensionless forms, i.e. N_c, Bo and We respectively. Finally, the evolution of the bubble shape and its dependence on the instantaneous gas flow feeding the bubble, We_{inst}, will be considered.

2.4.1 Pressure fluctuation inside the gas chamber

The time evolution of the gas pressure inside the injection chamber during a bubbling event has been shown in Fig. 2.4, for a constant gas flow rate Q_i = 25 ml/min and four different chambers of volumes V_c= 11.25, 21.25, 31.25 and 41.25 cm^3 respectively. The figure includes experimental results obtained using two needles of radii $a = 0.42$ and 0.81 mm which correspond to Bo= 0.024 and 0.089 respectively. The experimental measurements are compared with the pressure evolutions obtained using the simplified analytical model given by Eqs. (2.5) and (2.6) (dashed line), and that provided by Eqs. (2.10) and (2.6) (dash-dotted line). Both models reproduce accurately the depressurization of the gas chamber during the formation stage, i.e the period of time at which the bubble inflates, although, as already commented above, the simplified model is not able to describe the pressure increase during the holding stage. It should be noted that the model that

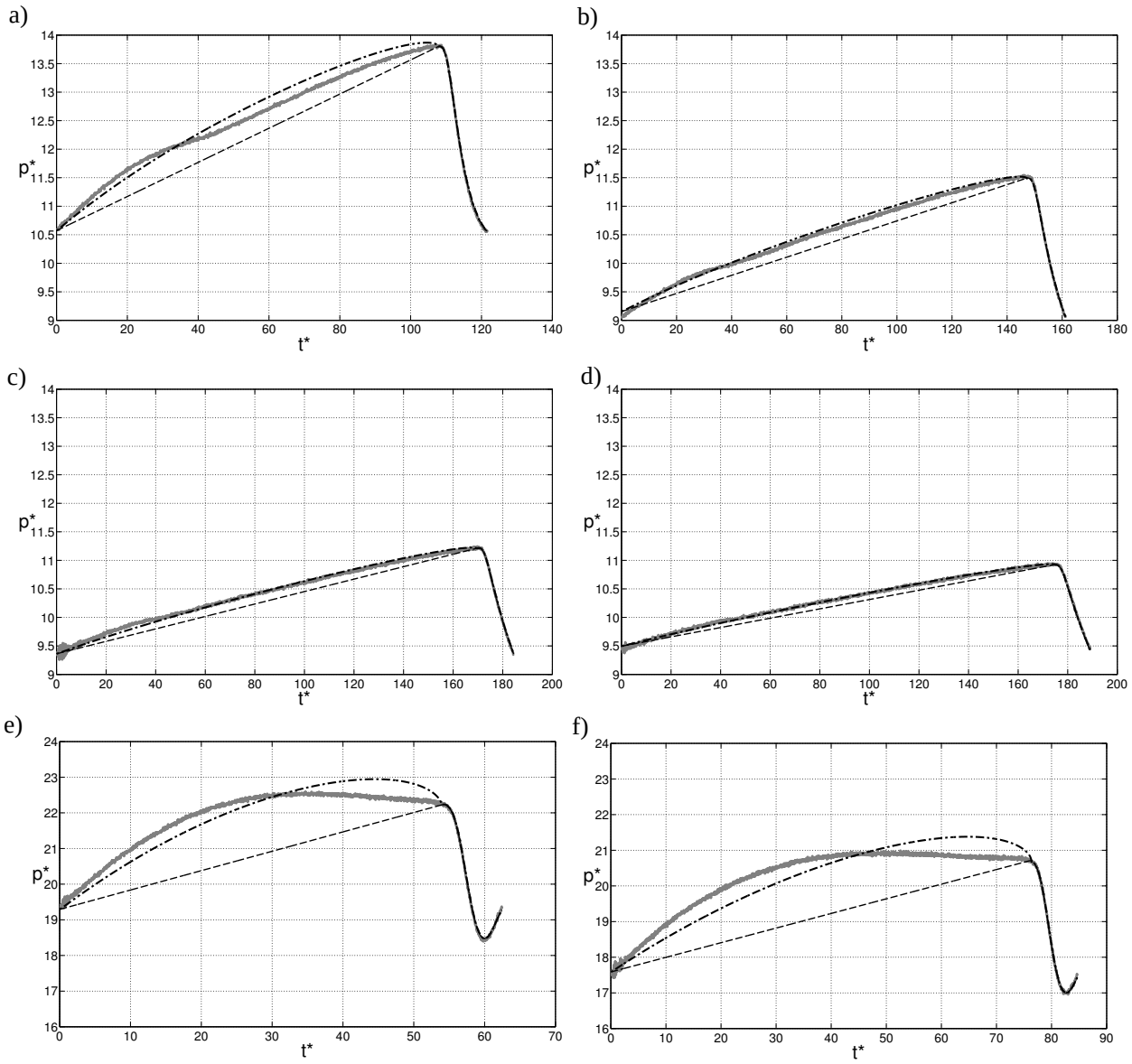

Figure 2.4: Time evolution of the pressure inside the gas chamber during a bubbling event when a flow rate of $Q_i = 25$ ml/min is injected into a chamber of volume: a) 11.25 cm^3 ($N_c = 1.41$), b) 21.25 cm^3 ($N_c = 2.66$), c) 31.25 cm^3 ($N_c = 3.92$), and d) 41.25 cm^3 ($N_c = 5.16$) connected to a needle of $Bo = 0.024$. Same for a gas chamber of volume: e) 31.25 cm^3 ($N_c = 1.07$), and f) 41.25 cm^3 ($N_c = 1.42$) with a needle of $Bo = 0.089$. The grey lines represent the experimental measurements, the dashed lines the pressure evolution given by the simple model and the dash-dotted lines the pressure provided by the model including the evolution of the water column inside the needle.

includes the evolution of the water column penetrating inside the needle agrees well with the experimental measurements, especially for the cases corresponding to V_c= 21.25, 31.25 and 41.25 cm^3 with a needle of radius $a = 0.42$ mm (figs. 2.4 b, c and d). However, it slightly differs from the experimental data corresponding to the smallest chamber (fig. 2.4 a), probably due to fact that the model considers a straight needle of constant radius, a, and the diameter of the needle used in the experiments changes when it connects to the holder. This effect is more significant for the lowest volume chamber where the needle-to-chamber volume ratio is larger. Another mechanism that might explain the differences observed in Fig. 2.4(a) is the evolution of the contact angle at the air-liquid-solid contact line during the motion of the water column inside the needle. Equations (2.8) and (2.9) consider that the air-water interface is flat, however, if the interface adopted an inverted spherical shape of radius $r_s = a\,/\cos\theta_e$, the chamber pressure given by the model would be slightly lower by an amount of $(2\sigma/a)\cos\theta_e$. Thus, since the differences observed in Fig. 2.4(a) are of the order of $\sigma/2a$, a meniscus with a contact angle of $\theta_e \approx 85^{\rm o}$ with respect to the gravity direction, instead of 90$^{\rm o}$ corresponding to the flat interface, seems to be formed during the holding stage. Consequently, a modification of Eqs. (2.8) and (2.9) to take into account surface tension effects would be given by

$$\frac{\partial u_l(t)}{\partial t} - \left[\frac{p_a - p(t) - (2\sigma/a)\cos\theta_e(t) - \rho_l u_l^2/2 + \rho_l g(H - z(t))}{\rho_l\, z(t)}\right] + \frac{8\nu u_l(t)}{a^2} = 0, \;\; \text{if} \;\; u_l < 0, \quad (2.12)$$

and,

$$\frac{\partial u_l(t)}{\partial t} - \left[\frac{p_a - p(t) - (2\sigma/a)\cos\theta_e(t) + \rho_l g(H - z(t))}{\rho_l\, z(t)}\right] + \frac{8\nu u_l(t)}{a^2} = 0, \;\; \text{if} \;\; u_l > 0. \quad (2.13)$$

The time evolution of the pressure chamber using a needle of radius $a = 0.81$ mm ($Bo = 0.089$) is shown in Fig. 2.4(e) for a chamber of volume 31.25 cm^3 and in Fig. 2.4(f) for a chamber of volume 41.25 cm^3. In this case, the chamber pressurizes faster than in the cases corresponding to the needle with $Bo = 0.024$ because the liquid column decreases more rapidly inside the needle. Similarly, once the water column achieves its maximum depth, it starts to move up until it reaches a velocity at which the gas flow rate ascending through the needle matches that injected inside the chamber, $Q_i \approx \pi a^2 dz/dt$. At this point, the chamber pressure stops increasing and remains nearly constant during the rest of the holding stage until the bubble starts to form. In this case, the model does not fully reproduce the experimental measurements because the flow resistance in the model is larger than the real one, providing lower liquid velocities inside the needle. In addition, the contact angle might vary as the liquid column goes down and up inside the injection needle. Thus, the time evolution of the contact angle has been plotted in Fig. 2.5 for the six cases shown in Fig. 2.4. To do so, the contact angle has been determined as $\cos\theta_e = (p_l^* - p^*)/2$, considering p^* the chamber pressure experimentally measured and p_l^* the liquid pressure given by the model (dash-dotted line). It can be observed that in Figs. 2.5(b), (c) and (d) the contact angle remains nearly equal to 90$^{\rm o}$ during most of the holding time, although during the initial stages the water column decreases with a contact angle slightly larger than 90$^{\rm o}$. However, in the case shown in figure 2.5(a) ($Bo = 0.024$, $N_c = 1.41$), the water column decreases with a spherical meniscus whose contact angle initially increases up to 94$^{\rm o}$ at $t^* = 20$. Subsequently, for $t^* > 37$, the liquid column moves inside the needle with an inverted cap of contact angle in the range $84^{\rm o} \leq \theta_e \leq 90^{\rm o}$. This effect is more evident in the cases corresponding to $Bo = 0.089$ shown in Figs. 2.5(e) and (f),

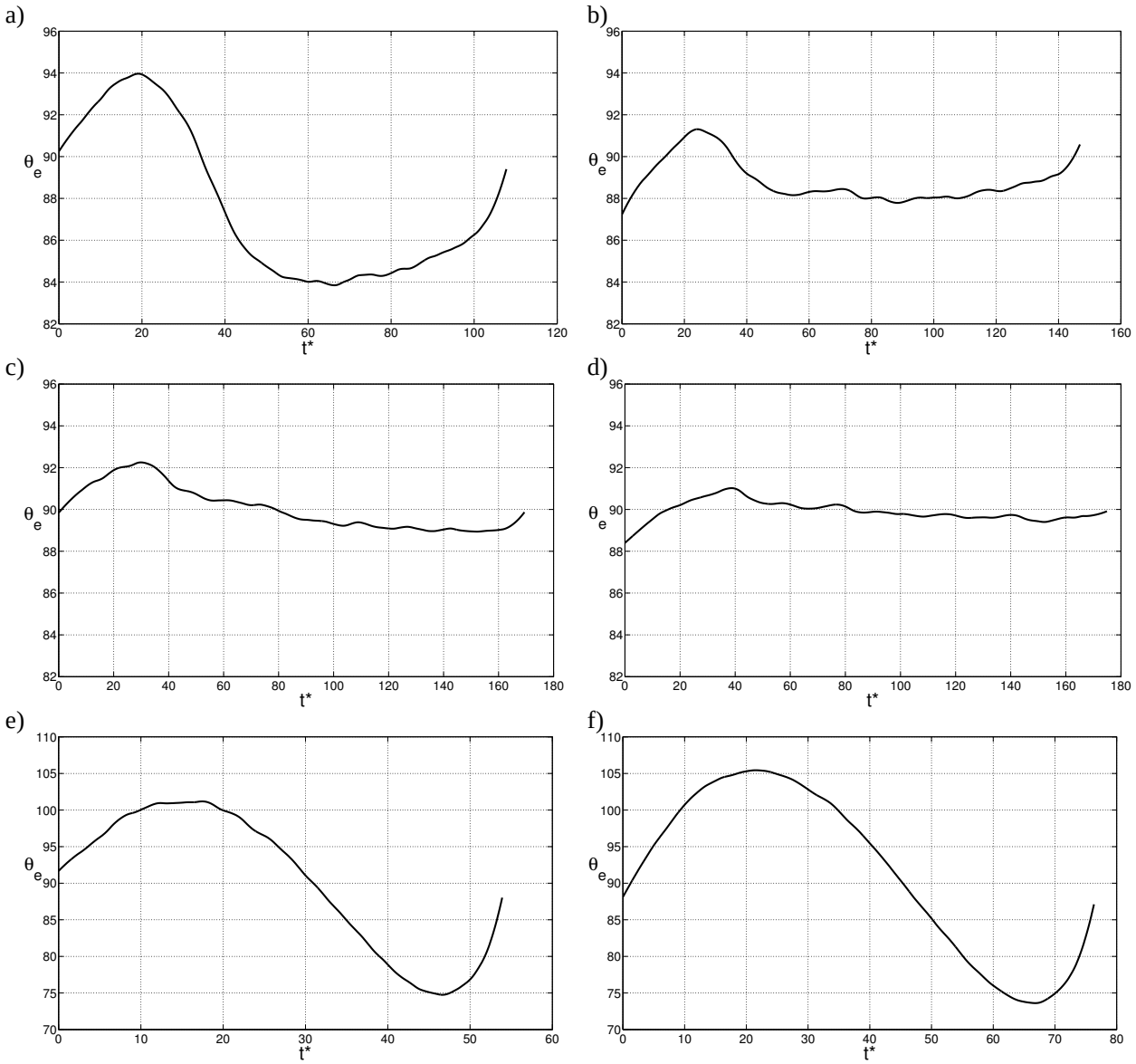

Figure 2.5: Time evolution of the contact angle extracted from Fig. 2.4. Flow conditions as in Fig. 2.4.

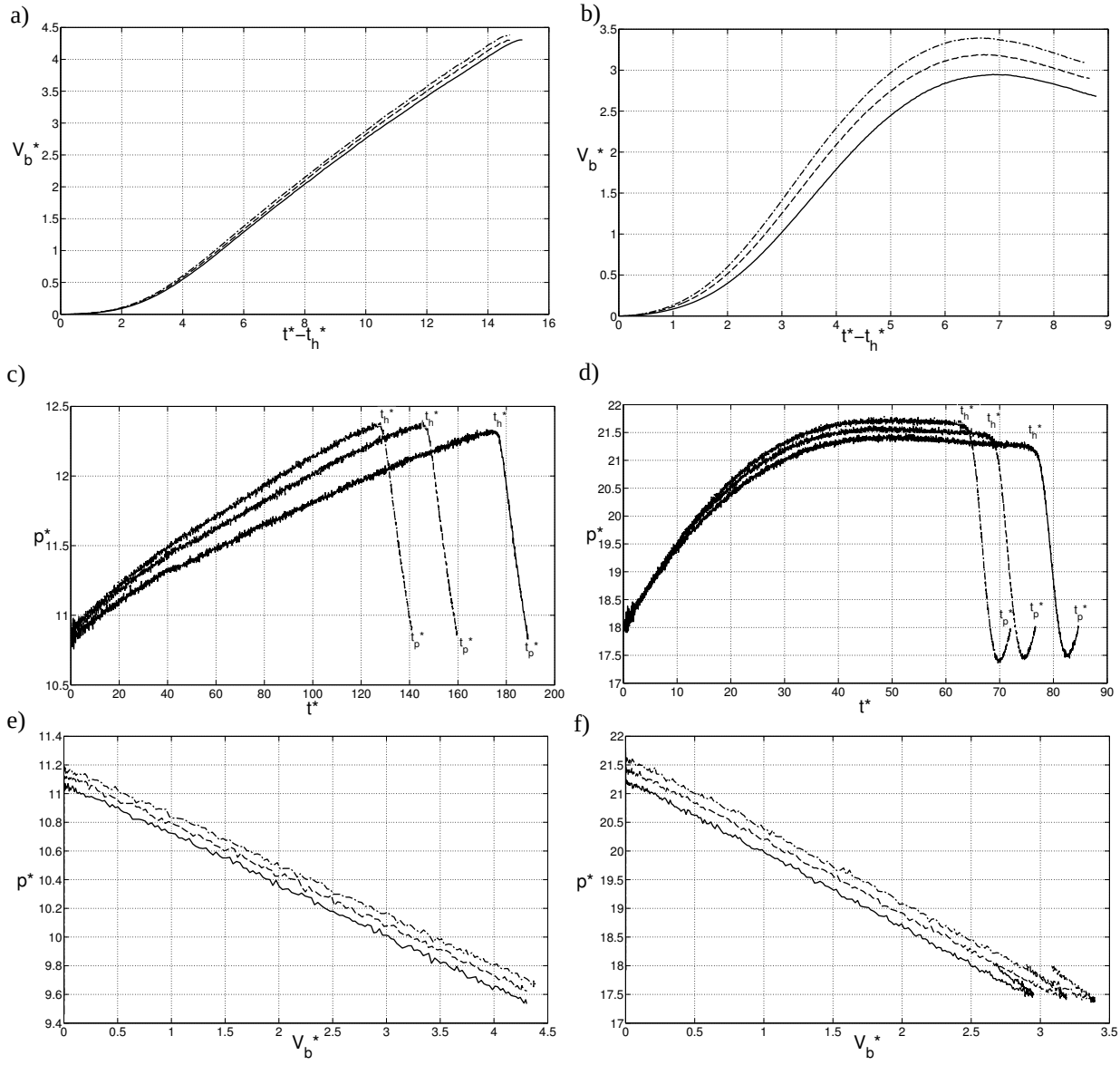

Figure 2.6: Dimensionaless time evolution of the bubble volume (upper row), V_b^*, time evolution of the chamber pressure (middle row), p^*, and evolution of the chamber pressure with the bubble volume (lower row) for three different gas flow rates, Q_i= 25 ml/min (solid line), 30 ml/min (dashed line) and 35 ml/min (dash-dotted line) respectively. The left column corresponds to the experimental results obtained with a needle of $Bo = 0.024$ ($N_c = 5.16$) and the right one with a needle of $Bo = 0.089$ ($N_c = 1.42$). Here the chamber volume is $V_c = 41.25$ cm^3.

where the liquid column goes down with a spherical cap whose contact angle varies from 90^o to 105^o and rises up with an inverted meniscus where $73^o \leq \theta_e \leq 90^o$ in the case of $N_c = 1.42$.

2.4.2 Effects of the chamber volume, gas input and needle radius

The effect of the chamber volume in the bubble generation process can be observed in Figs. 2.4(a)-(d) where, for a pair of Bond and Weber numbers, the difference between the maximum and minimum pressure inside the gas chamber during the formation stage decreases and the bubbling time increases as the volume of the gas chamber increases. For larger gas chambers, the pressure difference during the bubbling process would keep decreasing until eventually it would remain constant, achieving the constant pressure injection conditions. This effect of V_c on the evolution of the chamber pressure manifests on the formation of larger bubbles with increasing values of the chamber volume.

Figure 2.6 displays the evolution of the dimensionless bubble volume and chamber pressure obtained experimentally for the chamber of volume $V_c = 41.25$ cm^3 and two different needles allowing, thus, to analyze the effect of the Bo and gas flow, Q_i, on the bubble formation process. In this figure t_h^* indicates the dimensionless holding time, i.e. the time at which the holding stage finishes. Moreover, Figs. 2.6(a) and (b) show that, for a given Bond number, the bubble volume increases with Q_i although the gas flow rate injected is lower than the critical one, $Q_c = \pi(16/3\, g^2)^{1/6}\,(\sigma a/\rho_l)^{5/6}$ [102]. It should be noted that the formation time, i.e. the duration of the formation stage given by $(t_p^* - t_h^*)$[1], barely changes with Q_i, although larger bubbles are formed as Q_i increases because the maximum chamber pressure also increases, inducing a larger flow rate towards the bubble. Indeed, during the formation stage, the bubble growth rate is much faster than the flow rate of gas injected into the chamber, $dV_b(t)/dt \gg Q_i$, demanding a gas flow rate from the chamber that must satisfy $V_b(t_p) = Q_i\, t_p = \int_{t_h}^{t_p} G(t)/\rho(t)\, dt$, with $t_p - t_h \ll t_p$. However, the bubble formation frequency, given by $1/t_p$, increases with increasing gas flow rates since the holding time, t_h, diminishes, pressurizing the gas chamber more rapidly as shown in Figs. 2.6(c) and (d). Furthermore, the effect of Q_i on the bubble size is more apparent at larger Bond numbers although, in these cases, the bubble volume increases until it achieves a maximum value and starts to decrease. This decrease in the bubble volume is produced because its pressure becomes larger than that of the chamber, inducing a reverse flow from the bubble to the gas chamber. In addition, Figs. 2.6(e) and (f) exhibit the pressure-volume curve for the three gas flow rates at $Bo = 0.024$ ($N_c = 5.16$) and $Bo = 0.089$ ($N_c = 1.42$) respectively. It is shown that the chamber pressure decreases linearly with the bubble volume, with a slope that depends on N_c and barely changes with Q_i.

Four cases, described in table 2.1, have been selected to analyze the evolution of the bubble volume and shape during the formation process. In general, although the Weber number, $We = \rho_l Q_i^2/(\pi^2 a^3 \sigma)$, is always lower than the critical value, $We < We_c = (16/3)^{1/3} Bo^{-2/3}$, i.e. the gas flow rate is lower than the critical one $Q_i < Q_c$, the bubble volumes obtained are larger than the Fritz volume, except in case C for which $N_c = 0.39 < 0.85$. Moreover, for a given Bond number, the bubble volume increases with the chamber volume, as already pointed out by [69, 153, 4]. However, although, for $N_c > 0.85$, the bubble volume increases also with the needle diameter (cases B and D where $V_c = 41.25$ cm^3), as reported by Terasaka & Tsuge[153, 164], in the case of a small chamber (cases A and C where $V_c = 11.25$ cm^3) the bubble volume decreases with the needle diameter since $N_c < 0.85$ in case C. Similar effects were reported by Barker &

[1] Here $t_h^* = t_h/t_c$ and $t_p^* = t_p/t_c$ denote the dimensionless holding and pinch-off times respectively.

Case	A	B	C	D
V_c (cm^3)	11.25	41.25	11.25	41.25
V_b (mm^3)	51.61	85.39	25.13	107.20
Frequency (1/s)	9.65	6.18	20.46	4.90
Q_c (ml/min)	63	63	109	109
N_c	1.41	5.16	0.39	1.42
V_b^*	2.63	4.40	0.68	2.90
Bo	0.024	0.024	0.089	0.089
We	4.74	4.74	0.70	0.70
We_c	21.01	21.01	8.90	8.90

Table 2.1: Experimental characteristics of four typical cases performed with two chambers and two different needle where air is injected at a flow rate $Q_i = 30$ ml/min.

Nevers [9] in the formation of bubbles from an orifice associated to a transition from a small to a medium chamber.

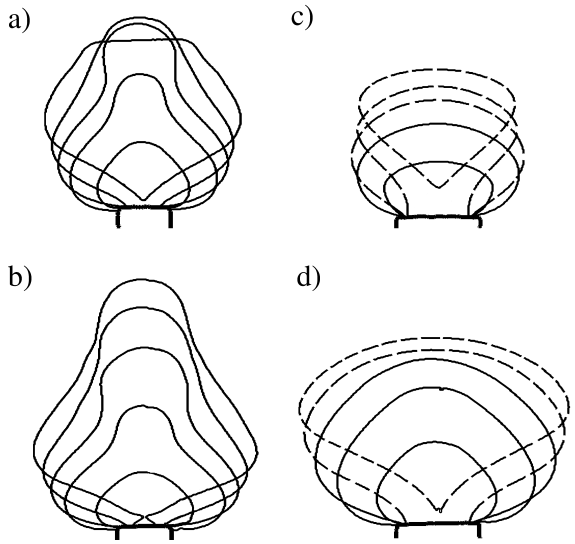

Figure 2.7: Sequence of bubble shapes during the formation stage for the cases A, B, C and D reported in Table 2.1, corresponding to times $(t^* - t_h^*)/(t_p^* - t_h^*)$= 0.2, 0.4, 0.6, 0.8 and 1. Here t_p^* and t_h^* are the dimensionless pinch-off and holding times respectively.

Figure 2.7 shows the time evolution of the bubble shape adopted during the formation stage for the four cases reported in table 2.1. It can be observed the different shape evolutions in cases A and B, where $We = 4.74$, from those associated to cases C and D where $We = 0.7$. In particular, while in cases C and D the bubble grows adopting an almond-like shape, in cases A and B the bubble elongates vertically forming a nipple on its tip due to the overpressure generated by the impact of the air jet discharging into the bubble. This effect can be better analyzed in terms of the instantaneous Weber number, $We_{inst} = G(t)^2/(\rho(t)\pi^2\, a^3\sigma)$, shown in Fig. 2.8. In cases A and B the instantaneous Weber number becomes larger than one, indicating that inertial effects inside

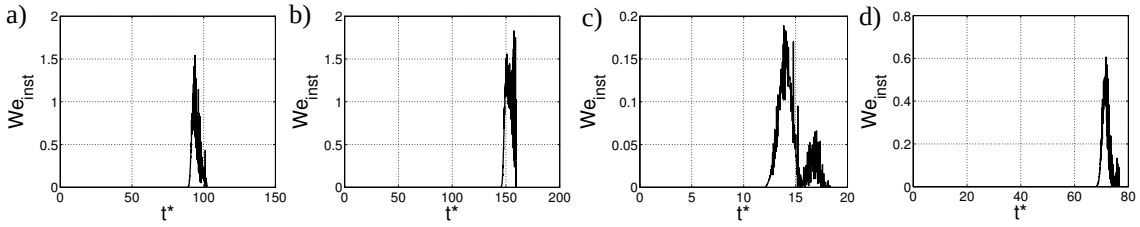

Figure 2.8: $We_{inst}(t)$ during the formation stage for cases A, B, C and D reported in Table 2.1.

the bubble become relevant with respect to surface tension effects. However, in cases C and D the momentum of the air jet feeding the bubbles is very small compared to surface tension, with values of the instantaneous Weber numbers much lower than unity. Consequently, the bubble adopts a more rounded shape with a flatter top. In addition, in cases C and D, the chamber pressure decreases below the bubble pressure during the formation time, inducing a reverse flow from the bubble to the chamber. The bubble silhouettes corresponding to times in which the bubble volume decreases due to the reverse flow are displayed in Fig. 2.7 with dashed lines, and can be identified by the secondary peaks shown in Figs. 2.8(c) and (d).

2.5 Conclusions

The present chapter of this dissertation describes the bubble formation process from a submerged vertical needle under coupled conditions, both by means of experiments and theoretical analysis. Specifically, four feeding chambers of volumes $V_c = 11.25$, 21.25 31.25 and 41.25 cm^3, and two needle of radii, a= 0.42 and 0.81 mm, have been assessed under different gas injection flow rates, Q_i. Although the former constitutes a widely extended bubble formation process in industry, there are still many issues regarding the physics governing the problem to be addressed given its complexity.

On the one hand, a theoretical model has been proposed to analyze the bubble formation process including the liquid flow inside the injection needle. This process can be divided into two phases, namely a holding and a formation stage of time spans t_h and $(t_p - t_h)$ respectively. As in the generation of bubbles from an orifice, the gas at the chamber pressurizes during the holding stage through a polytropic process. However, while the gas-liquid interface anchors at the orifice and the chamber pressure increases linearly in the case of bubble formation from orifices, when an injection needle is used the chamber pressure evolves differently, being necessary to take into account the flow dynamics inside the needle. In the case at hand, after the pinch-off of the previous bubble, the liquid meniscus travels down the needle towards the chamber, contributing to increase the pressure inside the gas chamber. At some point, the chamber pressure matches that of the liquid, pulling the water column upwards with an increasing velocity until eventually reaches the needle tip and initiates the formation of a new bubble. Furthermore, the contact angle has turned out to be also important, and varies throughout the holding stage as the water column moves. Thus, a time dependent contact angle model should be included for a more comprehensive model. Nevertheless, in general, the model predicts fairly well the time dependence of the chamber pressure during the whole bubble generation process within the operating conditions herein considered.

On the other hand, the influence of the main parameters governing the bubble formation process, namely the chamber volume, V_c, the gas flow rate feeding the chamber (gas input), Q_i, and the needle radius, a, has are also been assessed. Similar to the case of bubble formation from a submerged orifice, it has been found that the pressure variations decrease and larger bubbling times are induced for increasing chamber volumes, V_c, eventually reaching a constant pressure formation for sufficiently large chambers. The differences in time are more evident during the holding stage, i.e. larger holding times are required to increase the chamber pressure for larger chambers, whereas very similar formation times are found since the flow rate entering the bubble during the formation stage, $G(t)/\rho(t)$, becomes much larger than the gas input flow rate, Q_i, which induces very short formation times. In addition, larger bubbles are formed with larger chambers and for increasing values of the gas flow rate injected, although the effect of V_c (or similarly N_c) is more relevant than that of Q_i. The bubbling frequency also increases with Q_i, reducing significantly the holding time but barely affecting the duration of the formation stage. As for the influence of the needle radius, a, two bubble formation dynamics have been identified in conjunction with the chamber volume, V_c. For the smallest radius, a monotonic bubble growth occurs, being the chamber pressure larger than that of the bubble during the whole formation process. However, for larger needdle radii, the pressure inside the bubble may eventually become larger than that of the chamber, inducing a reverse flow of gas from the bubble towards the chamber, therefore reducing the bubble volume before its detachment. Finally, different bubble shape evolutions have been identified as a consequence of the varying instantaneous Weber numbers, We_{inst}, induced during the formation process.

To conclude, it is worth mentioning that the configuration at hand presents some advantages with respect to the generation of bubbles from submerged orifices, since contributes to pressurize the chamber avoiding the weeping phenomenon. The additional contribution to the chamber pressure increase may also lead to the generation of smaller bubbles under the same conditions although this conjecture needs to be corroborated in a future work.

CHAPTER
THREE

Numerical analysis of the rise motion of bubbles

In this chapter a numerical study on rising bubbles in still liquids employing the Volume of Fluid (VOF) technique to track the interface is presented. First, a combination of the correlation provided by Rastello *et al.* [116] for the rectilinear motion of a bubble with that given by Clift *et al.* [25] in the zig-zag ascension regime, conveniently made dimensionless, is proposed to determine the bubble terminal velocity for a wide range of bubble sizes and fluid properties. Furthermore, the crosspoint of both correlations gives the critical Weber number, $We_c = \left(\rho_l U_T^2 D/\sigma\right)_c$, at which the transition from a rectilinear to a zig-zag bubble motion takes place in a liquid of a given Morton number, $Mo = g\mu_l^4/\sigma^3\rho_l$. Concerning the numerical simulations, two different open source solvers have been evaluated, i.e. InterFoam and Gerris Flow Solver, to describe the motion of a stable bubble rising with a rectilinear path by performing two-dimensional axisymmetric simulations. The simulations show the presence of parasitic currents and variable results depending on the mesh resolution in the case of InterFoam, whereas no spurious results are observed in Gerris, which is therefore more suitable for these kinds of flows. Finally, the numerical results indicate that the gas properties hardly affect the bubble terminal velocity and shape, although they show that the flow field inside the bubble is highly affected by the gas density and viscosity. This result can be of relevance in heat and mass transfer processes where the mass diffusion or heat exchange can be enhanced by the convective motion induced inside the bubble.

This chapter is included in the paper "The use of Volume of Fluid technique to analyze multiphase flows: specific case of bubble rising in still liquids", by J.C. Cano-Lozano, R. Bolaños-Jiménez, C. Gutiérrez-Montes and C. Martínez-Bazán, published in the Appl. Math. Model. [20].

3.1 Introduction

The dynamics of fluid interfaces represents a matter of high interest due to its relevance, not only in multitude of industrial applications, but also in nature and even in daily life. In particular, multiphase systems constitute one of the most significant cases of study due to its wide application in numerous technological processes. The analysis of these kinds of problems involving interfaces has constituted a matter of extensive investigation by means of theory, experiments, and numerical simulations. Specifically, in the case of rising bubbles, since it is extremely difficult to obtain fine experimental results due to the complexity of controlling the experimental conditions and registering data without any interference or modification of the flow field, numerical simulations have become a relevant tool.

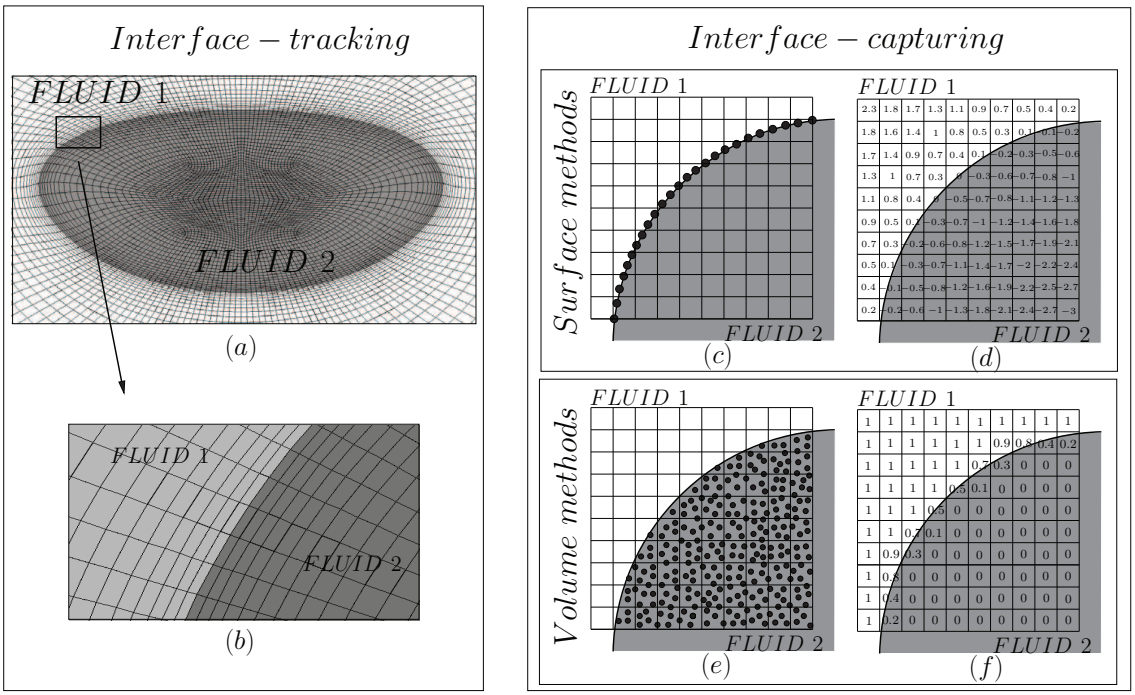

Figure 3.1: Schematic representation of interface-tracking and interface-capturing methods used to determine the interface in multiphase systems simulations. (a) Interface-Tracking method, (b) Detail of (a) near the interface, (c) Front Tracking (FT), (d) Level-Set (LS), (e) Marker and Cell (MAC), (f) Volume of Fluid (VOF).

The main features of multiphase systems include relatively large density and viscosity ratios, significant effect of surface tension forces, and complex interface geometries with free surfaces. The multiphase solvers must take these particularities into account in order to obtain accurate results, being the interface capturing one of the most important issues. In general, the numerical methods employed to solve interfaces are based on Finite Volume Methods (FVM) and can be classified into two categories: interface-tracking and interface-capturing methods [100] (see Fig. 3.1). Regarding the interface-tracking methods (Fig. 3.1a-b), they follow the motion of the interface with high precision [165]. The conservation equations are solved in each phase and are coupled across the interface, implementing the kinematic and dynamic conditions at the interface, which is defined as a sharp surface. Furthermore, each phase is solved in its own mesh, which deforms according to the interface movement. This method is limited to moderate interface deformations without topology changes, although this can be addressed applying topological changes and re-meshing of the domain. In addition, these methods present high computational costs associated with the mesh motion solver compared to others. As for the interface-capturing methods [135, 161, 167], they solve not only the continuity and momentum equations in both phases, but also an additional equation for a scalar or distance function, used as a phase indicator. Alternatively, marker-particles/grid might be used to determine the interface over a fixed grid. Moreover, different techniques can be employed in the interface-capturing methods, which can be classified into two main groups: surface and volume methods, as shown in Fig. 3.1(c)-(e). Concerning surface methods, several techniques can be employed, such as Front Tracking (FT) [23, 49, 112, 166, 160] or Level-Set (LS)

[143, 144, 136, 105]. In the FT technique, the interface is fitted using connected massless particles over the free-surface or a secondary moving grid to locate the interface in a Lagrangian way across an Eulerian mesh (Fig. 3.1c). Although in this algorithm the interface has a zero thickness, capturing interface deformations and topology changes can be troublesome. In the case of LS technique, the interface is defined as a zero level of a color function to identify the interface position (Fig. 3.1d). Same as FT, the interface is tracked accurately with a zero thickness, although mass is not always conserved. Regarding volume methods, several techniques are also available, such as the Marker and Cell (MAC) [54, 91] and the Volume of Fluid (VOF) techniques [59, 181, 118, 135], being the latter the most popular one. The MAC technique employs massless particles to identify the volume occupied by a fluid with free-surface (Fig. 3.1e), but it presents the disadvantage of the markers distribution in complex geometries and changes of topology. In the VOF technique, the interface is determined using a scalar indicator which varies between one (fluid 1) and zero (fluid 2), corresponding to the volume fraction occupied in each cell (Fig. 3.1f). As a consequence, a transport equation for the volume fraction parameter is additionally solved. Its main features are the conservation of mass and the ability of adaptation to rapid deformations and topological changes such as break-up and coalescence. However, as will be shown later, it presents some difficulties to advect the interface without diffusing and dispersing it and, consequently, the resulting interface is not as sharp as in other techniques.

Among all the mentioned methods and techniques, VOF constitutes the most widely used to solve interfaces due to the simplicity in its application, and will be the one employed in the present chapter of this dissertation. Regarding the schemes implemented for the discretization in the VOF method, low order schemes smear the interface, whereas high order ones produce numerical oscillations. At this point, several improvements to avoid these problems have been proposed, enhancing the accuracy of the calculation of the normal vector, as well as the interface reconstruction procedure, the curvature estimation algorithm, or the advection algorithm [47, 50, 107]. It should be also noted that this technique is dependent on the grid resolution, which might be source of errors in the advection and reconstruction algorithms. This drawback induces the so-called *artificial* or *numerical coalescence* of the disperse phase, preventing the real definition of the interface when the separation between two interfaces is smaller than the size of the computational cell. In this sense, the Adaptive Mesh Refinement (AMR) technique is employed to reduce this numerical error [168], providing a finer mesh in regions where there are large gradients or rapid changes of the physical variables, as it happens at the interface. As a consequence, the AMR technique allows the use of a coarse grid density in zones where the gradients are small [155, 173].

Furthermore, the calculation of the surface tension force constitutes a key issue of these methods, since its effects at the interface play a decisive role in multiphase flows. In most cases, the surface tension term is accounted in the momentum equation, using the Continuum Surface Force (CSF) model developed by Brackbill *et al.* [17]. Nevertheless, this model may introduce parasitic or spurious currents depending on the case study by [56, 73]. Several solvers have been developed to reduce these parasitic currents, although the problem has not been completely solved so far [63, 158].

Thus, with the aim at helping to select the proper and more efficient method, the particular

case of a single bubble rising inside a stagnant liquid with rectilinear trajectory has been investigated in this dissertation. This problem represents a case study in which resolving accurately the interface represents a task of a special importance. some open source solvers that implement the VOF technique for the interface treatment has been evaluated, as well as, to analyze the aforementioned disadvantages presented in these solvers, determining the CFD software that reachs better results compared with experimental data, requires lower computational cost, and avoids the appearance of numerical problems, such as the parasitic currents. The work is mainly focused on the simulation of stable bubbles, i.e. bubbles with axisymmetric flow, although the computations can be extended to bubbles in the vicinity of the unstable region.

This chapter is organized as follows: the main features of the numerical solvers employed in this chapter of the dissertation are described in section 3.2, and they are applied to the particular case of a bubble rising in still liquid in section 3.3. In particular, the numerical setup is described in subsection 3.3.2, showing an example of presence of parasitic currents in subsection 3.3.3. Next, the main numerical results are presenting in section 3.4. Finally, section 3.5 is devoted to the general conclusions.

3.2 Description of numerical solvers

In the present chapter, two different solvers implementing the VOF interface-capturing technique have been assessed, specifically, for the case of newtonian, incompressible, isothermal and immiscible fluids. Thus, a single set of continuity and momentum equations will be solved for both fluids,

$$\nabla \cdot \vec{v} = 0, \tag{3.1}$$

$$\frac{\partial \rho \vec{v}}{\partial t} + \nabla \cdot (\rho \vec{v}\vec{v}) = -\nabla p + \nabla \cdot \overline{\overline{\tau}} + \sigma\, k \nabla \gamma + \rho\, \vec{g}, \tag{3.2}$$

together with a transport equation for the volume fraction [59], γ, given by

$$\frac{\partial \gamma}{\partial t} + \nabla \cdot (\gamma \vec{v}) = 0. \tag{3.3}$$

In Eqs. (3.1)-(3.3), $\vec{v} = \vec{v}_l \gamma + \vec{v}_g (1-\gamma)$ is the velocity field defined as a weighted velocity, based on the distribution of the volume fraction, where $\vec{v_l}$ and $\vec{v_g}$ denote the velocity of the liquid and the gas phase, respectively, t is the time, p is the static pressure, $\overline{\overline{\tau}}$ is the viscous stress tensor, $\overline{\overline{\tau}} = \mu\,[\nabla \vec{v} + (\nabla \vec{v})^T]$, σ is the surface tension coefficient, assumed constant, k is the mean local curvature at the interface, and $\vec{g}$ represents the gravity acceleration. The fluid properties, i.e. density, ρ, and viscosity, μ, are computed as a function of the volume fraction (linear interpolation) as

$$\rho = \rho_l \gamma + \rho_g (1-\gamma), \tag{3.4}$$

$$\mu = \mu_l \gamma + \mu_g (1-\gamma), \tag{3.5}$$

where subscripts l and g represent liquid and gas phase, respectively. The particular features of the two open source solvers employed in this work, namely, Gerris and InterFoam, are briefly presented below.

3.2.1 Gerris Flow Solver

This CFD sotfware[1] is an open source code which resolves the time-dependent incompressible Navier-Stokes equations, Eqs. (3.1)-(3.2), and implements a piecewise-linear VOF advection scheme for the simulation of multiphase flows, using the traditional VOF Eq. (3.3) [111]. Gerris implements a quad/octree AMR method for spatial discretization [68], relevant to flows where different scales governing the problem are present. Therefore, the domain, a regular Cartesian grid, is discretized into quad/oct finite volumes organized hierarchically as a quadtree, octree in the three-dimensional space. The quad/octree grid generation involves the subdivision of each square cell into four/eight equal size child cells in each refinement level. Consequently, Gerris allows a dynamic adaptive mesh refinement along the interface (Fig. 3.2), as well as by means of any other criterion, such as the curvature or the vorticity magnitude, achieving the necessary resolution for accurate solutions at the key regions, without a significant global increment of cells.

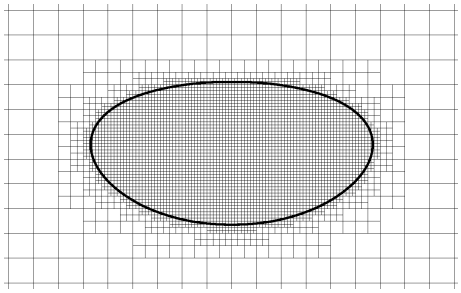

Figure 3.2: Detail of the mesh resolution during the bubble numerical simulation implementing quad/octree AMR technique. The mesh resolution is updated dynamically during the simulation in accordance with the motion of the interface. Solid line shows the interface for $\gamma = 0.5$.

As previously mentioned, the surface tension force computation constitutes a very important issue in multiphase flows simulations. To this aim, Gerris implements a generalized height-function (HF) formulation to estimate the mean local curvature, k, which assures second-order accuracy from VOF fields. In addition, the aforementioned solver is coupled with a balanced-force continuum formulation [43, 111], that guarantees an exact equilibrium solution irrespective of the spatial resolution and it prevents the generation of spurious currents [44]. Finally, second-order discretization schemes are used both for time and space, and the time step is limited by fixing the value of the Courant-Friedrich-Lewis (CFL) number in order to ensure the numerical stability [110, 111].

3.2.2 InterFoam implemented in OpenFOAM

This is a multiphase solver included in OpenFOAM[2] (Open Field Operation and Manipulation), a CFD open source package, which implements the VOF technique, within non-uniform, static meshes. In addition to Eqs. (3.1)-(3.2), it also resolves a modification of the classic transport

[1] The Gerris Flow Solver. http://gfs.sourceforge.net/wiki/index.php
[2] OpenCFD Ltd, http://www.openfoam.com/

equation for γ (Eq. 3.3),

$$\frac{\partial \gamma}{\partial t} + \nabla \cdot (\gamma \vec{v}) + \nabla \cdot [\gamma(1-\gamma)\vec{v}_r] = 0, \tag{3.6}$$

which implements the interface compression term proposed by Rusche [121], being $\vec{v}_r = \vec{v}_l - \vec{v}_g$ the relative velocity between both fluids. The above equation includes an additional term in relation to Eq. (3.3), which is only active at the interface region and which acts as a surface compression term, thus improving the interface resolution and limiting the smearing of the interface.

To account for the surface tension force, InterFoam implements the Continuum Surface Force (CSF) proposed by Brackbill [17], computing the local curvature, k, as a function of the volume fraction gradient, $-\nabla[\gamma/|\gamma|]$. Finally, in the present solver, second-order schemes have been mainly used both for the temporal and the spatial terms, as the time step is also limited by setting the CFL number. A detailed information about the InterFoam solver can be found in [11, 31, 52, 121].

3.3 Case study: bubble rise inside a still liquid medium

The correct numerical resolution of the problem of a bubble rising in still liquid is extremely sensitive to the real bubble shape, as it will be shown in the next Chapter 4. Therefore, in this section, the physics of the problem is first properly described and characterized using the available results in the literature. Then, the numerical solvers described in the previous section are thoroughly applied to this particular case with the purpose of obtaining a realistic solution. Next, the results of both solvers are compared and evaluated, with one of them selected as the most appropriate for this work. Finally, the selected solver is validated and used to analyze in detail the problem at hand.

3.3.1 Physical problem characterization

The rising of a bubble within a quiescent liquid constitutes one of the most important and canonical problems of multiphase flows. Depending on the physical properties, bubbles can undergo changes in their shape and trajectory during the rising process. These features have been shown since the early 50's to depend on the main characteristic dimensionless parameters, namely the Reynolds number, $Re = \rho_l U_T D/\mu_l$, the Bond number, $Bo = \rho_l g D^2/\sigma$, and the Morton number, $Mo = g\mu_l^4/\sigma^3\rho_l$, where $D = (6V/\pi)^{1/3}$, represents the equivalent diameter of a bubble of volume V, whose terminal velocity is U_T [13, 25, 53].

One of the methods commonly used to characterize the bubble rise inside a liquid is by looking into its terminal velocity, which determines the different behaviors presented in this problem. In this regard, although many experimental studies have been performed on this topic [76, 182], the work by Maxworthy *et al.* [88] will be focused here. Some of these results are plotted in Fig. 3.3(a), where the same general behaviour can be observed for all the series shown ($Mo < 10^{-3}$). For small values of D, the bubbles follow a rectilinear path with a steady motion, characterized by a monotonic increase of U_T with D. For larger values of D, a local maximum U_T is reached, which,

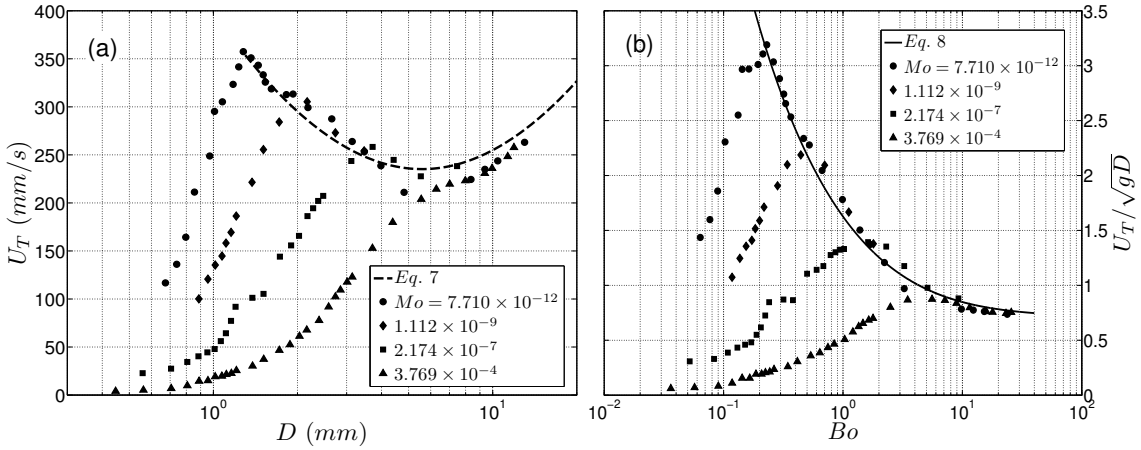

Figure 3.3: (a) Evolution of the dimensional terminal velocity, U_T, as a function of the bubble equivalent diameter, D. Symbols represent experimental data by Maxworthy *et al.* [88] corresponding to different Mo, and the line is the prediction of Eq. (3.7). (b) Same experimental data in dimensionless variables, together with Eq. (3.8).

according to Maxworthy *et al.* [88], indicates a change in the bubble rise from rectilinear to zig-zag/spiral path[3]. Moreover, Clift *et al.* [25], in their Fig. 7.3, and Duineveld [34], also report that the maximum velocity corresponds with the onset from rectilinear to zig-zag bubble motion. This unsteady motion, which initially induces a U_T decrease with D, turns into a subsequent rise of U_T for even larger D, caused by the changes in the bubble shape. Finally, for bigger bubbles, $Bo \geq 40$, Wegener & Parlange [174] established that the bubbles presented a spherical-cap shape and a new trajectory change to a straight rocking path occurred. This behavior is valid for $Mo < 1.64 \times 10^{-3}$, while for larger values, Bhaga [12] determined that the motion was always stable. Furthermore, the wake behind the bubbles is related to the different bubble trajectories. In this way, ascending bubbles with straight path (considered stable) are characterized by the existence of an axisymmetric wake, whereas those with zig-zag or spiral trajectories (considered unstable) present the development of two-counter rotating trailing vortices with a plane of symmetry in the wake [30, 98].

These features have been also observed in the rise of air bubbles in water [8, 77, 125]. In this regard, Clift *et al.* [25] established an approximation for rising bubbles in clean water, valid for U_T within the zig-zag motion region, given by

$$U_T = \left[(2.14\,\sigma/\rho_l\,D) + 0.505\,g\,D \right]^{1/2}. \tag{3.7}$$

Equation (3.7) is based on the wave analogy equation proposed by Mendelson [93] for this region and has been represented in Fig. 3.3(a), together with the experimental results by Maxworthy *et al.* [88]. As can be observed, a good agreement is obtained, mainly for Mo close to that of the clean water ($Mo \simeq 3 \times 10^{-11}$). This equation can be made dimensionless, obtaining

$$U_T/\sqrt{gD} = \left(2.14\,Bo^{-1} + 0.505 \right)^{1/2}, \tag{3.8}$$

[3]Citing p. 438 on [88]: "Although the stability characteristics of the rise were observed no attempt was made to classify them except to note that unsteady bubble motion started just beyond the diameter which gave the maximum velocity of rise"

where the dimensionless terminal velocity, $U_T/\sqrt{gD}$, only depends on the Bo number. Therefore, if the experimental data in Fig. 3.3(a) are plotted in the dimensionless form, together with Eq. (3.8), the results displayed in Fig. 3.3(b) are obtained. It can be noticed that Eq. (3.8) crosses each experimental curve close to the corresponding maximum value of $U_T/\sqrt{gD}$. Although not included in Fig. 3.3(b) for clarity, additional experimental data reported in Clift *et al.* [25], as well as those from Zenit & Magnaudet [182], have been used to corroborate the aforementioned trend.

Moreover, in a recent study, Rastello *et al.* [116] proposed a correlation curve for the rising bubble Reynolds number as a function of the Weber, $We = \rho_l {U_T}^2 D/\sigma$, and Mo numbers, valid in the stable, rectilinear regime, which writes

$$Re = 2.05\, We^{2/3} Mo^{-1/5}. \tag{3.9}$$

Figure 3.4 shows the experimental data in Fig. 3.3, together with Eq. (3.9), plotted in the Re-($We^{2/3}Mo^{-1/5}$) plane. It can be observed that all data collapse onto a single line in a region until a certain value of $We^{2/3}Mo^{-1/5}$, which depends on Mo, is achieved. In fact, this region where the data collapse corresponds to the rectilinear path regime in Figs. 3.3(a)-(b), until the maximum terminal velocity is reached. Therefore, it can be noticed that Eq. (3.9) presents a good correlation for the cases corresponding to stable rectilinear paths, whereas it is not able to predict properly the Re once the bubble motion becomes unstable. Indeed, this fact can be also observed in Legendre *et al.* [76], where a good agreement between experimental data and Eq. (3.9) was found, but certain discrepancies were detected, mainly at high Re numbers. Nevertheless, if Eq. (3.8) is rewritten in terms of Re, We and Mo, one gets

$$Re = [We^2\,(We - 2.14)/(0.505\, Mo)]^{1/4}, \tag{3.10}$$

which, evaluated for different values of Mo, is able to provide the bubble Reynolds number in the unstable region, as shown in Fig. 3.4. In fact, note that the experimental data agree well with Eq. (3.10), e.g. $Mo = 7.71 \times 10^{-12}$, mainly for Mo close to that of pure water. Furthermore, it is noteworthy that the crosspoint between Eq. (3.9) and Eq. (3.10) determines the onset for the unstable motion, giving $We_c^{-2/3}(We_c - 2.14) = 8.92\, Mo^{1/5}$, where $We_c(Mo)$ represents the critical Weber number at which the transition from a rectilinear to a zig-zag motion occurs for a given Morton number. Notice that, $We_c(Mo)$ corresponds to the Weber associated to the bubble with maximum terminal velocity at any Morton number, displayed in Figs. 3.3(a)-(b). The previous correlation predicts $We_c = 2.14$ when $Mo \to 0$, and $We_c = 2.23$ for water ($Mo = 2.72 \times 10^{-11}$), which is in good agreement with the experimental value given by Maxworthy *et al.* [88] ($We_c = 2.30$). Therefore, Eq. (3.10) proposed in this work, together with Eq. (3.9), contribute to provide a more complete characterization of the bubble rising velocity.

The purpose of this chapter is to characterize the rising of bubbles both inside the stable region as well as close to the transition curve. Addressing this problem experimentally is extremely difficult, since sometimes it is necessary to introduce impurities or surfactants to visualize the flow, which alters the bubble terminal velocity and shape [146]. Under the aforementioned complexity, Computational Fluid Dynamics (CFD) codes have turned into useful tools to complement the state-of-the-art scientific knowledge on the matter. Thus, it is essential to take into account the particularities presented in this problem to obtain a realistic result with an optimal computational

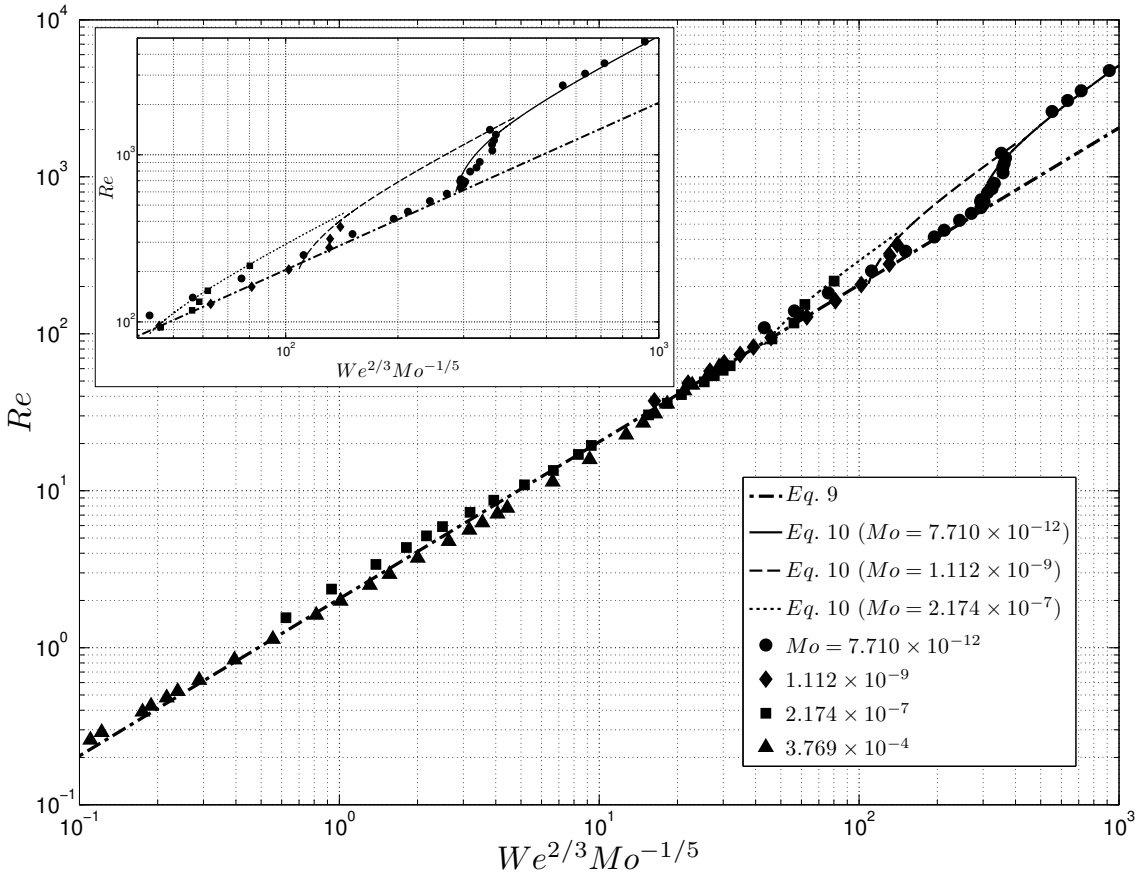

Figure 3.4: Experimental data by Maxworthy *et al.* [88], together with predictions of Eqs. (3.9) and (3.10) in the *Re*-$We^{2/3}Mo^{-1/5}$ plane. The inset shows the details around the transition point for three Morton numbers.

cost. In this context, the rise of stable bubbles (rectilinear path) can be simulated by imposing the axisymmetric boundary condition instead of performing three-dimensional numerical simulations, since it exhibits an axisymmetric wake. However, in the unstable regime, three-dimensional simulations are required since the bubble wake loses its axisymmetry and the results obtained with two-dimensional axisymmetric simulations would differ from the actual bubble behavior. Nevertheless, a complete characterization of the bubble instability regimes, performing three-dimensional numerical computations, is out of the scope of the present work. Another crucial aspect is to use a solver free of parasitic currents. Thus, the purpose of the presented study is to determine a suitable numerical solver and setup which allows a correct numerical study of this phenomenon in the stable region and in the neighborhood of the transition curve.

3.3.2 Problem setup

The size of the computational domain used in the simulations, shown in Fig. 3.5, was equal to $4D$ in the radial coordinate and $48D$ in the axial coordinate, large enough to guarantee that the results were not affected by the size of the domain, and similar to those used in other numerical

studies [61, 99, 167]. Smaller computational domains, of $4D \times 24D$, were also employed in those cases in which the steady conditions, mainly in terms of shape and terminal velocity, were reached sufficiently fast (cases discussed in subsection 3.3.3). Both, two-dimensional and three-dimensional numerical simulations were considered and compared, although mainly two-dimensional, axisymmetric simulations were conducted, due to the characteristics of the problem at hand, i.e., a bubble rising with a rectilinear path and presenting an axisymmetric wake. Therefore, the computational domain was enclosed by four boundaries, where different conditions were imposed, namely, non-slip condition at the bottom, zero normal velocity gradient and constant pressure at the top, slip condition at the outer cylinder, and axisymmetry at the cylinder axis. The bottom boundary condition actually represents the solid wall of a pool containing the liquid, although a free-slip condition was also assessed, providing the same result. The bubble, initially spherical ($D = 2$ mm) at rest, and placed $2.5D$ from the bottom, rises due to buoyancy, changing its shape, and eventually reaching a terminal rise velocity. The initial shape of the bubble had no effect on the final solution, as only cases at large Bo and Mo are affected by the initial condition [104]. Moreover, the chosen governing dimensionless parameters are the Bond and the Galilei, Ga, numbers, where $Ga = \rho_l\, g^{1/2}\, D^{3/2}/\mu_l = Re\,\sqrt{gD}/U_T = Bo^{3/4}/Mo^{1/4}$, which were varied within the ranges $0.1 \leq Bo \leq 100$ and $5 \leq Ga \leq 200$.

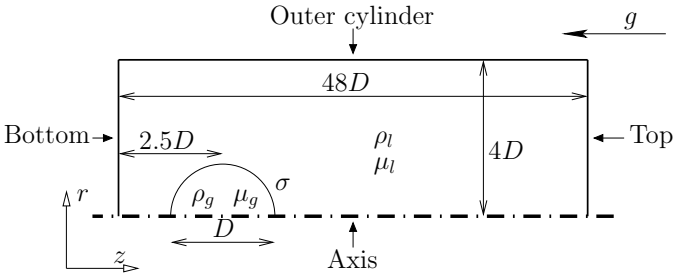

Figure 3.5: Sketch of the computational domain used in this study together with the physical parameters.

Regarding the computational mesh, a base grid of 8 cells/D with an AMR grid of 4 refinement levels at the interface and inside the bubble, achieving 128 cells/D, with a maximum number of near 1.6×10^5 cells, was used in the two-dimensional axisymmetric simulations performed with Gerris. The computational domain and spatial resolution used here are the same ones employed in Chapter 4, being selected as a function of the domain size assessment and grid sensitivity study, described in more detail in next chapter. In the case of InterFoam, two different resolution structured grids (within a computational domain of $4D \times 24D$), each composed by two uniform meshes, were used: first, a coarse mesh of uniform resolution equal to 64 cells/D, from the axis to $1.25D$, and 8 cells/D, from $1.25D$ up to the outer boundary, with 1.3×10^5 cells; and second, a fine mesh of uniform resolution equal to 128 cells/D, from the axis to $1.25D$, and the same resolution of the coarse one elsewhere, with 5.1×10^5 cells. Moreover, the number of cells inside the bubbles was larger than other previous numerical works, such as, Van Sint Annaland *et al.* [167], with 12 cells/D, or Hua & Lou [61], with 25 cells/D, among others. In all the simulations performed, the time step was controlled setting a maximum CFL number equal to 0.5.

3.3.3 Evaluation and comparison of the Gerris and InterFoam solvers: Parasitic currents

In the present section, the results obtained with the two above-mentioned solvers have been compared, focusing on the final bubble shape and terminal velocity, as well as on the existence of parasitic currents [73]. The latter, i.e. the generation of non-physical velocities of small amplitude near the interface region, which can oscillate temporally, is one of the most important drawbacks of the VOF technique, mainly in the case of surface tension dominated flows. The source of these spurious velocities is the imbalance between the pressure gradient and the surface tension terms at the interface, which can generate velocities of the order of those of the actual fluid flow, thus, producing instabilities and deformations in this region. These parasitic currents can be avoided or mitigated with high-spatial resolution grids and sophisticated discretization techniques [43, 117]. In the specific case of Gerris, it constitutes one of the first solvers reducing the spurious solutions to the machine precision [44, 111].

With the aim of evaluating and comparing both solvers, the particular case of a bubble with $Ga = 5$ and $Bo = 0.1$ has been simulated. For these parameters, the terminal velocity in terms of the Reynolds number is $Re = Ga\,U_T/\sqrt{gD} = 1.83$. These values have been selected since the low Re and Bo numbers region is more suitable for the appearance of parasitic currents [56]. Therefore, this constitutes one of the worst case scenarios, making it appropriate for its evaluation. Unlike in other similar studies, in the present work, the gravity acceleration has been considered, i.e. a dynamic problem has been solved, to mimic the real flow conditions. In short, since this case corresponds to a stable bubble, the actual rectilinear rise of a bubble with a low terminal velocity and high surface tension, i.e. quasi-spherical shape, has been analyzed by performing two-dimensional axisymmetric simulations.

Regarding the results from InterFoam, very different terminal velocities are obtained, depending on the mesh resolutions, $Re = 2.16$, for 64 cells/D, and $Re = 1.90$, for 128 cells/D. The latter agrees well with the prediction obtained using Gerris, with $Re = 1.83$, which does not vary regardless of the grid resolution. As for the parasitic currents, Fig. 3.6 shows the results obtained for the final shape and dimensionless relative velocity field, $(\vec{v} - U_T\,\vec{e_z})/\sqrt{gD}$. In both simulations performed with InterFoam, Fig. 3.6(a)-(b), the presence of spurious solutions is observed, with the intensity being larger in the case of the coarser mesh. As can be observed in Fig. 3.6(a), these velocities induce the generation of artificial recirculations, which modify the flow field and can distort the bubble shape. The intensity of the spurious velocities decreases as the grid resolution is increased, Fig. 3.6(b), since the local curvature near the interface is better resolved [70]. However, their complete mitigation cannot be fully accomplished, and the CPU time increases considerably as the grid cells are reduced (i.e the computational time needed to obtain the results shown in Fig. 3.6b, with a fine grid, is 6 times larger than that taken when the coarse grid is used, Fig. 3.6a).

In the case of Gerris, shown in Fig. 3.6(c), it is worth mentioning the absence of parasitic velocities, with a much lower number of cells and a CPU time required of only 2.3 times the one of the coarse grid in InterFoam. It must be pointed out that the CPU time is also affected by the time step, limited by a maximum CFL number of 0.5, with the time steps being equal to

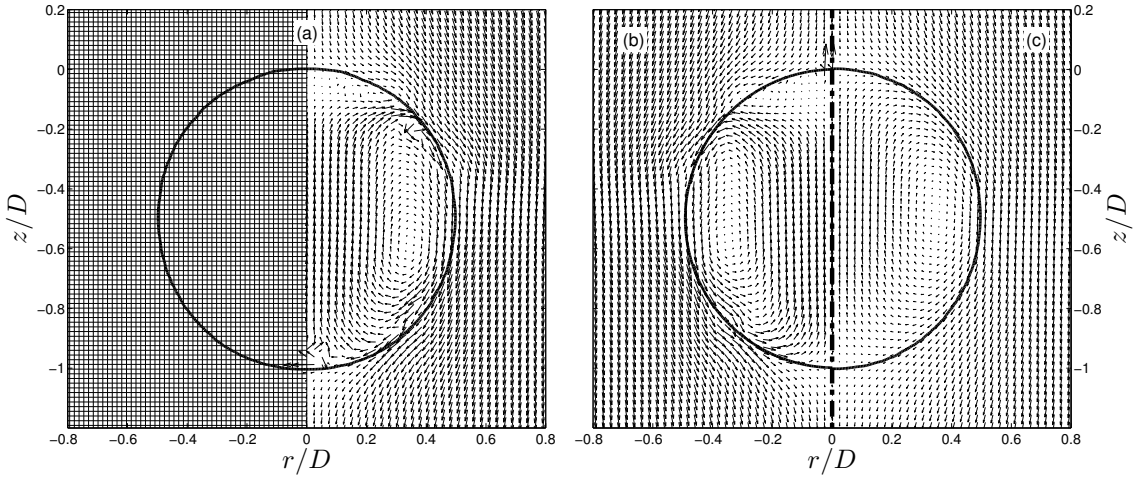

Figure 3.6: Dimensionless relative velocity field, $(\vec{v} - U_T\,\vec{e_z})/\sqrt{gD}$, computed with InterFoam in a coarse (right half of Fig.3.6a) and a fine mesh (b) for a bubble with $Ga = 5$ and $Bo = 0.1$. Recirculations observed on the bubble interface clearly illustrate the presence of parasitic currents. The detail of the coarse mesh near the bubble has also been included (left half of Fig. 3.6a). The solution from Gerris, which does not exhibit spurious velocities, is shown in (c).

1.4×10^{-5}, 6.4×10^{-6}, and 1.2×10^{-6} seconds, for the two InterFoam meshes (coarse and fine) and the Gerris mesh, respectively. Furthermore, the final shape of bubbles are practically identical, although local distortion effects are expected to influence the solution in case of larger computing times. Therefore, the above results clearly show that the AMR technique and the surface tension treatment implemented in Gerris are more suitable in the case at hand. Subsequently, Gerris solver will be used from now on. For further VOF studies on parasitic currents in surface tension dominated flows simulated with InterFoam see Albadawi *et al.* [2] and Klostermann *et al.* [70].

3.4 Results

The present section shows the results obtained for the rectilinear bubble rise in still fluids computed with Gerris Flow Solver. First, two-dimensional and three-dimensional simulations are compared to confirm the suitability of the former ones to simulate stable bubbles. Next, the results obtained from two-dimensional axisymmetric numerical simulations are presented and correlated with Eq. (3.9), validating the numerical procedure, which finally is used to analyze the influence of the inner bubble gas on the rising dynamics, considering both density and viscosity.

3.4.1 Comparison of two-dimensional axisymmetric and three-dimensional numerical simulations

Previous to the presentation of the results herein reported and obtained from two-dimensional, axisymmetric numerical simulations, the present subsection compares the results from three-dimensional as well as two-dimensional axisymmetric computations, using the exact same spa-

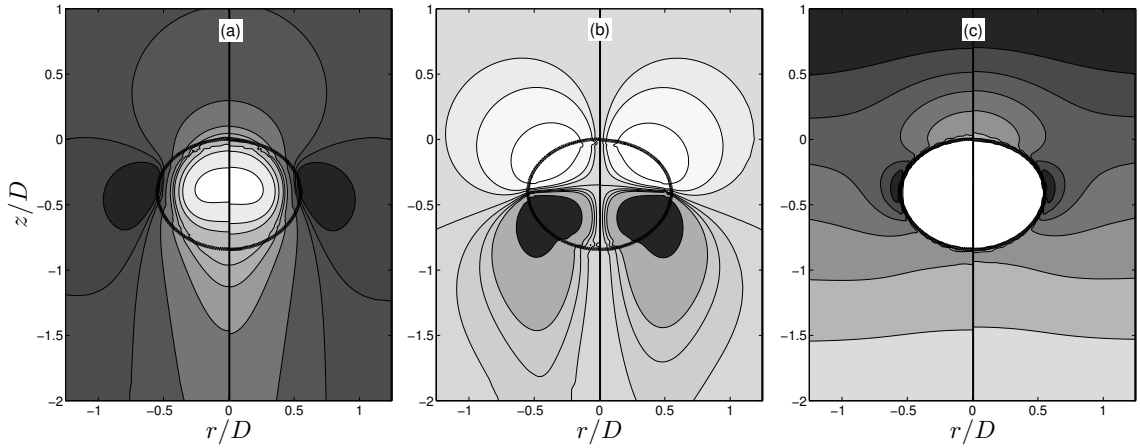

Figure 3.7: Two-dimensional axisymmetric (left half) and three-dimensional numerical simulations (right half) corresponding to a bubble with $Ga = 50$ and $Bo = 1$. Bubble shape and isocontours of dimensionless (a) axial velocity [-2 -1.6 -1.5 -1.4 -1 -0.5 -0.25 -0.1 0.25 0.5 1], from dark to light, (b) radial velocity [-1 -0.25 -0.1 -0.07 -0.04 0 0.08 0.15 0.4] and (c) pressure, $p/(\rho_l g\, D)$, [1 1.5 1.8 2.1 2.5 3 3.5 5].

tial resolution, of a stable bubble ($Ga = 50$ and $Bo = 1$). This study has been conducted with the aim of ensuring that the two-dimensional assumption had no effect on the results. From the numerical simulations, the terminal velocity, obtained in terms of Re, was equal to 73.76 and 74.87, respectively, and the aspect ratio, χ, equal to 1.30 and 1.31, with a maximum discrepancy of 1.49%. Detailed results can be observed in Fig. 3.7, which shows the dimensionless axial and radial relative velocity components, as well as the pressure iso-contour fields, together with the bubble shape obtained from both types of simulations. It can be observed that the results obtained from the two-dimensional, axisymmetry simulations (left half) are nearly identical to those given by the three-dimensional ones (right half). It is noteworthy to point out that the dimensionless parameters of the simulated bubble are also close to the stable/unstable trajectory transition, thus corroborating the validity of the assumption of axisymmetry. Moreover, when the two-dimensional axisymmetric simulations are conducted, a large amount of CPU time is saved as, in this case, the CPU time per simulated second is 8.68 hours/second, whereas, in the case of the three-dimensional simulations is 4151.24 hours/second, 478 times larger. This CPU time reduction is even larger if one takes into account that, for the above simulations, a 2 cells/D base, with a 4 level AMR (32 cells/D), grids have been used, whereas the spatial resolution of the results presented next corresponds to a 8 cells/D base, with a 4 level AMR grid (128 cells/D).

3.4.2 Terminal velocity and real bubble shape. Numerical method validation

A key issue of the rising motion of a bubble is the proper simulation of the final flow dynamics. In the present work, a conservative criterion has been considered, focusing on the prediction of constant bubble terminal velocity and shape. Figure 3.8 shows the temporal evolution of the terminal velocity and shape of a rising spherical bubble initially at rest, corresponding to three different coupled values of (Ga,Bo), namely $(174.14, 0.23)$, $(85.45, 3.21)$ and $(50, 20)$. From the left column

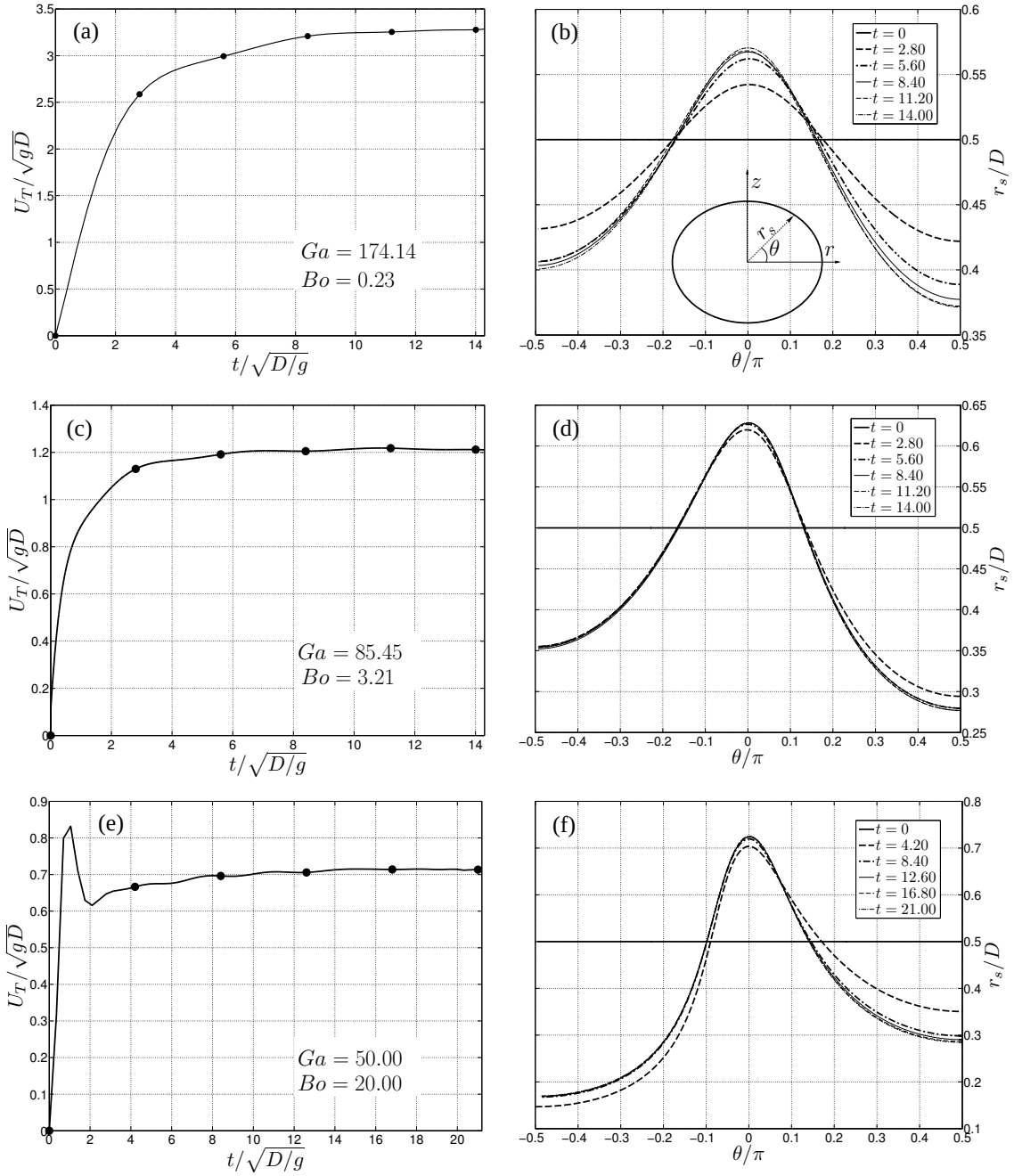

Figure 3.8: (a) Temporal evolution of the dimensionless terminal velocity, $U_T/\sqrt{gD}$, obtained for a bubble with $Ga = 174.14$ and $Bo = 0.23$, (b) Bubble shape corresponding to the six instants marked with symbols in (a). The shape is characterized by the distance to the interface, r_s, and the angle from the major diameter, θ (see sketch). As can be observed, the first instant presents a spherical shape (horizontal line at $r_i/D = 0.5$). (c) and (d) show the same information as (a) and (b), respectively, for $Ga = 85.45$ and $Bo = 3.21$. (e) and (f) show the equivalent results for $Ga = 50$, $Bo = 20$.

in Fig. 3.8, bubbles are observed to undergo a velocity increase in the early stages, until reaching an asymptotic value which barely varies with time. The time for which the asymptotic terminal velocity is achieved depends on the specific dimensionless parameters. Moreover, it is noteworthy that, as the rise velocity evolves to its final value, the bubble shape adapts to its final form. This fact is illustrated in the right column of Fig. 3.8, where the bubble shape temporal evolution for six different times is shown, corresponding to the markers represented in Figs. 3.8(a), (c) and (e). Here, the bubble shape has been characterized as a function of r_s and θ (polar coordinates), being r_s the distance from the bubble centre to the interface, and θ the angle from the major diameter (see sketch in Fig. 3.8b). As can be observed in Figs. 3.8 (b),(d),(e), the bubble shape, which is initially spherical, becomes flatter as it rises. It is worth mentioning that, even when the final velocity is reached, small variations in shape still occur, therefore, being both parameters essential to monitor, differently from most of the studies which usually account only for the terminal velocity. Furthermore, the accurate prediction of the final shape is of great importance since it determines the surrounding flow, as well as the generation of azimuthal vorticity responsible for the recirculation region and the onset of the path transition.

Finally, with the aim of validating the numerical method, Fig. 3.9(a) shows the results of the dimensionless terminal velocity, $U_T/\sqrt{gD}$, as a function of the Bo number for different values of Ga, in the range $5 \leq Ga \leq 200$, together with the correlation proposed in Eq. (3.10). Since the correlation denotes the transition region, the simulations have been performed within the stable region (open symbols), as well as close to the transition limit (solid markers). The experimental data by Veldhuis [170] and Zenit & Magnaudet [182, 183], corresponding to the region near the transition, have been also simulated and compared in this plot ($\star$). As can be observed, a good agreement has been found between Eq. (3.10) and the solid symbols, validating thus the numerical results obtained in this work. Besides U_T, a good agreement is also obtained for the shape, evaluated in terms of the aspect ratio χ (major-to-minor diameter ratio), with discrepancies always lower than 5%, as it will be shown in next Chapter. Moreover, the area placed on the right side of the dashed line in Fig. 3.9(a) determines the region of spherical-cap bubbles, $Bo \geq 40$, characterized by a straight rocking path [174]. Therefore, the zone delimited between both solid and dashed lines corresponds to bubbles with an unstable motion (zig-zag and spiral trajectories), for which three-dimensional simulations would be necessary. Furthermore, the numerical results in Fig. 3.9(a) have been also compared with Eq. (3.9) in Fig. 3.9(b), where results are plotted in the Re-$We^{2/3}Mo^{-1/5}$ plane. As can be noticed, the numerical results adequately correlate with Eq. (3.9).

As already mentioned above, the unsteady zig-zag region is characterized by the loss of axisymmetry of the wake, and the subsequent change in the terminal velocity, as shown in Fig. 3.4 in terms of the bubble Reynolds number. Therefore, two-dimensional axisymmetric simulations would eventually provide unphysical solutions in the unstable regime. Consequently, if the bubble We is lower than $We_c(Mo)$ the two-dimensional simulations are adequate to describe the bubble motion, otherwise one should perform three-dimensional computations. However, two-dimensional simulations will still be able to describe the bubble motion in the unstable regime, near the transition region, $We \simeq We_c$, since the changes in bubble shape and terminal velocity are small. On the other hand, if axisymmetric simulations are performed at $We > We_c$, terminal velocities, expressed

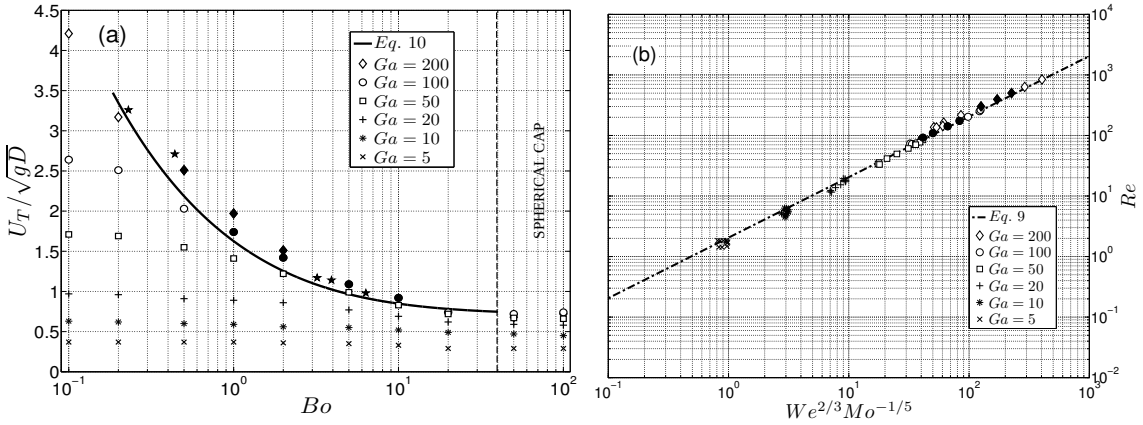

Figure 3.9: (a) Dimensionless terminal velocity as a function of Bo number. Symbols correspond to the numerical results for different values of Ga in the stable region (open symbols) and near the transition (solid symbols). Experimental data by other authors [170, 182, 183] have been also plotted ($\star$). Solid line represents Eq. (3.10), and dashed line determines the spherical-cap region ($Bo \geq 40$). (b) Comparison of the same results in terms of Re and ($We^{2/3}Mo^{-1/5}$) (symbols) with Eq. (3.9).

in terms of the bubble Reynolds number, given by Eq. (3.9) will be obtained, while the correct velocity follows Eq. (3.10) when the bubbles fall within the unstable regime. In fact, in the unstable region, the bubble wake is no longer axisymmetric and develops two counter-rotating vortices with a symmetry plane, representing a flow field not possible to describe with two-dimensional simulations. Thus, three-dimensional simulations of the unstable case will provide bubble terminal velocities in accordance with Eq. (3.10) if the are correctly performed.

3.4.3 Effect of the inner gas

In the present subsection, the effect of the inner gas physical properties on the bubble rise dynamics has been evaluated, by varying the gas-to-liquid density, $\lambda = \rho_g/\rho_l$, and viscosity, $\beta = \mu_g/\mu_l$, ratios. In the study, The study has not only been focused in the bubble shape and terminal velocity, but also on the possible changes in inner and outer velocity fields.

To analyze the effect of the inner flow density, $\lambda = \rho_g/\rho_l$ values ranged from 1.28×10^{-4} to 1.28×10^{-1}, have been studied. The simulations have been conducted for a bubble with $Ga = 99.35$ and $Bo = 3.92$ [183], where only the gas density has been varied for $\beta = 4.21 \times 10^{-3}$. Similar works have been conducted by Chen *et al.* [22] and Hua & Lou [61], among others, although they only studied the effect on the shape and terminal velocity.

Table 3.1 shows the results obtained for the terminal velocity, in terms of the Re number, and the final bubble shape, in terms of the aspect ratio, χ, together with the corresponding differences with respect to the case of minimum λ. In general, it can be observed that the terminal velocity decreases as λ increases, since the buoyancy forces, which are of the order of $\rho_l(1-\lambda)$, also become lower. Moreover, it can be observed that this change of Re is hardly significant for the lowest values of λ, whereas for $\lambda = 1.28 \times 10^{-1}$, a 5% difference is obtained, which is also related to a

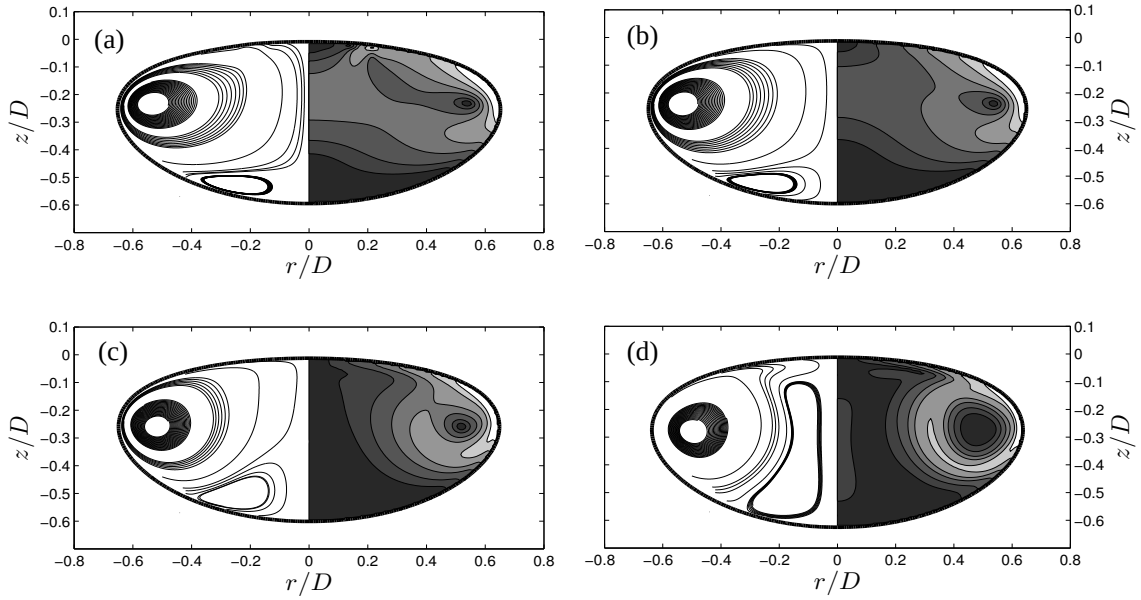

Figure 3.10: Bubble shape together with the streamlines (left half) and dimensionless relative velocity contours (right half) inside the bubbles, for $\beta = 4.21\times10^{-3}$, and different density ratios (a) $\lambda = 1.28\times10^{-4}$, (b) $\lambda = 1.28 \times 10^{-3}$, (c) $\lambda = 1.28 \times 10^{-2}$, and (d) $\lambda = 1.28 \times 10^{-1}$, for a bubble with $Ga = 99.35$ and $Bo = 3.92$. The values of the velocity isocontours, from dark to light, are [0, 0.1, 0.2, 0.35, 0.5, 0.75, 1].

	a)	b)	c)	d)
λ	1.28×10^{-4}	1.28×10^{-3}	1.28×10^{-2}	1.28×10^{-1}
Re	117.53	115.97	115.60	111.68
$E_{Re}\%$	-	1.33	1.65	4.97
χ	2.24	2.21	2.21	2.09
$E_{\chi}\%$	-	1.03	1.03	6.70

Table 3.1: Re and aspect ratio, χ, obtained for the four values of the gas-to-liquid density ratio, λ, for $\beta = 4.21 \times 10^{-3}$, $Ga = 99.35$ and $Bo = 3.92$. E_{Re} and E_{χ} represent the relative difference with respect to Re and χ corresponding to the case of lowest λ.

change in the bubble shape, as next commented. However, this last case would represent a rising drop instead of a bubble, as this value can only be found for pairs of liquids. These effects, mainly in terms of the bubble shape, are of high importance, as they have direct impact on the outer vorticity field and the consequent induced trajectory.

Regarding the bubble shape, notice that the aspect ratio decreases with λ, indicating that the bubble becomes more rounded as λ increases, but the variations are even lower than those found in Re for small λ, and significant differences, of the order of 7%, are observed only for $\lambda \geq 1.28\times10^{-1}$. In Figs. 3.10(a)-(d), the resulting interface contours are represented for each case. Although difficult to visually detect, a displacement of the location of maximum curvature takes place, mainly for the case with largest λ. This can more clearly be observed in Fig. 3.11, where the bubbles interfaces are displayed as a function of θ, as in Fig. 3.8(b). It can be observed that, while the

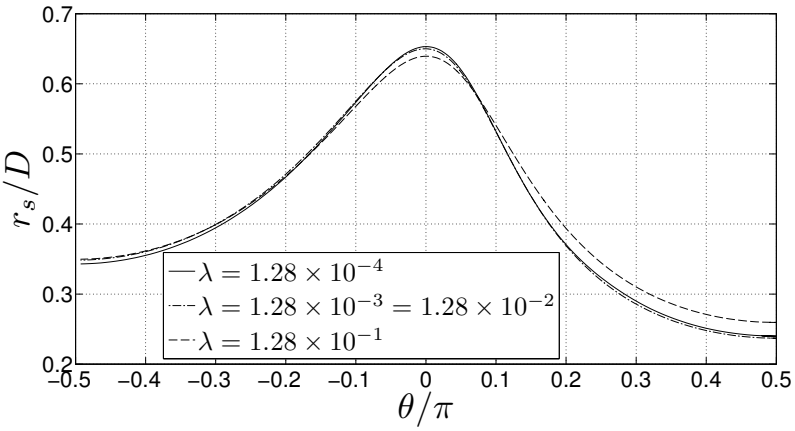

Figure 3.11: Bubble shape in terms of the distance to the interface, r_s, and the angle from the major diameter, θ, for the different values of λ herein assessed. Here $\beta = 4.21 \times 10^{-3}$, $Ga = 99.35$ and $Bo = 3.92$.

shape barely changes for $1.28 \times 10^{-4} \leq \lambda \leq 1.28 \times 10^{-2}$, the bubble becomes more spherical for $\lambda = 1.28 \times 10^{-1}$, as already mentioned above. It needs to be pointed out here that the variation of the aspect ratio, χ, can be misleading, since two bubbles with identical χ may have different shapes as it will be plotted in next Chapter 4.

Moreover, the inner gas flow field has been analyzed in order to investigate its relationship with the previous changes in U_T and shape. In this regard, Figs. 3.10(a)-(d) show the resulting streamlines (left half) and velocity contours (right half) inside the bubble for different values of λ. The streamlines clearly show the existence of a pair of counter rotating vortices caused by the continuity of the velocity and the shear stresses conditions, imposed at the bubble interface. It can be noticed that, although the core of these vortex rings barely changes with λ, their size varies due to the different momentum induced in the gas flow. This can be especially noted in the lower ring, which becomes larger as λ increases, since the gas momentum also increases, as can be also appreciated in the velocity contours plotted on the right half in Figs. 3.10(a)-(d). Nevertheless, although the change in the gas density induces important variations in the inner flow field, they do not affect the bubble shape.

Finally, as previously commented, the exact shape of the bubble has been proven to be of great importance on the rising process, since it determines the vorticity generation and, consequently, the trajectory transition from rectilinear to zig-zag path. For this reason, the outer flow, obtained from the final bubble shape, has been analyzed as well. In Fig. 3.12, a recirculation region can be observed for all λ (left half), as well as the production of azimuthal vorticity (right half), whose maximum is located at the point of maximum curvature. The effect of increasing λ is noticeable in the liquid separation point downstream the bubble, which moves inwards as the shape becomes more rounded, thus reducing the size of the standing eddy. Similarly, the generation of azimuthal vorticity also varies, being less intense for increasing values of λ, resulting therefore in a more stable bubble. Again, these effects are much more noticeable for the case of largest λ. From the above results on the bubble shape, terminal velocity, and outer flow, it is clear that the influence of the gas density on the rising dynamics is negligible for values of λ from $O(10^{-4})$ to $O(10^{-2})$ (values

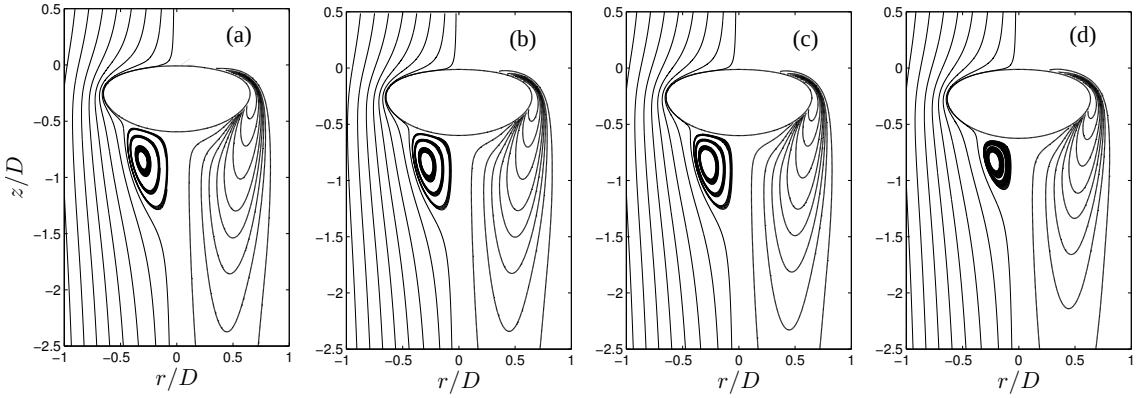

Figure 3.12: Bubble shapes, together with the streamlines (left half) and azimuthal vorticity contours (right half) outside the bubble, for different values of the density ratio (a) $\lambda = 1.28 \times 10^{-4}$, (b) $\lambda = 1.28 \times 10^{-3}$, (c) $\lambda = 1.28 \times 10^{-2}$, and (d) $\lambda = 1.28 \times 10^{-1}$, corresponding to a bubble with $\beta = 4.21 \times 10^{-3}$, $Ga = 99.35$ and $Bo = 3.92$.

corresponding to helium and sulfur hexafluoride), being only important for cases with larger λ, which would be associated to the case of rising drops. Nevertheless, the gas density is shown to have an important influence on the inner flow field.

To complete the study on the gas effect, a similar analysis has been conducted by varying the gas viscosity, achieving a range of the gas-to-liquid viscosity ratios, $\beta = \mu_g/\mu_l$, from 4.21×10^{-4} to 4.21×10^{-1} ($\lambda = 1.28 \times 10^{-3}$). Table 3.2 shows the results obtained for the terminal velocity, in terms of the Re, and the aspect ratio, as well as their differences with respect to the case of lowest β. As for λ, the same trend has been obtained for increasing β: the terminal velocity decreases, since viscous stresses increase, and the bubble becomes more spherical. In this case, differences smaller than those observed varying λ have been found, being negligible in most cases, except for the largest β, for which maximum differences of 1.34% and 4.05% were found in the terminal velocity and the bubble shape, respectively. The effect of increasing gas viscosity on the inner flow is shown in Fig. 3.13 for $Ga = 99.35$, $Bo = 3.92$ and $\lambda = 1.28 \times 10^{-3}$, in terms of the streamlines and velocity contours. Since the gas density is fixed, the buoyancy forces remain constant. Therefore, although the two counter rotating vortices are also observed, the increase of μ_g induces a very different evolution on the inner flow field. In this case, as the gas viscosity increases, the velocity gradients decrease, and the upper vortex, of higher velocity, also increases, therefore reducing the lower one to a residual location. Despite the evolution of inner flow field is different from that observed varying λ, notice that the location where both vortex rings get in contact with the interface in each case is nearly the same as those obtained increasing λ. This point, which is related to the liquid separation point, moves towards the axis as the bubble becomes more spherical. As a consequence, an outer flow field evolution quite similar to that found increasing λ is obtained, with the subsequent aforementioned effects on the properties of bubble wake, vorticity generation and stability.

Again, as in the case of gas density, the effect of the gas viscosity on the external flow (bubble

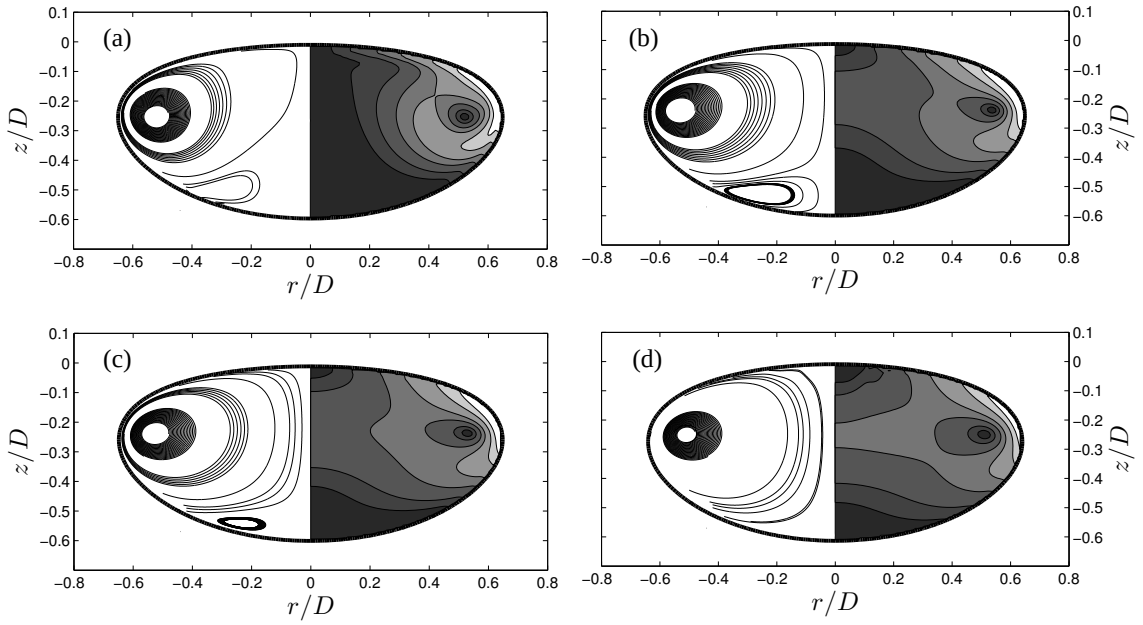

Figure 3.13: Bubble shape together with the streamlines (left half) and dimensionless relative velocity contours (right half) inside the bubbles with different viscosity ratio (a) $\beta = 4.21\times10^{-4}$, (b) $\beta = 4.21\times10^{-3}$, (c) $\beta = 4.21 \times 10^{-2}$, and (d) $\beta = 4.21 \times 10^{-1}$, with $\lambda = 1.28 \times 10^{-3}$, $Ga = 99.35$ and $Bo = 3.92$. The values of the velocity isocontours, from dark to light, are [0, 0.1, 0.2, 0.35, 0.5, 0.75, 1].

	a)	b)	c)	d)
β	4.21×10^{-4}	4.21×10^{-3}	4.21×10^{-2}	4.21×10^{-1}
Re	116.03	115.97	115.62	114.47
$E_{Re}\%$	-	0.05	0.35	1.34
χ	2.22	2.21	2.21	2.13
$E_{\chi}\%$	-	0.45	0.45	4.05

Table 3.2: Re and aspect ratio, χ, obtained for the four values of the gas-to-liquid viscosity ratio, β, for $Ga = 99.35$, $Bo = 3.92$ and $\lambda = 1.28\times10^{-3}$. E_{Re} and E_{χ} represent the relative difference with respect to Re and χ corresponding to the case of lowest β.

shape and terminal velocity) is negligible, observing small differences at values of β which correspond to cases of rising drops. However, it has been also observed that the gas viscosity has a strong influence on the flow field established inside the bubble. In fact, the dispersed-to-continuous viscosity ratio has been shown to strongly affect the mass transfer from a fluid sphere to the surrounding fluid [124], obtaining the optimum results for low viscosity ratios. Thus, the differences in the flow fields induced inside the bubble as the gas density and viscosity are varied could constitute an alternative way of controlling the convective motion inside bubbles and drops. These results can be applied to improve the mass and heat and, as a result, to reduce the energy consumption required in these kinds of processes [5, 171]. In this context, particular results on the heat and mass transfer in the case of rising bubbles can be found in some numerical studies [26, 42]. Besides the effect on the inner flow field, it has been proven that the bubble shape, its terminal velocity

and the external flow field are not affected by the inner gas, and consequently, it does not need to be considered to perform numerical simulations where the inner flow is not required, optimizing the computational cost.

3.5 Conclusions

The present chapter of the dissertation studies the bubble rising process in a stagnant liquid, mainly focused on the terminal velocity, U_T, bubble aspect ratio, χ, as well as on the proper simulation of this phenomenon. Moreover, the effect of the inner gas on the problem dynamics has been also assessed.

First, making use of previous studies, the physics of the problem has been first described in terms of the evolution of the bubble terminal velocity, U_T, as a function of its diameter, D. In this parametric plane, for a given Mo number, there is a range of diameters for which the terminal velocity increases with the bubble size. In this region, the bubble, considered stable, rises with a rectilinear path, characterized by the existence of an axisymmetric wake downstream from the bubble. For larger D, a local maximum U_T takes place, and the bubble starts to describe a zig-zag/spiral path, a pair of counter-rotating vortices appear in the wake, and the bubble becomes unstable. From the above data, a new correlation has been proposed, given by $U_T/\sqrt{gD} = (2.14\,Bo^{-1} + 0.505)^{1/2}$, to determine the bubble terminal velocity in the unstable region for a wide range of fluid properties and bubble sizes, based on the approximation by Clift *et al.* [25]. The same correlation, expressed in terms of the Re, We, and Mo numbers as $Re = [We^2\,(We - 2.14)/(0.505\,Mo)]^{1/4}$, reproduces the experimental values of Re for different Mo in the unstable region. In addition, equating this correlation with that given by Rastello *et al.* [116], valid for bubbles rising with rectilinear paths, an expression for the critical Weber number, We_c, at which the transition from a rectilinear to a zig-zag motion takes place has been also proposed, as a function of Mo, which writes $We_c^{-2/3}(We_c - 2.14) = 8.92\,Mo^{1/5}$.

Considering these particularities, two different open source solvers implementing a VOF interface-capturing technique have been assessed, specifically, InterFoam and Gerris Flow Solver. The former, included in OpenFOAM, implements the VOF technique within non-uniform, static meshes. On the other hand, Gerris implements a quad/octree AMR method for spatial discretization, and thus it allows a dynamic adaptive mesh refinement. To evaluate the suitability of both solvers, the rectilinear rise of a stable bubble with a low terminal velocity and high surface tension ($Ga = 5$ and $Bo = 0.1$), i.e. quasi-spherical shape, has been analyzed by performing two-dimensional axisymmetric simulations with meshes of different resolution. The results show that the terminal velocity obtained with Gerris does not vary regardless the grid resolution, whereas very different values are obtained from InterFoam. Moreover, the presence of parasitic currents is observed with InterFoam solver, being their intensity also a function of the grid resolution. Although these artificial velocities can be reduced increasing the spatial resolution, they do not completely disappear and the CPU time is considerably incremented. However, parasitic currents are not observed when the Gerris solver is used. Therefore, the Adaptative Mesh Refinement technique and the surface tension treatment impletented in Gerris, make this solver more suitable in the case at hand, i.e. surface tension

dominated flows. Subsequently, two-dimensional axisymmetric and three-dimensional Gerris simulations of a bubble with $Ga = 50$ and $Bo = 1$, have been compared to confirm the suitability of the first to simulate a stable bubble. A good agreement has been observed for Re and aspect ratio, χ, as well as for velocity and pressure fields, being the CPU time considerably reduced in the case of two-dimensional computations. Moreover, since this case is close to the trajectory transition, this confirms the validity of the axisymmetry assumption in this region. In addition, the results have been compared with experimental data and with the proposed correlations, obtaining a good agreement in the transition path region, and thus, validating the numerical procedure.

Finally, the validated numerical method has been employed to study in detail the effects of the gas properties on the dynamics of a bubble rising in still liquid. To this aim, the effects of both, the gas density and viscosity have been analyzed by performing simulations with different gas-to-liquid density, $\lambda = \rho_g/\rho_l$, and viscosity ratios, $\beta = \mu_g/\mu_l$, in the ranges $1.28 \times 10^{-4} \leq \lambda \leq 1.28 \times 10^{-1}$ and $4.21 \times 10^{-4} \leq \beta \leq 4.21 \times 10^{-1}$, respectively. To determine the differences on the bubble dynamics, their effect on the bubble shape and terminal velocity, as well as on the inner and outer velocity fields, have been assessed. In general, increasing values of λ and β exhibit the same features: the bubble terminal velocity decreases, it becomes more rounded, and the standing eddy formed behind the bubble becomes smaller. Nevertheless, these changes are negligible for $1.28 \times 10^{-4} \leq \lambda \leq 1.28 \times 10^{-2}$ and $4.21 \times 10^{-4} \leq \beta \leq 4.21 \times 10^{-2}$, being only significant for $\lambda \geq 1.28 \times 10^{-1}$ and $\beta \geq 1.28 \times 10^{-1}$, which would represent rising drops rather than bubbles. Therefore, the effect of the inner gas can be neglected, that is, numerical simulations can be performed without taking into account the inner gas, with the resulting reduction of the computational time, in case only the outer liquid flow and the bubble shape are needed. This conclusion has a direct impact to obtain the axisymmetric base flow, and bubble shape in hydrodynamic stability studies, for example. Nevertheless, the gas density and viscosity variations have shown a strong influence on the inner flow field, which is of special importance in mass and heat diffusion processes across the interface. Therefore, the proper selection of a transportation gas could greatly enhance the aforementioned diffusion phenomena, thus optimizing the global efficiency of these kinds of processes.

CHAPTER
FOUR

Wake instability of fixed axisymmetric bubbles

The aim of this chapter is to analyze numerically the transition from straight to zig-zag motion during the rising of a single bubble in a still liquid. Results are reported for the regime in which the inner fluid motion is negligible, i.e., in the limit of $\mu_g/\mu_l \ll 1$ and $\rho_g/\rho_l \ll 1$, where μ denotes dynamic viscosity, ρ is density and subscripts g and l correspond to the gas and liquid phase, respectively. In such a regime the flow dynamics is governed by a set of two nondimensional parameters, which are chosen as the Bond, $Bo = \rho_l\, g\, D^2/\sigma$, and the Galilei, $Ga = \rho_l\, g^{1/2}\, D^{3/2}/\mu_l$, numbers, being σ the surface tension coefficient, g the gravity acceleration and D the bubble equivalent diameter. The neutral curve for the onset of zig-zag motion corresponding with the realistic fore-and-aft axisymmetric bubble shape has been reported and discussed its relation with the critical curve for the existence of a standing eddy. By mapping the results into the $\{\chi, Re\}$-plane, where χ denotes the transverse-to-streamwise aspect ratio and $Re = \rho_l\, U_T\, D/\mu_l$ is the Reynolds number based on the terminal velocity of the bubble U_T, the results shown in this chapter demonstrate the existence of substantial differences with respect to previous theoretical works performed assuming a spheroidal (or revolution ellipsoidal) bubble for all χ and Re, and obtain a good agreement with available experimental data. The fore-and-aft asymmetry of the axisymmetric bubble is shown to be a relevant parameter affecting the strength of the azimuthal vorticity along the neutral curve, a phenomenon that has not been reported before.

This chapter is included in the paper "Wake instability of a fixed axisymmetric bubble of realistic shape", by J.C. Cano-Lozano, P. Bohorquez and C. Martínez-Bazán, published in the Int. J. Multiphase Flow [19].

4.1 Introduction

A single gas bubble rising in a still liquid may follow a rectilinear, zig-zag or spiral path depending mainly on the gravitational acceleration, the pair of fluids involved and the interfacial properties, as well as on the bubble size. This phenomenon has been analyzed experimentally in several studies and it is usually referred to as Leonardo's paradox, since Leonardo Da Vinci reported the first pioneering observations [114, 113].

A great deal of experimental work has been devoted to characterize the terminal velocity and shape of an isolated bubble, the ensuing path and the wake flow behind it. In the work of Haberman & Morton [53] the bubble diameter was progressively increased setting the remaining physical parameters constant. They found that, at a constant value of the Morton number,

$Mo = g\mu_l^4/\sigma^3\rho_l = Bo^3/Ga^4$, the final bubble shape evolves from a sphere to an ellipsoid as the equivalent diameter, D, is increased, attaining a spherical cap form at sufficiently large diameters. These shapes exhibited rectilinear, spiral and straight rocking (i.e. the bubble rotates around its streamwise axis following a straight path) motions, respectively. However, for Morton numbers larger than 10^{-3}, they observed a different phenomenology with bubbles ascending rectilinearly independently of their diameters. Later, it was discovered that the transition from rectilinear to spiral path occurs through zig-zag motion (see last paragraphs in pp 252 and 253 by Saffman [125]) with the bubble moving from side to side in a vertical plane (Lindt [77], see his Table 2, corroborated Saffman's findings). In a subsequent study, Bhaga [12] complemented Haberman and Morton's study and showed that the critical value of the Morton number that ensures a straight path ranges between 1.64×10^{-3} and 5.48×10^{-3}. He also stated that the spherical cap shape occurs for $Bo > 40$, having a rectilinear path at all Reynolds numbers, in agreement with Wegener & Parlange [174]. However, in this range of Bond numbers, the bubble wake can be very complex, exhibiting skirts in laminar regime or turbulent wakes (referred to as open wakes) for $Re > 125$, where $Re = \rho_l U_T D/\mu_l$ is the Reynolds number based on the terminal velocity of the bubble, U_T. Accurate parametric studies were later performed by Clift *et al.* [25] and Bhaga & Weber [13] to characterize the bubble shape and motion (see Magnaudet & Eames [83], for a comprehensive review).

Apart from the previously mentioned experimental works, additional studies focusing on the loss of rectilinear motion and the wake flow behind a zig-zagging bubble were performed in tap water by Hartunian & Sears [55] and Aybers & Tapucu [8] (see Table 7.1 in Clift *et al.* [25]), in several liquids for a wide range of Morton numbers ($2.39 \times 10^{-11} \leq Mo \leq 5.85 \times 10^{-7}$) by Tsuge & Hibino[163], and using pure clean water by Duineveld [34], who highlighted the fore-and-aft asymmetry that unstable bubbles can exhibit. Visualizations and measurements of the wake flow of an unstable bubble have been done using dye [81, 128], particle image velocimetry [18, 183], laser doppler anemometry [36], the thermographic Schlieren setup [29, 170] and planar laser-induced fluorescence [142]. The exact path followed by the bubble has been also measured by Wu & Gharib [175], Shew *et al.* [140] and Zenit and Magnaudet [182] using image processing. However, as pointed out by de Vries *et al.* [30], experimental methods are usually intrusive and introduce impurities that may affect strongly the instability development. Also, the use of pure clean liquids is necessary, as happens for pure versus tap water [18]. Additional difficulties appear associated with compressibility of gas phase that causes variations of bubble volume and equivalent diameter during experiments [103, 140], viscosity changes due to temperature gradients [29, 170] and the presence of surfactants [146] that modify the terminal velocity and shape of the bubble [157]. Considering these difficulties it has been decided that the problem must be considered from the numerical side, allowing to study the ideal scenario.

The primary origin of the zig-zag and spiral trajectory of a rising bubble is a double threaded wake that develops behind the bubble, analogous to the case of solid static bluff bodies [97, 98, 139]. The main difference with respect to no-slip solid bodies is the zero-shear-stress boundary condition acting on the bubble surface, though it does not modify the unstable global mode [37]. As a consequence two approaches have been adopted to theoretically predict the onset of zig-zag motion. Given a terminal velocity and bubble shape, one can anticipate the loss of the flow axisymmetry,

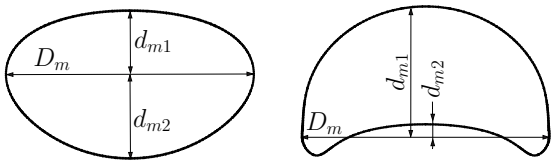

Figure 4.1: Sketch showing the minor, $d_m = d_{m1} + d_{m2}$, and major, D_m, bubble diameters for a convex shape viewed from inside (left, $Ga = 200$ and $Bo = 0.82$) and concave interface at the bottom (right, $Ga = 20$ and $Bo = 100$). The bubble aspect ratio is defined as $\chi = D_m/d_m \geq 1$. Notice that pure spheroids have $d_{m1} = d_{m2}$ though, in the present work, this constraint has been relaxed as $0.98 \leq d_{m1}/d_{m2} \leq 1.02$. Also, spherical bubbles are gived by $\chi \leq 1.02$. Bubbles move upwards.

the development of a pair of counter-rotating vortices in the wake flow behind the bubble and a non-straight path by hydrodynamic linear stability analysis [179] or by three-dimensional Direct Numerical Simulations (DNS) [84]. In these studies the bubble was assumed to have a fixed spheroidal shape and the results were parametrized in terms of the bubble aspect ratio, defined here as $\chi = D_m/d_m$ where D_m is the major, transverse axis of the bubble and $d_m = d_{m1} + d_{m2}$ is its minor, streamwise counterpart (see Fig. 4.1). Notice that d_{m1} and d_{m2} represent the distance from the plane perpendicular to the axis containing the major diameter to the front and the back of the bubble respectively. Thus, d_{m2} will be positive (negative) if the back of the bubble is below (above) the plane of D_m. However, as shown in Fig. 4.1, the true bubble shape may be rather different from a spheroid. So the main novelty of this study, that has not been considered before, is that the shape of the bubble is not prescribed, but it is obtained as a function of the dimensionless parameters involved in the problem. Alternatively, three-dimensional numerical simulations were presented by Gaudlitz & Adams [46] and Tuković & Jasak [165] who solved the motion in the gas and liquid phases with hybrid particle Level-Set and interface tracking methods, respectively. The main advantage of these techniques are that the real shape of the bubble is obtained during the numerical simulation but they are computationally very expensive in comparison with DNS of the liquid phase and linear stability analysis.

To the best of the authors' knowledge there are no theoretical studies providing the neutral curve for the onset of zig-zag instability considering the real shape of the bubble in terms of the dimensionless parameters governing the flow dynamics. Therefore, the main purpose of this chapter is to provide new results on the critical curve of zig-zag instability using the real bubble shape. To this end, the limit of $\mu_g/\mu_l \ll 1$ and $\rho_g/\rho_l \ll 1$, where the gas inner motion can be neglected, will be studied. The real bubble shape and terminal velocity is obtained herein by means of axisymmetric numerical simulations where the bubble is allowed to freely rise, and the stability of the axisymmetric liquid flow is checked with unsteady, three-dimensional incompressible numerical simulations of the flow around a bubble kept fixed, of shape provided by the axisymmetric simulations. This chapter is organized as follows: in Section 4.2 the numerical methodology is explained in detail; next, results on the bubble shape and terminal velocity are outlined in Section 4.3.1; the existence of standing eddy and its relation with the zig-zag instability is discussed in Section 4.3.2; finally, stability results from the three-dimensional numerical simulations are drawn in Section 4.3.3. The conclusions are summarized in Section 4.4.

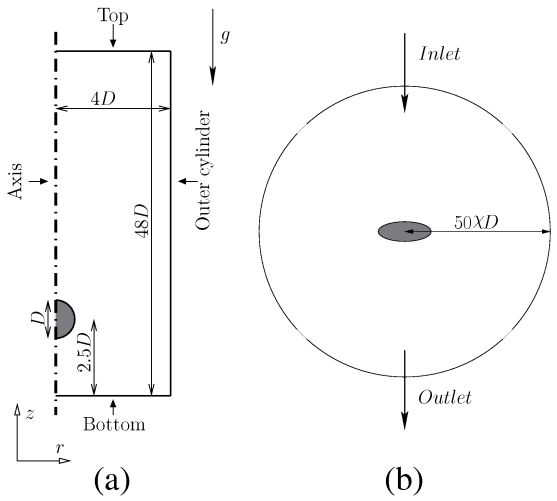

Figure 4.2: Sketch of the computational domain and boundary conditions in the (a) axisymmetric and (b) three-dimensional numerical simulations.

4.2 Numerical methodology

Axisymmetric numerical computations were performed by using Gerris Flow Solver, an open source code available in the public domain that allows the accurate simulation of surface-tension-dominated interfacial fluid flows [111]. The computational domain employed in the axisymmetric numerical simulation emulated a vertical cylinder with characteristic streamwise length and radius of $48D$ and $4D$, respectively, as sketched in Fig. 4.2a. Several test cases were run using different domain sizes to ensure that the dimensions of the computational domain chosen were adequate. This domain was discretized with a coarse background mesh containing 64 and 768 cell edges along the vertical (z) and radial (r) directions, respectively. Also, a very fine mesh, moving with the bubble, was used inside the bubble and in its vicinity. This mesh extended $1D$ ahead of the bubble, $3D$ behind it to accurately capture the wake flow and $3/2$ D in the radial direction, containing 512 and 192 longitudinal and transversal cells respectively. The transition from the coarse to the fine mesh was done by means of a block structured AMR (Automatic Mesh Refinement) method that introduced additional cells in the overlapping boundaries. In fact, Gerris uses a quad/octree adaptive mesh refining technique, which allows to refine the cells size and the number of cells as a function of the refinement level selected (a refinement level divides a cell in exactly four children cells in the axisymmetric simulations), increasing the number of cells around the bubble interface. Table 4.1 shows the Reynolds number and the aspect ratio obtained using three different refinement levels for the experimental case denoted as DMS-T05 (S) in Table 4.4. Notice that, increasing the refinement level from level 2 to level 3 provides relative differences in the Reynolds number and the aspect ratio of 0.41% and 3.36 % respectively. However, if the grid size is further refined using an additional refinement level, the relative errors are reduced to 0.13% in the Reynolds number and 0.99% in χ. Thus, it has been decided to use the refinement level 4 to obtain more accurate results, assuming a higher computational cost.

Refinement	Re	$E_{Re}\%$	χ	$E_{\chi}\%$
Level 4	103.15	$--$	1.99	$--$
Level 3	103.29	0.13	2.01	0.99
Level 2	103.72	0.41	2.08	3.36

Table 4.1: Grid sensitivity analysis.

The fine mesh provided accurate resolution along the interface separating the inner (gas) and outer (liquid) fluids. To start the simulations, the same set of initial conditions as in Ohta *et al.* [104] was considered, ensuring that the steady state shape and terminal velocity U_T of the bubble reported in Section 4.3 are not affected by them. Thus, a spherical bubble initially at rest was located $2.5D$ above the bottom of the vertical cylinder and the pressure distribution was set hydrostatic. As boundary conditions, to emulate the solid bottom wall of a liquid pool, a no-slip condition at the bottom was imposed, computing the pressure from the continuity constraint, a stress-free impermeable-wall condition at the outer cylinder, zero normal velocity gradient and fixed pressure at the top, and axisymmetric conditions on the axis of the cylinder. During each numerical simulation, the temporal evolution of the bubble shape, terminal velocity and recirculation area (if existed) were checked, stopping the simulation when the steady state was reached.

Taking into account that the average number of cells was about 1.6×10^5, that transient numerical simulations were performed until a steady state was achieved, and that the pressure equation (a Poisson-like equation) was iterated up to reducing its residual below 10^{-6}, parallel computations were required to map the wide range of parameters of $5 \leq Ga \leq 300$ and $0.1 \leq Bo \leq 100$. Thus, each numerical simulation was run in two Intel Nehalem x5670 six-core processors with overall runtime of two weeks per case. A total amount of 70 simulations for $Bo = \{0.1, 0.2, 0.5, 1, 2, 5, 10, 20, 50, 100\}$ and $Ga = \{5, 10, 20, 50, 100, 200, 300\}$ were carried out. The steady state bubble shapes described in Section 4.3 are shown in Fig. 4.3. It is worth mentioning that the spatial resolution and the extent of the computational domain in the current simulations are finer and longer, respectively, than those employed in previous numerical studies (e.g. [61]). In the case of a spherical bubble, i.e. at low Bond and Galilei numbers, there were 128 cells uniformly distributed along the bubble diameter (i.e. nearly 12900 cells inside the bubble), whilst in the worst case, i.e. at $Bo = 100$ and $Ga = 200$, the number of cells in the streamwise axis (and its perpendicular) inside the bubble was about 40 (and 200).

After performing the axisymmetric numerical simulations, the bubble shape and the terminal velocity (or Reynolds number Re) obtained were used to perform three-dimensional, incompressible numerical simulations of the flow around the bubble by means of OpenFOAM. To this end, the axisymmetric bubble interface was employed to construct its corresponding three-dimensional surface that was then discretized using 52000 rectangular cells. The three-dimensional bubble was kept fixed at the center of a spherical domain of radius $50\,\chi\,D$ (see Fig. 4.2b) and the bubble surface mesh was extruded along the radial direction increasing progressively the step size until reaching the outer spherical domain. The computational domain was larger than that used by Magnaudet & Mougin[84] and it was similar to that employed by Bohorquez *et al.* [15] whose length extended 50 diameters downstream from the base of the body. In addition, the number of cells was established

according to the grid refinement study performed in Sanmiguel-Rojas *et al.* [131]. Thus, the mesh size close to the bubble surface was thin enough to accurately resolve the slip boundary layer. The radial direction was discretized into 125 intervals and a three-dimensional mesh of nearly 6×10^6 cells was constructed. The procedure described in [84] was followed to check whether the flow was stable or unstable. Alternatively, global linear stability analysis could have been done to determine the stability characteristics of the base flow, as done by Yang & Prosperetti [179], but such task lies out of the scope of this work. In the three-dimensional numerical simulations the velocity was set to the constant value of the axisymmetric terminal velocity, $\vec{v} = -U_T\,\vec{e}_z$, and the pressure was computed from the incompressible constraint at the inlet of the outer domain (see Fig. 4.2b) whilst at the outlet it is fixed $p = \vec{n}\cdot\nabla\vec{v} = 0$, where $\vec{n}$ is the normal surface vector pointing outwards from the computational domain [15]. Zero normal flux and zero-shear-stress (or shear free) boundary conditions were established at the bubble surface [84].

The main novelty of the study presented in this chapter is that we the real bubble shape, computed numerically for each Galilei and Bond number, was used instead of assuming a spheroidal bubble. As a matter of fact, it shall show in Section 4.3 that such hypothesis is valid only for a very limited set of values. Also, taking into account the global nature of the linear instability responsible for the onset of zig-zag motion [179], it is easy to understand that varying the bubble shape, or not considering the true base flow, may have a strong impact on the stability results [156].

4.3 Results

The main results on this study are associated with the key point that the axisymmetric bubble shape corresponding to each pair of *Ga* and *Bo* numbers is computed and not prescribed. Therefore, some geometrical properties of the computed shapes are summerized and relating them to known results, in Section 4.3.1. Next, in Section 4.3.2, the presence of a standing eddy in the wake of the bubble has been investigated in order to determine its connection with the loss of rectilinear path. Finally, the three-dimensional numerical simulations are presented in Section 4.3.3, allowing to revisit the theoretical predictions of the neutral curve for the onset of a zig-zag motion, and showing the high sensitivity of the stability results to the axisymmetric bubble shape.

4.3.1 Axisymmetric bubble shape and terminal velocity

Following previous works analyzing spheroidal bubbles (e.g. Blanco & Magnaudet [14]), the aspect parameter χ is defined as the ratio between the major bubble diameter in the transversal direction, D_m, and the bubble length measured along the streamwise axis, d_m, (see Fig. 4.1). The shape of the bubbles obtained from the axisymmetric numerical simulations are represented in Fig. 4.3, together with the values of the aspect ratio, as function of the Galilei and the Bond numbers. In addition, Table 4.2 shows the values of the dimensionless curvature at the front and back of the bubbles. In this table, positive values indicate that the shape of the bubble is convex viewed from inside, while negative values indicate that the shape is concave. The curvature has been made dimensionless with the diameter of the bubble initially at rest, D, providing a dimensionless

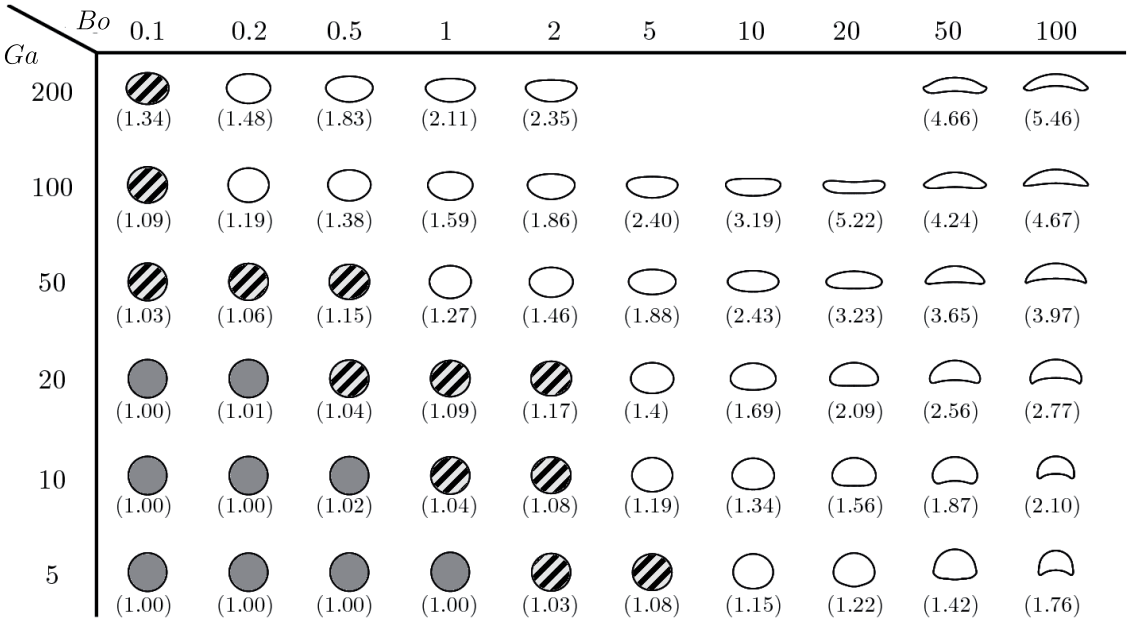

Figure 4.3: Axisymmetric bubble shapes and aspect ratio values χ obtained with Gerris Flow Solver. Gray and striped bubbles correspond to spherical and spheroidal bubbles respectively.

curvature equal to 1 for a spherical bubble. At low Galilei and Bond numbers, as revealed by the gray shapes in Fig. 4.3, bubbles are nearly *spherical* since $\chi \approx 1$, in particular $\chi \leq 1.02$. The threshold chosen to model bubbles as spheres is more conservative than the value $\chi \leq 1.1$ employed in previous works (see Section III.B in Clift *et al.* [25]). This part of the $\{Ga, Bo\}$ plane is separated from that having bubbles with only one vertical axis of revolution (colored in white) by a region depicted with striped bubbles (hereafter referred to as *revolution ellipsoidal* or *spheroidal* bubbles). To distinguish if the shape is spheroidal, a ratio between the vertical semi-axes of $0.98 < d_{m1}/d_{m2} < 1.02$ (see Fig. 4.1) has been employed as criterion. Notice that, in the range of Re and Bo investigated here, there is a relatively small number of bubbles having spherical and spheroidal shapes, which have been displayed in Fig. 4.3 as gray and striped bubbles respectively. Outside this region, bubbles are neither spherical nor spheroidal, and the shape varies significantly with Bo and Ga. In general, χ increases monotonically with Ga and Bo, and the bubble shape deviates more and more from spheroidal. At this point, it is important to remark the difference in terminology established here, with respect to classical sources, when using the term ellipsoidal with $\chi > 1.1$. Quoting p. 23 in Clift *et al.* [25] : "*The term ellipsoidal is generally used to refer to bubbles and drops which are oblate with convex interface (viewed from inside) around the entire surface... It must be noted that actual shapes may differ considerably from true ellipsoids and that fore-and-aft symmetry must not be assumed*".

The axisymmetric numerical results are in excellent agreement with those by Ryskin & Leal [123], Ohta *et al.* [104], Hua & Lou [61], Feng [40] and Agarwal *et al.* [1] at almost all values of Ga and Bo. The only differences found with respect to the exhaustive numerical study by Hua & Lou [61] appeared at $Ga = 200$ and $2 < Bo < 50$, where axisymmetric shape oscillations were observed in the numerical simulations. However, the results presented in this chapter agree with

Ga \ Bo	0.1	0.2	0.5	1	2	5	10	20	50	100
200	0.62	0.54	0.36	0.23	0.13				0.29	0.30
	0.72	0.69	0.57	0.53	0.48				−0.20	−0.29
100	0.86	0.76	0.6	0.46	0.33	0.16	0.03	−0.27	0.39	0.40
	0.94	0.84	0.74	0.65	0.55	0.38	0.17	−0.01	−0.16	−0.17
50	0.95	0.91	0.80	0.69	0.56	0.40	0.31	0.31	0.46	0.47
	0.96	0.94	0.86	0.77	0.65	0.43	0.21	0.11	−0.13	−0.16
20	0.99	0.98	0.95	0.89	0.81	0.68	0.62	0.59	0.60	0.58
	0.99	0.98	0.94	0.89	0.8	0.55	0.27	−0.05	−0.21	−0.21
10	0.99	0.99	0.97	0.95	0.92	0.84	0.79	0.77	0.74	0.71
	0.99	0.99	0.97	0.95	0.89	0.71	0.41	−0.02	−0.39	−0.33
5	1.00	1.00	1.00	1.00	0.96	0.92	0.88	0.93	0.865	0.83
	1.00	1.00	1.00	1.00	0.95	0.86	0.66	1.21	0.55	−0.42

Table 4.2: Curvatures at the front (upper line of each case) and the back (lower line of each case) of the bubble as function of Ga and Bo. These values have been made dimensionless with the diameter of the bubble initially at rest, D, providing a dimensionless curvature equal to 1 for a spherical bubble.

Ryskin and Leal [123], who argued the absence of steady axisymmetric solution, as well as with experiments [125, 25]. These unstable axisymmetric bubbles are usually called *wobbling* bubbles, see for instance Fig. 8 in Bhaga & Weber [13]. In addition, at $Ga = 100$ and $10 \leq Bo \leq 20$, observing *disk-like* bubbles [40] having a concave interface at the top (view from inside) prior to acquiring a *spherical-cap* shape for $Bo \gtrsim 50$. Whilst this fact seems unphysical a priori, similar results were reported by [123, 104, 40, 1]. Nevertheless, it is difficult to verify this behavior experimentally since a camera is unable to capture the inner details of three-dimensional concave shapes. For the same Galilei number and higher Bond numbers, the disk-like family of shapes were no longer observed and spherical-cap bubbles were formed. To the best of our knowledge, the recovery of a spherical-cap shape at $Bo \geq 50$ and $Ga \geq 100$ has not been described before, since most authors did not report results in this range of parameters, see e.g. Fig. 2 in Ryskin & Leal [123]. Moreover, an additional set of simulations have been run at $Ga = 300$ and different behaviors have been found depending on the Bond number: axisymmetric shape oscillations, caused by surface tension effects, were observed for $Bo < 0.5$ [92, 81] and wobbling bubbles were formed when $Bo \geq 1$, obtaining steady shapes only at $Bo = 0.5$. However, since at $Ga = 300$, only bubbles in the range $0.5 \leq Bo < 1$ achieved a steady shape, this case has not been included in Fig. 4.3.

The results on the aspect ratio χ, showing several isolines in the plane $\{Bo, Ga\}$, and highlighting the regions where spherical (light gray) and spheroidal (dashed area) bubbles exist, are summarized in the Fig. 4.4. With the aim of illustrating the three families of shapes appearing in axisymmetric bubbles, four points denoted by A, B, C and D with $\{Bo, Ga\}$ values of $\{0.2, 10\}$, $\{1, 20\}$, $\{1, 100\}$ and $\{20, 10\}$, respectively, are shown. The corresponding bubble shapes can be found in Fig. 4.3 as well as in the inset of Fig. 4.4. When $\chi \approx 1$, see for instance bubble A, the shape is spherical, while spheroidal (or revolution ellipsoidal) geometries occur at about $\chi \approx 1.02$, according to the shape criterion defined in this chapter. The loss of spheroidal shape appears for larger values of χ depending both on Ga and Bo and was established based on the fore-and-

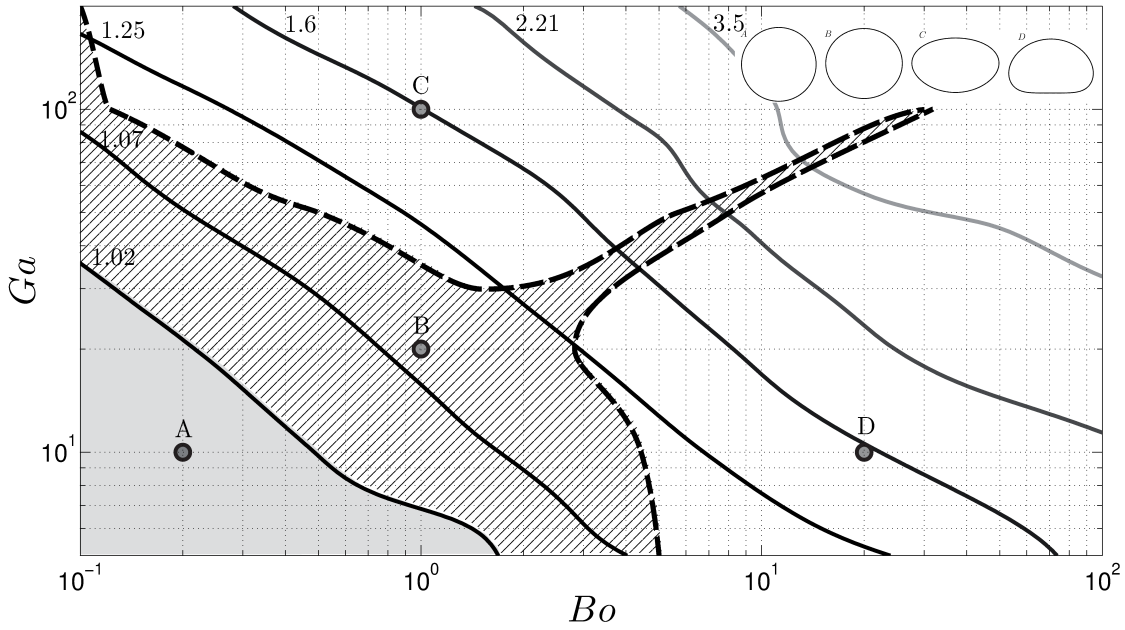

Figure 4.4: Isocontours of the aspect ratio (χ = 1.02, 1.07, 1.25, 1.60, 2.21, 3.50) in the $\{Ga, Bo\}$ parameter space. Bubbles in gray and dashed areas are spherical ($\chi \leq 1.02$) and spheroidal ($0.98 \leq d_{m1}/d_{m2} \leq 1.02$), respectively, as for Fig. 4.3. Cases A, B, C and D correspond to $\{Bo, Ga\}$ values of $\{0.2, 10\}$, $\{1, 20\}$, $\{1, 100\}$ and $\{20, 10\}$, respectively, and their shapes are shown in the inset.

aft asymmetry threshold given by $0.98 \leq d_{m1}/d_{m2} \leq 1.02$. The curve determining the loss of the spheroidal shape is depicted in Fig. 4.4 with a thick-dashed line. The spiky nose extending into the white region arises due to the shape changes previously described at $Ga > 20$. For instance, Fig. 4.3 shows that, at $Ga = 100$, bubbles have a flatter front and a more rounded rear for $Bo \approx 5 - 10$ corresponding to a fore-and-aft asymmetry of $d_{m1}/d_{m2} < 0.98$. Conversely, as the Bond number increases, spherical cap bubbles are found with asymmetries of $d_{m1}/d_{m2} > 1.02$. This progressive change in the fore-and-aft asymmetry from values lower than 0.98 to larger than 1.02 occurs through a narrow range of Bond numbers, as shown in Fig. 4.4. Next, the non-spheroidal shapes occurring in the region colored in white can be observed, for instance in the case of $\chi = 1.6$, i.e. points C and D. It is worth noticing that the bubble shape varies with Ga and Bo, for a fixed value of the aspect ratio. Consequently, a constant value of χ does not correspond to a unique axisymmetric shape.

An additional parameter required to discuss the stability characteristics of the bubble motion is the terminal velocity, U_T. Table 4.3 shows the ratio between the Reynolds and the Galilei numbers, i.e. $Re/Ga = U_T/\sqrt{gD}$, commonly referred to as Froude number. It also allows to map the set of non-dimensional numbers $\{Bo, Ga\}$ to alternative parameter planes formed by pairs of independent dimensionless numbers, including the Weber number $We = \rho U_T^2 D/\sigma = Bo\ (Re/Ga)^2$, or the capillary number, $Ca = \mu U_T/\sigma = Bo\, Re/Ga^2$. Alternatively, the Morton number $Mo = g\,\mu^4/(\rho\,\sigma^3) = Bo^3/Ga^4$ can also be used. The computations of the terminal velocity were validated by comparing additional numerical simulations with previously published experimental results. Several results are summarized in Table 4.4 for water, DMS-T11 and DMS-T05 liquids [182, 183], as well as for an

$Ga\backslash Bo$	0.1	0.2	0.5	1	2	5	10	20	50	100
200	4.21	3.17	2.51	1.97	1.51				0.68	0.72
100	2.64	2.51	2.03	1.74	1.42	1.09	0.92	0.74	0.72	0.74
50	1.71	1.69	1.55	1.41	1.22	0.99	0.83	0.72	0.67	0.66
20	0.97	0.96	0.91	0.89	0.86	0.77	0.69	0.62	0.59	0.58
10	0.63	0.62	0.60	0.59	0.57	0.55	0.52	0.49	0.47	0.45
5	0.37	0.37	0.37	0.37	0.36	0.35	0.33	0.29	0.29	0.29

Table 4.3: Ratio between the terminal, U_T, and the characteristic velocity, $\sqrt{gD}$, or, similarly, between Re and Ga, as a function of Bo and Ga.

air bubble ascending rectilinearly in water (see p. 110 in [170]). The table shows that the relative errors between the computations made in this chapter and the experimental Reynolds numbers and aspect ratios are always lower than 5 %, validating the numerical computations for the mesh size, resolution and numerical schemes described in Section 4.2.

	Ga	Bo	Re_{exp}	Re	$E_{Re}\%$	χ_{exp}	χ	$E_{\chi}\%$
Water	239.19	0.44	650	648.90	0.17	2.00	1.93	3.50
DMS-T11	71.35	6.34	70	69.78	0.31	2.35	2.32	1.15
DMS-T05 (O)	99.35	3.92	113	112.63	0.40	2.16	2.21	2.43
DMS-T05 (S)	85.45	3.21	100	103.15	3.15	1.98	1.99	0.50
VLDS (S)	174.14	0.23	546	568.00	4.00	1.40	1.47	5.00

Table 4.4: Comparison between our numerical simulations and experiments: water and DMS-T11 data are taken from [182], DMS-T05 data is from [183] and VLDS (S) corresponds to an air bubble ascending rectilinearly in water (see p. 110 in [170]). E_{Re} and E_{χ} denote the percent relative error between experiments (subscript *exp*) and numerics for the Reynolds number Re and aspect ratio χ, respectively. Finally, letter O (S) in liquid DMS-T05 denotes an oscillatory (stable) bubble ascending in zig-zag (rectilinear) path.

So far it has been observed that using χ as the only parameter to characterize real bubbles does not necessarily prescribe their actual shape. For this reason, it has been decided to keep the original set of dimensionless numbers, namely Bo and Ga, to parameterize the study, since their values fix both the bubble shape (see Fig. 4.3), and its terminal velocity (see Table 4.3). This is one of the key points of this work and highlights the differences with respect to previous studies supposing a fixed spheroidal shape of the bubble for all Ga. Also, it is important to point out that the spheroidal shape assumption is only valid in a small part of the $\{Bo, Ga\}$ plane, so that previous results reported under such a hypothesis might not be applicable in the white region of Fig. 4.4.

4.3.2 Critical curve for the existence of a standing eddy

Additional numerical simulations were performed with the aim to accurately determining the critical curve for the existence of a standing eddy behind the bubble. This problem was first solved,

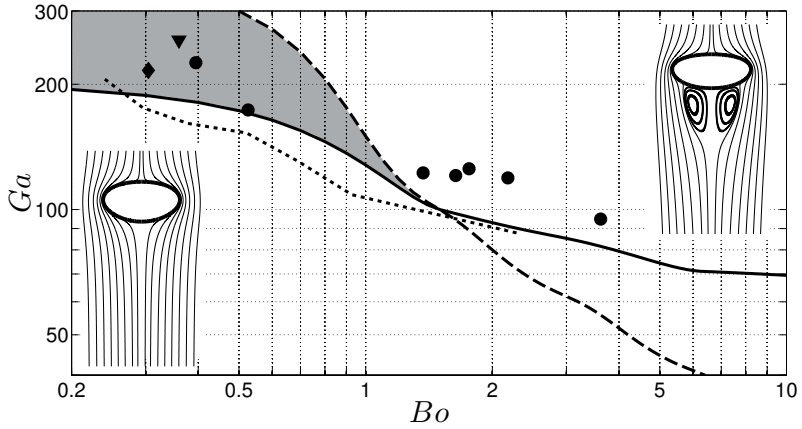

Figure 4.5: Dashed line: transition curve for the presence of standing eddy obtained from our axisymmetric simulation; Continuous line: transition curve for the onset to zig-zagging motion given by our three-dimensional numerical simulations; Solid circles (●): experimental results indicating the onset of zig-zag motion by Tsuge & Hibino [163]; Inverted triangle (▼): experimental unstable point reported by de Vries [29]; Diamond (⧫): experimental unstable point reported by Veldhuis [170]; Dotted line: transition curve given by the values of Ga and Bo associated to the bubble diameter having the maximum velocity of rise for different Morton numbers taken from Fig. 4 in Maxworthy *et al.* [88], since this curve can be considered as a lower bound for the neutral zig-zagging curve.

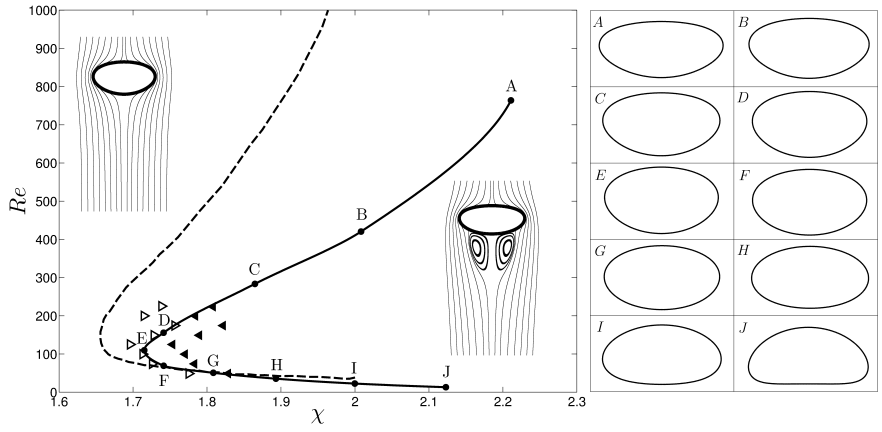

	A	B	C	D	E	F	G	H	I	J
Ga	300	200	150	100	80	60	50	40	30	21
Bo	0.5	0.82	1.0	1.4	2.0	3.1	4.3	6.50	10.4	20.2
Re	763.77	420.50	283.46	155.63	109.65	69.09	50.75	35.33	22.51	13.09
χ	2.21	2.00	1.86	1.74	1.71	1.74	1.81	1.89	2.00	2.12
d_{m1}/d_{m2}	0.81	0.80	0.81	0.85	0.81	0.83	0.91	1.00	1.29	2.22

Figure 4.6: Critical curve for the presence of standing eddy drawn in the plane $\{\chi, Re\}$. Solid line: present numerical results; dashed line: results reported by Blanco & Magnaudet [14] assuming spheroidal bubble shapes. Hollow and solid triangles represent numerical results of bubbles without and with recirculation area reported by Sanada *et al.* [129]. The table provides further details of bubbles A-J.

fixing the shape of the bubble as spheroidal, in the seminal work by Ryskin & Leal [123], and afterwards, for a wide range of Reynolds numbers of $Re \leq 1000$, by Blanco & Magnaudet [14]. Later, Sanada *et al.* [129] revisited their results by using the true bubble shape in the narrower range of $50 \leq Re \leq 225$. Here, the study by Sanada *et al.* [129] has been extended up to $13 \leq Re \leq 764$ (i.e. $21 \leq Ga \leq 300$) finding novel results in relation to Leonardo's paradox. The dashed line in Fig. 4.5 shows the transition curve for the onset of a standing eddy behind the bubble obtained from the numerical simulations carried out in this work. Below this curve, there is no recirculating flow in the wake of the bubble, whilst above it the presence of a standing eddy was found. Thus, in the range of values studied here, the plane $\{Bo, Ga\}$ is divided in two regions, one without standing eddy (on the left-hand side of the dashed curve) and another one with it (on the right-hand side). In addition, a solid line is included to show the transition curve for the onset of a zig-zagging motion obtained numerically from the three-dimensional simulations, and several experimental results corresponding to unstable bubbles ascending in zig-zag motion [163, 29, 170]. As commented above, it is difficult to reproduce experimentally the idealized theoretical scenario, due to the presence of surfactants in the liquid phase, or gas expansion due to the falling hydrostatic pressure, among other factors affecting the instability threshold (see e.g. Section IV in Brücker [18]). The experimental points of Veldhuis [170] and de Vries [29], displayed respectively with a filled diamond and a solid inverted triangle in Fig. 4.5, as well as several cases taken from Tsuge & Hibino [163] (filled circles) lie in the region corresponding to bubbles without a standing eddy. Interestingly, unstable bubbles are found in the absence of a standing eddy (shaded region in Fig. 4.5), concluding that its presence is not a necessary condition for the onset of zig-zag motion. Such a result, first postulated in p. 55 by de Vries [29], is reproduced here and constitutes a novelty with respect to the cases of solid spheres, spheroids or disks [37]. The no slip boundary condition on axisymmetric bluff bodies induces the boundary layer separation and the formation of a standing eddy behind them at low Reynolds numbers. At larger Reynolds numbers a pair of counter-rotating vortices usually develop due to the unstable nature of the background flow owing to the rupture of the recirculation area [154]. However, in the flow behind a clean bubble, there are situations at moderate Galilei numbers that do not present a recirculation region and whose outer flow is unstable, as highlighted by the shaded area in Fig. 4.5. As we shall see in more detail in Section 4.3.3, this is a noticeable result that can be justified qualitatively taking into account the real bubble shape and the vorticity field around it, and quantitatively by means of three-dimensional numerical simulations. Fig. 4.5 also includes a curve given by the values of the Galilei and Bond numbers corresponding to the maximum ascending velocity of bubbles for different Morton numbers extracted from Fig. 4 in Maxworthy *et al.* [88], since this curve can be considered as a lower bound for the onset of a zig-zag motion.

In order to compare the critical curve for the presence of recirculation with previous numerical results [14, 129], it has been plotted in the $\{\chi, Re\}$ plane in Fig. 4.6. Note the excellent agreement between the computations (solid line) and the numerical study by Sanada *et al.* [129] (hollow right triangles and solid left triangles). As a matter of fact their bubbles with standing eddy lie on the right hand side of the critical curve that covers a wider range of aspect ratios, up to $\chi = 2.21$, and extends from $Re = 13$ to $Re = 764$. However, some discrepancies have been observed with the results obtained by Blanco & Magnaudet [14] assuming fore-and-aft symmetry, simply because the bubble shapes diverge from true spheroids for $\chi > 1.34$ in most of the $\{Bo, Ga\}$-plane, as shown

in Fig. 4.3 and 4.4. Nevertheless, the differences between the results obtained in this chapter and those of Blanco & Magnaudet [14] are negligible for $Re < 69$.However, for $Re > 69$ results obtained assuming spheroidal shapes diverge from those employing the real bubble shape, and the discrepancies increase with the Reynolds number. These differences are caused by the increase of the fore-and-aft asymmetry along the $F \rightarrow A$ line, as shown in Fig. 4.6.

4.3.3 Neutral curve for the onset of zig-zag motion

As commented in Section 4.2, direct numerical simulations were carried out to determine the stability characteristics of the flow around a bubble. To this end, the real shape and the true terminal velocity obtained from the axisymmetric simulations were used to perform the three-dimensional, incompressible numerical simulations. The unstable character of the axisymmetric base flow can be associated with the development of a pair of counter-rotating vortices, as discussed by Mougin & Magnaudet [98], Magnaudet & Mougin [84] and Yang & Prosperetti [179]. Consequently, the onset of zig-zag motion occurs when the flow loses the axisymmetry as a consequence of the development of a pair of counter-rotating streamwise vortices. This criterion has been adopted hereafter to establish the stable or unstable nature of the axisymmetric base flow. Some of the stability results from the numerical computations performed in this chapter have been already represented in Fig. 4.5. In addition, to compare with previous studies, the critical curve for the loss of flow axisymmetry and the onset of zig-zag motion has been drawn in the plane $\{\chi, Re\}$ in Fig. 4.7.

Let me start by describing the case of a sphere, corresponding to $\chi = 1$. For this particular case, Moore [94] showed that, at high Reynolds numbers, the flow around a spherical bubble approaches the irrotational solution. In a subsequent paper, he obtained a refined solution for $Re \gg 1$ and $(Re)^{5/3}Mo^{1/3} \ll 1$ incorporating slight corrections to his first study, that included the consideration of spheroidal shapes (see [95]), and suggested the absence of a standing eddy behind a steadily rising bubble. This result differs significantly from that of a solid sphere with no-slip boundary condition. Atefia *et al.* [6] studied the effect of increasing the surface shear-stress and found that a standing eddy appeared at the rear of the sphere as the tangential shear stress increased. They also found that the solution differs from the potential flow at moderate Reynolds number. This phenomenon is related to the presence of surfactants in experiments, that are known to induce a partial-slip boundary condition at the bubble interface. Consequently, the presence of surfactants or impure liquids may induce the development of a recirculation region, as well as the destabilization of the axisymmetric solution and the onset of zig-zag motion [27, 18], as happens also in the case of two-dimensional wakes behind a cylinder [75]. Indeed, the axisymmetric base flow around a solid sphere exhibits a standing eddy for Reynolds numbers larger than 10 [101] and the critical Reynolds number for the development of counter-rotating vortices is of 210 [48]. Thus, in the flow around non-slip spheres, the instability occurs in the presence of a standing eddy with boundary layer separation.

However, de Vries [29] stated (see p. 55 in his PhD) that "*path instability for bubbles in pure water occurs in a regime in which a standing eddy is not observed behind a bubble*". Furthermore, a closer inspection at the rear of an air bubble ascending in pure water by de Vries [30] showed that double-threads were present whenever the curvature of its path was non-zero. In fact, according

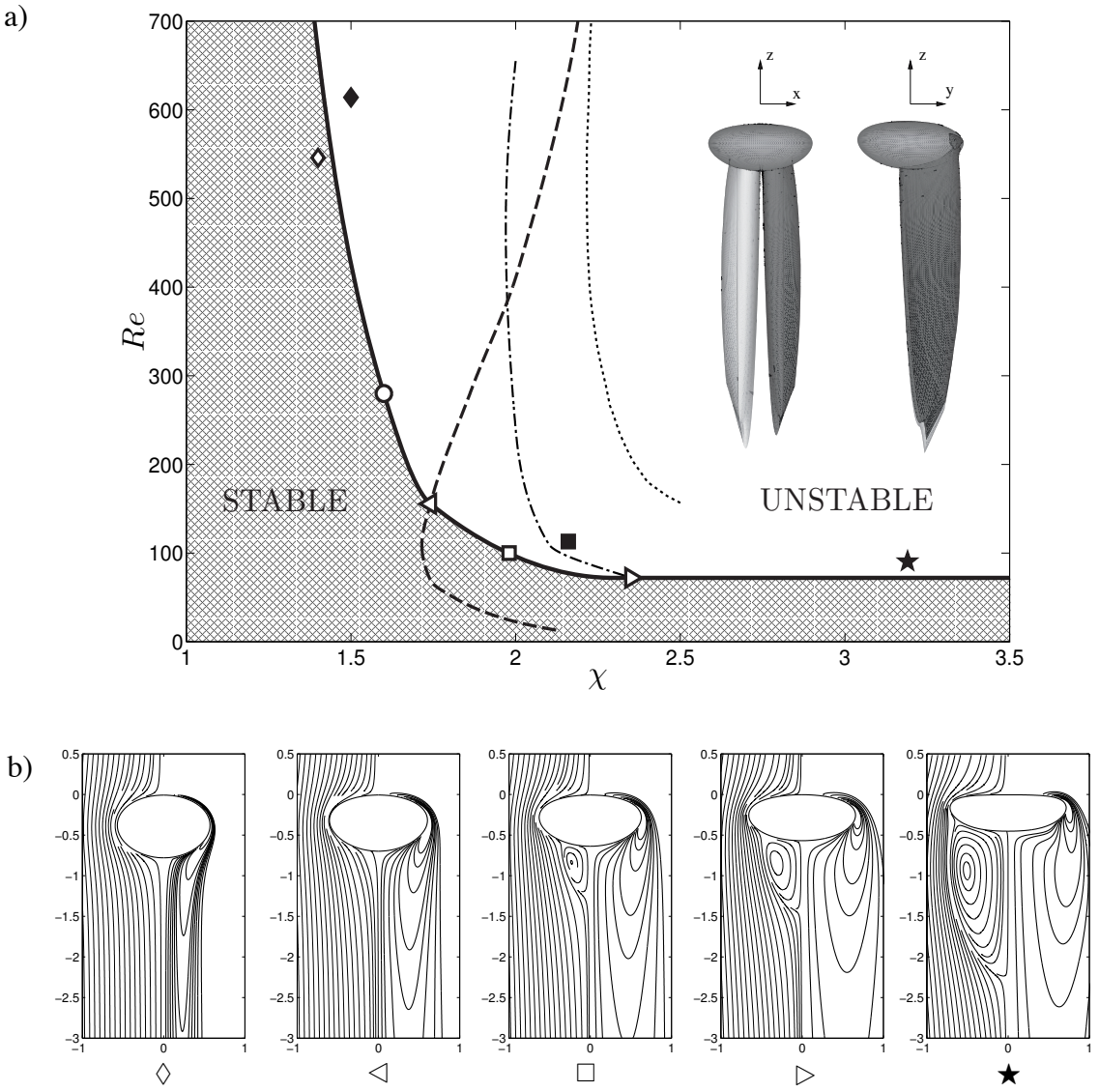

Figure 4.7: (a) Stability diagram for the development of zig-zag instability. Continuous line: present numerical results; dot-dashed line: experimental neutral curve by Zenit & Magnaudet [182]; dotted line: numerical results reported by Magnaudet & Mougin [84] assuming a spheroidal bubble. In addition, dashed line highlights the transition for the existence of standing eddy shown in Fig. 4.5. The inset shows the streamwise vorticity isocontours $\omega_z D/U_T = \pm 0.24$, corresponding to $Bo = 3.93$ and $Ga = 99.35$. (b) Bubble shapes, streamlines (left half) and azimuthal vorticity contours (right half) at several points close to the neutral curve. The physical properties of the symbols represented in the figure are summarized in Table 4.5.

	◊	⧫	◯	◁	□	■	▷	★
Ga	174.14	215.90		100	85.45	99.35	71.35	100
Bo	0.23	0.30		1.50	3.21	3.93	6.34	10
Re	546	614	280	181	100	113	70	99
χ	1.40	1.50	1.60	1.74	1.98	2.16	2.35	3.19
d_{m1}/d_{m2}	0.94	0.93		0.85	0.77	0.69	0.80	0.55
Mo	1.3E−11	1.3E−11		3.4E−8	6.2E−7	6.2E−7	9.9E−6	1.0E−5

Table 4.5: Characteristic properties of the points represented in Fig. 4.7. Symbols ◊ (rectilinear path) and ⧫ (zig-zag path) are experimental points by Veldhuis [170], □ and ■ show the rectilinear and oscillatory experiments by Zenit & Magnaudet [183], ◯ is a critical experimental point by Wu & Gharib [175] and ▷ corresponds to a critical experimental point by Zenit & Magnaudet [182]. The points represented by ◁ and ★ correspond to present numerical simulations. Notice that point ◊ corresponds to VLDS (S), □ to DMS-T05 (S), ■ to DMS-T05 (O) and ▷ to DMS-T11 data in Table 4.4.

to Veldhuis [170], see Fig. 7.14 and cases (a)-(b) in his dissertation, air bubbles ascending in pure water with small Bond numbers of 0.22-0.30 can be unstable for $Ga \approx 200$ ($Re \approx 575$), rapidly decreasing the critical Reynolds number as the aspect ratio χ increases. For instance, Wu & Gharib [175] established that, for $\chi = 1.6$ the critical Reynolds number for the onset of zig-zagging was about 280. Though they did not visualize the wake, this work will show it later, according to the analysis shown in this dissertation, the base flow does not exhibit a recirculation region for such a low value of χ.

To determine the transition curve for an unstable ascending motion of the bubble three-dimensional numerical simulations of the flow around a bubble, whose shape (and consequently its aspect ratio) and terminal velocity was previously obtained from the axisymmetric simulations described in Sections 4.3.1 and 4.3.2 in a wide range of Bond and Galilei numbers, have been performed. The main results are summarized in Fig. 4.7. For completeness, this figure also displays with a dashed line the transition curve for the presence of standing eddy shown in Fig. 4.6. Beginning with the case of spherical bubbles, to the best of our knowledge, there are no studies at low and moderate Reynolds numbers to verify Moore's result [94]. Thus, additional three-dimensional numerical simulations were performed to study the effect of the Reynolds number on the flow around spherical bubbles, within the range of $200 \leq Re \leq 15000$, increasing progressively the values of Re in steps of 100. It has been found that, unlike in the case of solid spheres, the flow was always axisymmetric and did not observe the formation of a standing eddy. Consequently, it can be concluded that that the flow around a sphere is stable independently of the value of Re when the zero-shear-stress (or shear free) boundary condition is imposed on its surface. However, the results of Fig. 4.5 suggest that the flow field around a bubble may become unstable without the presence of a recirculation region behind it. Thus, in the following, the evolution of the transition curve will be described as the bubble aspect ratio increases or, similarly, as the Bond number increases, and its relation with the existence/absense of a standing eddy in the wake of the bubble.

As the bubble aspect ratio increases, becoming slightly oblate, with $\chi \geq 1.4$, the flow is observed to be unstable at $Re \approx 700$. This result agrees with the experimental results of Veldhuis

[170] shown in Fig. 4.7a. In fact, as it is shown in Fig. 4.7b, the bubble denoted with ◊, whose aspect ratio is $\chi = 1.4$, has a fore-and-aft asymmetry of $d_{m1}/d_{m2} = 0.94$ (though it visually seems a spheroid), the axisymmetric basic flow does not display a recirculation region and exhibits the production of azimuthal vorticity in the boundary layer that develops on the bubble surface, whose maximum is found at the point of maximum curvature. For larger aspect ratios and Bond numbers, the critical Reynolds number further decreases, and the recirculation region develops along the neutral curve for $\chi \geq 1.74$ and $Re \leq 181$ (see point ◁ in Fig. 4.7). The vorticity field is more intense than those corresponding to lower aspect ratios, and can be associated with the increases in the value of the maximum curvature on the bubble surface due to the increment of the fore-and-aft asymmetry, even though the terminal velocity decreases. As a matter of fact, the asymmetry factor decreases to $d_{m1}/d_{m2} = 0.85$ (see Table 4.5) and the intensity of azimuthal vorticity in the region near the point of maximum curvature is higher than that corresponding to $\chi < 1.74$ (see for instance point ◊ in Fig. 4.7). A similar phenomenon can be observed for larger values of χ for which the recirculation area takes place. For instance, at $\chi = 1.98$ and $Re = 100$ (coordinates denoted with symbol □), the vorticity is produced near the point of maximum curvature of the bubble surface, and it is convected downstream, extending radially to a region larger than in the previous case of $\chi = 1.74$ and $Re \leq 181$ (indicated as ◁ in Fig. 4.7). This phenomenon induce to conclude that the degree of the fore-and-aft asymmetry, which increases along the neutral curve as χ increases and Re decreases, and the corresponding increase in the maximum curvature of the bubble, are the crucial parameters in the production of vorticity and, as a consequence, play a fundamental role in the destabilization of the axisymmetric base flow. Magnaudet & Mougin [84] showed that vorticity is the flow property by which the instability arises in the case of spheroidal bubbles with fore-and-aft symmetry, and proposed an argument based on their numerical observations. Their numerical results are also depicted with a dotted line in Fig. 4.7, showing that the flow behind a spheroidal bubble first becomes unstable for $\chi_c \approx 2.21$. However, the results of the present work agree with the experiments by Veldhuis [170] and Wu & Gharib [175], showing that it is possible to observe zig-zagging motion for $1.5 \leq \chi \leq 1.6$ at moderate Reynolds about $280 \leq Re \leq 600$. On the other hand, the base flow of unstable bubbles begins to exhibit a standing eddy for $\chi \geq 1.74$ due to the increase of vorticity brought to this area by convection [123]. Therefore, a major conclusion of the present work is the fact that fore-and-aft asymmetry induces an increment of vorticity strength, caused by an increase in the maximum bubble curvature, in good agreement with previous experimental studies.

The solid square (■) in Fig. 4.7 represents the zig-zagging bubble analyzed by Zenit & Magnaudet [183] using particle image velocimetry and DMS-T05 liquid. To illustrate the double-threaded structure ensuing in unstable flows, the inset of Fig. 4.7a depicts the streamwise vorticity field obtained from the three-dimensional numerical simulations of this study for the same vorticity values used in their Fig. 7 (i.e. $\omega_z D/U_T = \pm 0.24$). The unstable nature on the flow can be readily understood by the presence of a long wake, which generates a lift force on the bubble and causes it to rise in a non-straight path. Fig. 4.7a also shows the experimental neutral curve reported by Zenit & Magnaudet [182], which lies between the stable (hollow square) and unstable points (solid square) reported by Zenit & Magnaudet [183]. However, although the numerical results agree with the experimental results of de Vries [29], Veldhuis [170] and Zenit & Magnaudet [183], they deviate from those of Zenit & Magnaudet [182] as the Reynolds number increases, with the differences

vanishing for $\chi = 2.35$ and $Re = 70$. For the latter set of parameters, both the recirculation region and the vorticity strength are higher than for lower aspect ratios and, consequently, the critical value of Re further decreases. However, the dependence of the critical Re with χ (and Bo) is weaker for $\chi \geq 2$, since the fore-and-aft asymmetry varies more slowly in this case. To conclude, the base flow at $\chi = 3.19$ and $Re = 99$ (or $Bo = 10$ and $Ga = 100$) has been displayed in Fig. 4.7b, having a strong asymmetry of $d_{m1}/d_{m2} = 0.55$ (see Table 4.5). The standing eddy is obviously much larger than those observed at lower values of χ, and the vorticity strength also increases because the bubble adopts a shape with a flatter front and, consequently, a higher value of its maximum curvature.

Once again, it is important to highlight the relevance of considering the real shape of the bubble, that allowed to study the effect of fore-and-aft asymmetry on the critical Reynolds number for a wide range of aspect ratios ($1.4 \leq \chi \leq 3.2$) and Bond numbers ($0.23 \leq Bo \leq 10$), covering a range of Morton numbers from 10^{-12} to 10^{-4}. At a given aspect ratio, a critical Reynolds number lower than that obtained for fore-and-aft symmetric bubbles by Magnaudet & Mougin [84] (Fig. 4.7a) has been found. This fact indicates the increase of vorticity strength associated to the loss of fore-and-aft symmetry, and the destabilization of the base flow.

4.4 Conclusions

To sum up, in this chapter, the transition from rectilinear to zig-zag motion of a single bubble freely rising in a stagnant liquid, has been numerically investigated which depends on the fluids properties and the bubble size, analyzing the characteristics of the wake and the final shape adopted by the bubble. The real bubble shape has been taken into account, stressing the fact that it cannot be defined only by its aspect ratio, χ, since it is possible to obtain different bubble shapes with the same aspect ratio but different fore-and-aft asymmetries, by varying the Galilei and Bond numbers. Axisymmetric simulations have been performed to determine the transition curve for the presence of a standing eddy in the wake of the bubble as a function of the Galilei and Bond numbers.

In addition, three-dimensional numerical simulations have been performed to determine the stability characteristics of the flow around a bubble using the shape of the bubble and its terminal velocity provided by the axisymmetric numerical simulations. The unstable character of the axisymmetric base flow can be associated with the development of a pair of counter-rotating vortices as it was discussed by Mougin & Magnaudet [98] and Yang & Prosperetti [179], which induce a zig-zag ascending motion on the bubble. This transition from straight to zig-zag motion agrees with previous experimental results. Thus, a transition curve for the development of zig-zag instability has been constructed as a function of the bubble aspect ratio, χ, which depends on the bubble shape, and the Reynolds number based on the bubble terminal velocity, Re. It is shown that spherical bubbles are always stable independently of the Re, and that the critical value of Re for which the bubble becomes unstable decreases as the aspect ratio increases. The larger critical values of Re at lower χ correspond to smaller asymmetries in the bubble shape, i.e. shapes tending to spheres, as higher terminal velocities are required to deform the bubble generating azimuthal vorticity and a rotational flow field. The results differ form those reported by Magnaudet & Mou-

gin [84], who varied the aspect ratio considering a prescribed shape for the bubble (ellipsoid of revolution). Such differences highlight the importance of obtaining the real bubble shape in order to accurately determine the transition diagram. Furthermore, the results provided by the combination of axisymmetric and three-dimensional numerical simulations also report the existence of unstable bubbles not having a standing eddy in their wake, indicating that its presence is not a necessary condition for the onset of zig-zag motion. This bubble behavior differs from that of solid axisymmetric bluff bodies, which become unstable when a recirculating flow of a given length is already present behind the body. Such differences are simply attributed to the different boundary conditions that prevail on the surface of the body. While a zero-shear-stress (or shear free) boundary condition is imposed on the bubble interface, a non-slip condition is present on the surface of solid bodies causing the boundary layer separation and the formation of a recirculating flow in their wake at lower Reynolds numbers. Although, according to Fig. 4.7, boundary layer separation can also take place for bubbles whose aspect ratio is larger than 1.74, the flow around a bubble may exhibit non-oscillating instabilities, without the presence of a standing eddy, caused by the transport of vorticity generated at its surface.

Finally, in terms of numerical simulations of the ascending motion of bubbles, two-dimensional axisymmetric simulations can be performed in the case of stable bubbles, and more expensive, unsteady, three-dimensional numerical simulations are required for unstable bubbles. Thus, the transition curve can also be used to determine the type of simulations required to analyze the flow field.

CHAPTER
FIVE

Global Linear Stability Analysis of bubbles with fore-and-aft asymmetry

A global Linear Stability Analysis of the three-dimensional flow past a gas bubble rising in a still liquid is carried out, considering the actual bubble shape and terminal velocity obtained for various sets of Galilei (Ga) and Bond (Bo) numbers in axisymmetric numerical simulations. Hence, this study extends the stability analysis approach performed by Tchoufag *et al.* [150, 148] to the case of bubbles with fore-aft asymmetric shapes. The critical curve separating stable and unstable regimes for the straight vertical path is obtained both in the (Ga, Bo) and the (Re, χ) planes, where Re is the bubble Reynolds number and χ its aspect ratio (i.e. the major-to-minor axes length ratio). This provides new insight into the effect of the shape asymmetry on the wake instability of bubbles held fixed in a uniform stream and on the path instability of freely rising bubbles, respectively. For the range of Ga and Bo explored here, the stability results show that the flow past a bubble with a realistic shape (i.e. a flatter front and a more rounded rear) is more stable than that past a perfectly spheroidal bubble with the same aspect ratio.

This chapter is included in the paper "A global stability approach to wake and path instabilities of rising bubbles with a fore-aft asymmetric shape", by J.C. Cano-Lozano, J. Tchoufag, J. Magnaudet and C. Martínez-Bazán, submitted to the Phys. Fluids.

5.1 Introduction

Bubble rising in a quiescent liquid is a phenomenon of key interest in multiple environmental, geophysical and industrial contexts. The corresponding dynamics, i.e. the evolution of the bubble shape, the path that the bubble describes as it rises in a still liquid and the topology of its wake have been widely studied experimentally and numerically [25, 83, 37, 159]. However, from the experimental point of view, it remains a challenge to obtain quantitative data using ultrapure water [33, 34]. The addition of surfactants affects the dynamics of the gas-liquid interface, changing the shear-free condition into a no-slip one and altering, as a result, the path and wake of the bubble [146, 145]. Moreover, the presence of surfactants is known to increase the drag and hence decrease the critical Reynolds number (based on the equivalent diameter and terminal rise velocity of the bubble) and the critical aspect ratio beyond which the bubble path becomes unstable and departs from a vertical straight line. Surfactant effects may be eliminated by using nonpolar liquids, especially silicone oils [182, 183]. However, silicone oils have low surface tensions (typically four times lower than water), resulting in significant bubble deformations even for bubbles of small size. This limits somewhat the possibility to use them to explore in detail the stability

of the flow past moderately deformed bubbles, since the reduced size of the latter (compared to similar bubbles in water) increases the difficulty to obtain accurate measurements in the wake (e.g. through Particle Image Velocimetry). Whatever the selected carrying liquid, determining accurately the above critical parameters from experiments is not a trivial task: it requires sophisticated optical devices in at least two orthogonal planes, and a long tank because in certain regimes the bubble may travel a long distance before its path displays an instability. This is why experimental results may contain non-negligible errors if the tank used is not sufficiently long [130].

In order to avoid the inconveniences or go beyond the limitations mentioned above, Direct Numerical Simulations (DNS) have been increasingly used in the recent years to analyze the structure and stability of the flow induced by the bubble motion [98, 84]. These studies succeeded in determining the thresholds for the transition from straight to zig-zag bubble path though, in most cases, the bubble shape was considered fixed during its motion. Recently, Linear Stability Analysis (LSA) has also been proposed as a powerful tool to determine the neutral curves for wake [179, 150] and path [151] instabilities.

In the present study, a LSA is used to determine the transition to instability of the flow past a rising bubble using a realistic bubble shape, thus going a step further than the previous aforementioned works where a spheroidal shape was prescribed. Two different configurations are considered, namely the case of bubbles held fixed in a uniform stream on the one hand and that of freely rising bubbles on the other hand. Through this, we are able to analyze the influence of the fore-aft asymmetry of the bubble shape on the stability properties of the surrounding flow and of the bubble path. To facilitate the understanding of the findings obtained through these two complementary approaches, this stability study is divided in two parts. The one at hand deals with the results of the LSA approach while a second part reports on the novel wake topologies and bubble paths revealed by the DNS approach. The present chapter is organized as follows. Section 5.2 describes the LSA procedure and the results obtained through it with a fixed bubble exhibiting fore-aft asymmetry. Then Section 5.3 deals with freely moving bubbles with such an asymmetry and compares the corresponding LSA results with those obtained in the study performed by Tchoufag *et al.* [151] with perfectly spheroidal bubbles. The concluding Section 5.4 summarizes the main results.

5.2 LSA of the flow past fixed fore-aft asymmetric bubbles

The first part of the chapter is focused on the wake instability of bubbles whose shape, velocity and orientation are kept fixed once an equilibrium shape and a terminal velocity have been reached in an axisymmetric computation. The wake instability is assessed by means of the LSA approach. Two different codes are used in a complementary manner to carry out the study: the Gerris Flow Solver [110, 111] provides the final shape and rise velocity following the process described in Chapter 3, while FreeFem++ [57] is employed to achieve the LSA. The former is a finite volume multiphase solver in which interfaces are tracked using a Volume of Fluid (VOF) technique combined with a quad/octrees discretization, while the latter is based on the finite element method.

5.2.1 Problem configuration and methodology

The selected control parameters are the Galilei number, $Ga = \rho D\sqrt{gD}/\mu$ (also frequently referred to as the Archimedes number in stability studies), and the Bond number, $Bo = \rho g D^2/\sigma$, where ρ is the liquid density, D the equivalent bubble diameter such that the bubble volume equals $\pi D^3/6$, g is the gravitational acceleration, μ the liquid viscosity and σ the surface tension. These two dimensionless parameters are related to the Morton number, $Mo = g\mu^4/\rho\sigma^3$, which only depends on the fluid properties through $Mo = Bo^3/Ga^4$ so that they are indeed sufficient to characterize entirely the bubble shape and velocity. Note that, similar to the Reynolds number $Re = \rho U_T D/\mu$, the aspect ratio χ is not, strictly speaking, a control parameter but an outcome of the simulation for a given set (Ga, Bo). Therefore, a given value of χ may correspond to bubbles with different shapes, see Chapter 4.

In order to study the linear stability, Gerris Flow Solver is firstly used to compute the bubble shape and its terminal velocity, U_T, by means of axisymmetric direct numerical simulations of the full Navier-Stokes equations. For this purpose, the previous configuration employed in Chapter 3 is used, starting the simulations with a spherical bubble in a fluid at rest and considering gas/liquid density and viscosity ratios of 10^{-3} and 10^{-2}, respectively. Then, the bubble acquires its actual shape as it rises under buoyancy, until it eventually reaches a terminal velocity. The simulations are stopped when the terminal velocity and the shape are steady, i.e. remain unchanged over time (up to a certain precision lower than 1% for both U_T and χ, see Chapter 3). In a second step, we use FreeFem++ to perform the LSA of the flow around the bubble whose characteristics have been previously obtained.

In FreeFem++, the flow is governed by the incompressible Navier-Stokes equations which, using D and U_T as characteristic length and velocity scales, respectively, read in the dimensionless form

$$\nabla \cdot \mathbf{U} = 0, \tag{5.1}$$

$$\partial_t \mathbf{U} + \mathbf{U} \cdot \nabla \mathbf{U} = \nabla \cdot \mathbf{T}, \tag{5.2}$$

where ∂_t denotes the partial time derivative, $\mathbf{T} = -P\mathbf{I} + Re^{-1}\left(\nabla\mathbf{U} + \nabla\mathbf{U}^T\right)$ is the stress tensor, $\mathbf{I}$ the Kronecker tensor and Re the Reynolds number defined as $Re = \rho\, D\, U_T/\mu$. In addition, dynamic and kinematic boundary conditions are imposed at the bubble surface. This is achieved by assuming that the bubble does not deform any more after it has reached its terminal velocity (i.e. its shape is not altered by the small-amplitude pressure disturbances considered in the LSA approach) and that the viscosity of the gas that fills it is negligibly small, so that the continuity of shear stresses forces the outer fluid to satisfy a zero-shear condition at the bubble surface. These two conditions simply read

$$\mathbf{n} \times (\mathbf{T} \cdot \mathbf{n}) = 0, \tag{5.3}$$

$$\mathbf{U} \cdot \mathbf{n} = 0, \tag{5.4}$$

where $\mathbf{n}$ denotes the outward unit normal at the surface.

The flow is then classically split into the so-called base flow plus infinitely small disturbances (of order ϵ) around it. The bubble shape obtained with Gerris is frozen and the base flow past the

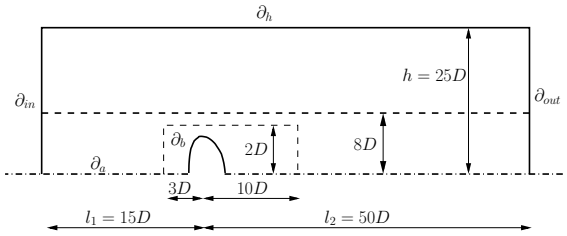

Figure 5.1: Sketch of the domain employed in the simulations performed with FreeFem++.

bubble held fixed is solved with FreeFem++, using the terminal velocity obtained with Gerris as the speed of the incoming stream. Then at order ϵ, the linearized perturbation problem resulting from (5.1)-(5.4) is solved to evaluate the stability of the previously computed base flow (see the computational domain sketched in Fig. 5.1). The finite element technique, with quadratic (resp. linear) elements for interpolating the velocity (resp. pressure) fields, is used to solve the $O(1)$ and $O(\epsilon)$ problems. More details on the weak formulation of the equations are given in Appendix A of [150].

5.2.2 Base flow problem

Governing equations

Following the LSA approach of [150], a strictly steady, axisymmetric base solution of the governing system (5.1)-(5.4) is searched. The work of Verfurth [172] described that a proper finite element formulation of the Navier-Stokes equations with a slip boundary condition requires the normal stress Σ at the corresponding surface to be added to the usual unknown velocity and pressure fields. Therefore, the governing equations of the base flow (characterized by velocity and pressure fields $\mathbf{U_0}$ and $\mathbf{P_0}$, respectively) to be solved in the cylindrical domain displayed in Fig. 5.1 read

$$\nabla \cdot \mathbf{U}_0 = 0, \tag{5.5}$$

$$\mathbf{U}_0 \cdot \nabla \mathbf{U}_0 = \nabla \cdot \mathbf{T}_0, \tag{5.6}$$

$$\mathbf{T}_0 \cdot \mathbf{n} = \Sigma_0 \, \mathbf{n} \quad \text{on} \quad \partial_b, \tag{5.7}$$

$$\mathbf{U}_0 \cdot \mathbf{n} = 0 \quad \text{on} \quad \partial_b, \tag{5.8}$$

$$\mathbf{U}_0 = \mathbf{e}_x \quad \text{on} \quad \partial_{in}, \tag{5.9}$$

$$\mathbf{T}_0 \cdot \mathbf{n} = \mathbf{0} \quad \text{on} \quad \partial_{out}, \tag{5.10}$$

$$\mathbf{e}_r \cdot \mathbf{U}_0 = (\mathbf{e}_r \cdot \nabla)(\mathbf{U}_0 \cdot \mathbf{e}_x) = 0 \quad \text{on} \quad \partial_a \cup \partial_h, \tag{5.11}$$

where Σ_0 denotes the base normal stress at the bubble surface, and $\mathbf{e}_x$ and $\mathbf{e}_r$ are the unit vectors in the streamwise and radial directions, respectively. Equation (5.11) expresses the symmetry condition on the domain axis and the shear-free condition on its lateral boundary. The system being nonlinear, the base flow solution is approached using an iterative Newton method, as described in [141].

Validation of the base flow

The base flow (and the $O(\epsilon)$ problem to be described later) was solved on the computational domain sketched in Fig. 5.1. This domain was discretized into triangular elements via a Delaunay-Voronoi algorithm. The corresponding grid was refined in a region close to the bubble ($3D$ ahead of it and $10D$ behind it) to make sure that the near wake is adequately resolved. The domain size and grid refinement were first validated by comparing results with those of previous studies devoted to spheroidal bubbles [150]. As shown in Table 5.1, predictions for the drag coefficient are in excellent agreement with those of [150].

χ	1			1.75			2.25		
Re	100	400	1000	166	332	830	100	500	1000
Present study	0.374	0.107	0.045	0.518	0.285	0.122	1.097	0.305	0.158
Tchoufag *et al.* [150]	0.374	0.107	0.045	0.518	0.285	0.122	1.097	0.305	0.158

Table 5.1: Drag coefficient C_D corresponding to a steady axisymmetric flow past a spheroidal bubble; C_D is defined as $(8/\pi)F_x$, where F_x denotes the dimensionless drag force.

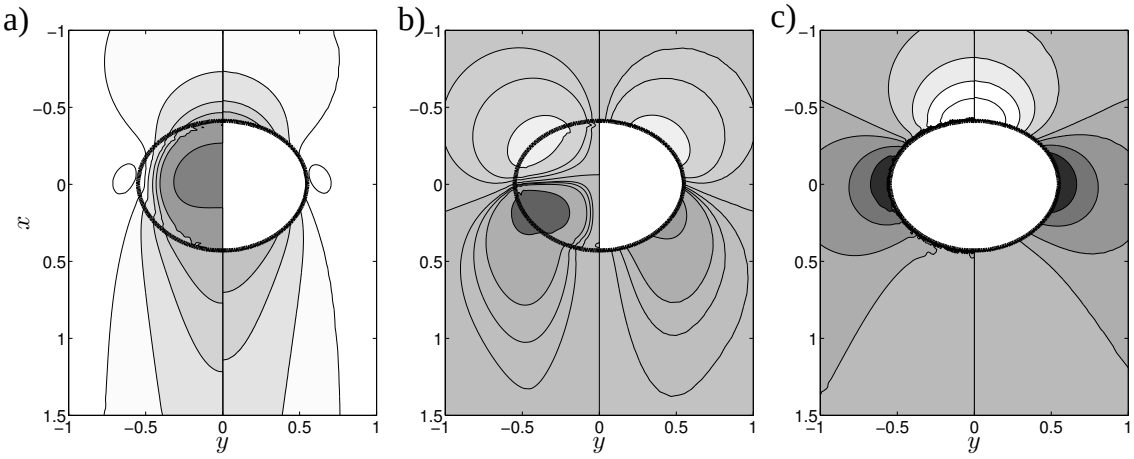

Figure 5.2: Comparison of the base flow obtained with Gerris (left) and FreeFem++ (right) for a bubble with $Bo = 1$ and $Ga = 50$. Iso-contours of dimensionless (a) axial velocity [-1, -0.5, 0.0, 0.2, 0.4, 0.7, 0.9, 1.0, 1.2], from dark to light, (b) radial velocity [-1.0, -0.25, -0.1, -0.07, -0.04, 0.0, 0.08, 0.15, 0.4], and (c) pressure [-0.6, -0.3, -0.15, -0.05, 0.0, 0.1, 0.2, 0.3, 0.4].

Furthermore, the base flow was compared with results provided by Gerris regarding the velocity and pressure fields and the development of a standing eddy at the rear of the bubble. Figure 5.2 shows that the pressure and velocity fields produced by the two codes are very close, although some tiny differences may be discerned in the near wake. The drag coefficients C_D provided by FreeFem++ were also compared with the quantity $C_{DG} = 4Ga^2/3Re^2$ provided by Gerris: indeed C_{DG} is the drag coefficient resulting from a balance between buoyancy and viscous forces. This comparison revealed a relative error generally lower than 5%, thus confirming the good agreement between the two codes. Moreover, the azimuthal vorticity created by the base flow over the bubble surface was computed and compared with the classical formula valid at a shear-free surface [10], namely $\omega = 2\kappa U_t$, where κ is the local curvature of the surface in the meridional plane and U_t is

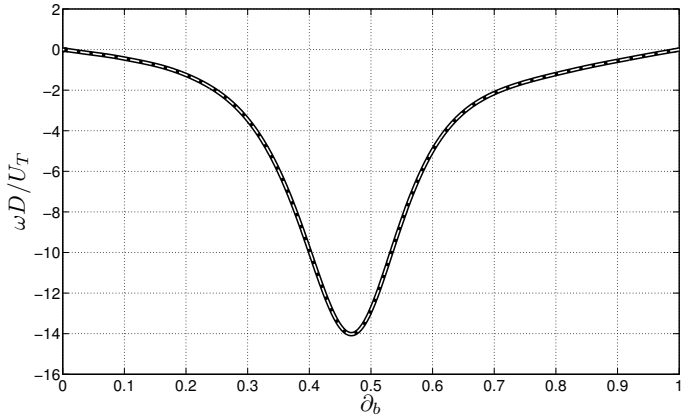

Figure 5.3: Vorticity distribution at the bubble surface obtained with FreeFem++ (solid line) and calculated as $\omega = 2\kappa U_t$ (white dashed line) using the interface geometry determined by Gerris for a bubble with $Bo = 2$ and $Ga = 80$; the left (right) extremity of the curve corresponds to the front (rear) stagnation point.

the tangential velocity of the fluid. Again the agreement is excellent, as revealed by Fig. 5.3. In this comparison, values of κ were directly recorded from Gerris, so that the observed agreement also allows us to conclude that the curvature of the bubble surface is well preserved from the determination achieved by Gerris to the FreeFem++ grid.

5.2.3 Perturbation problem

Governing equations

At order ϵ, the governing equations for the disturbances are obtained by linearizing the Navier-Stokes equations and the boundary conditions around the base state. The former read

$$\nabla \cdot \mathbf{u} = 0, \tag{5.12}$$

$$\partial_t \mathbf{u} + \mathbf{u} \cdot \nabla \mathbf{U}_0 + \mathbf{U}_0 \cdot \nabla \mathbf{u} = \nabla \cdot \mathbf{t}, \tag{5.13}$$

where $\mathbf{t} = -p\,\mathbf{I} + Re^{-1}\left(\nabla \mathbf{u} + \nabla \mathbf{u}^T\right)$ is the stress tensor disturbance. Equations (5.12)-(5.13) must be solved subjected to the boundary conditions

$$\mathbf{t} \cdot \mathbf{n} = \sigma_s\, \mathbf{n} \quad \text{on} \quad \partial_b, \tag{5.14}$$

$$\mathbf{u} \cdot \mathbf{n} = 0 \quad \text{on} \quad \partial_b, \tag{5.15}$$

$$\mathbf{u} = \mathbf{0} \quad \text{on} \quad \partial_{in} \cup \partial_h, \tag{5.16}$$

$$\mathbf{t} \cdot \mathbf{n} = \mathbf{0} \quad \text{on} \quad \partial_{out}, \tag{5.17}$$

where σ_s is the disturbance of the normal stress at the bubble surface. The boundary condition on the axis ∂_a depends on the symmetry of the mode under consideration. The solution of the linearized problem is sought in the form of normal modes. This solution is expanded in Fourier modes in the azimuthal direction θ, using the advantage of the axisymmetric geometry of the flow domain. Hence, the state vector $\mathbf{q} = (\mathbf{u}, p, \sigma_s)$ reads in the cylindrical (r, θ, x) coordinate system

$$\mathbf{q} = \hat{\mathbf{q}}(r, x) e^{\lambda t + \mathrm{i} m \theta} + c.c., \tag{5.18}$$

where *c.c.* denotes the complex conjugate. In this expansion, $\lambda = \lambda_r + \mathrm{i}\lambda_i$ is the complex eigenvalue whose real (imaginary) part is the perturbation growth rate (frequency), m being the azimuthal wavenumber. The stability analysis is restricted to $m = \pm 1$, since it has been established previously that these are the most unstable modes [84, 150]. Therefore, the appropriate boundary conditions on the domain axis ∂_a read

$$\mathbf{e}_x \cdot \hat{\mathbf{u}} = (\mathbf{e}_r \cdot \nabla)(\hat{\mathbf{u}} \cdot \mathbf{e}_r) = \hat{p} = 0\,. \tag{5.19}$$

Once the normal modes decomposition has been injected into the linearized equations, the system (5.12)-(5.17), (5.19) can be recasted in the form of a generalized eigenvalue problem

$$\lambda \mathscr{B}\hat{\mathbf{q}} + \mathscr{A}\hat{\mathbf{q}} = \mathbf{0}, \tag{5.20}$$

where $\mathscr{B}$ and $\mathscr{A}$ are the mass and stiffness matrices, respectively. In FreeFem++, these matrices are built using the UMFPACK library. The eigenvalue problem (5.20) is solved using a shift-invert Arnoldi technique implemented in the SLEPc library [1].

LSA results: influence of the bubble shape on wake instability

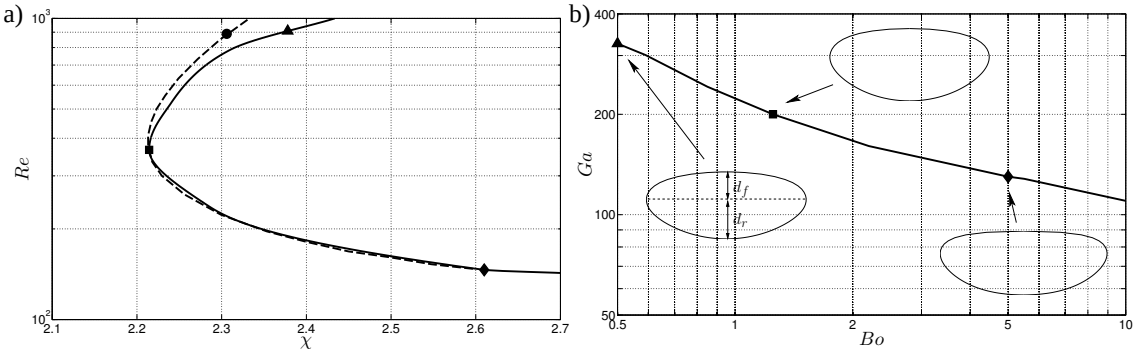

Figure 5.4: Neutral curves obtained from the LSA in the case of a fixed bubble: (a) comparison in the (χ, Re) plane between present results corresponding to a real bubble shape (solid line) and results from Ref. [150] for a spheroidal shape (dashed line); (b) Neutral curve in the (Bo, Ga) plane for a real bubble shape. In subfigure (a), the triangle, square and lozenge symbols identify the (χ, Re) coordinates of the three bubbles whose shape is displayed in subfigure (b); for these three bubbles, the ratio d_f/d_r defined in the figure, which is a measure of the fore-aft asymmetry, is 0.66, 0.68 and 0.52, respectively. The bullet in subfigure (a) identifies the point (χ_p, Re_p) discussed in the text.

The LSA results showing the neutral curve obtained in the case of a fixed bubble with fore-aft asymmetry are displayed in the plane of the control parameters in Fig. 5.4. For such a fixed body, the neutral curve separates regions of the parameter space where the axisymmetric wake is linearly stable or unstable. In Fig. 5.4(a) these results are compared with those obtained in [150] for a perfectly spheroidal bubble. In this case, the relevant control parameters are the bubble aspect ratio, χ, and the Reynolds number, Re, since the shape is prescribed and does not evolve with the Reynolds number. The neutral curve is also shown in Fig. 5.4(b) in the "natural" (Ga, Bo)

[1] http://www.grycap.upv.es/slepc/

plane, together with the bubble cross-section at three selected locations. For these three bubbles, the fore-aft asymmetry in the order of increasing Bo is 38%, 32% and 48%, respectively, i.e. it is a non monotonic function of the Bond number.

It appears that the fore-aft asymmetry has a non-negligible influence on the stability of the wake. More specifically, for a given aspect ratio larger than the critical value $\chi_c \approx 2.215$ corresponding to the "nose" of the neutral curve, it is seen to decrease the range of Re within which the wake is unstable, by moving the upper branch down. For instance, considering a bubble with an aspect ratio $\chi = \chi_p = 2.306$ and a Reynolds number $Re_p = 888.55$ (the point shown with a bullet in Fig. 5.4a) it turns out that the flow past the real bubble is stable while that past a perfectly spheroidal bubble is neutrally unstable. In contrast, shape asymmetry leaves the lower branch of the neutral curve almost unaffected. In physical terms, the stabilizing effect of the shape asymmetry may be understood by noting that, starting from an oblate spheroidal shape, flattening the front part and rounding the rear part may be obtained by imposing some slow suction on the former and some slow blowing on the latter (designed such that the total flow rate through the bubble surface is zero in order to keep its volume constant). Suction is known to make a boundary layer thinner and stabilize it, and so does the flattening of the front part on the boundary layer that develops from the front stagnation point of the bubble toward its equatorial plane. Blowing is also known to stabilize the near wake of bluff bodies by reducing or even suppressing the standing eddy that takes place there, thus weakening the source of wake instability [131, 15]. Oblate bubbles are basically bluff bodies on which most of the vorticity is produced in the vicinity of the equatorial plane ($\psi = 0$ in Fig. 5.5) which is the part of the surface where the curvature reaches its maximum [84]. On these grounds one can expect that, for a given curvature of the surface in the equatorial plane, making the rear part of the bubble more rounded stabilizes its wake. Hence, both mechanisms cooperate to make the flow past the bubble more stable.

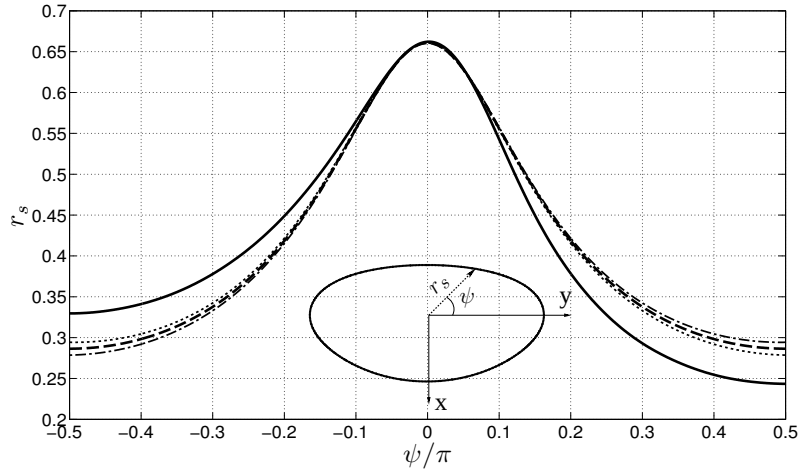

Figure 5.5: Different bubble shapes, all corresponding to $\chi = \chi_p$, in polar coordinates: the solid line shows the real bubble shape while the dashed line shows the perfectly spheroidal bubble. The dotted and dash-dotted lines represent bubbles whose shape is close to a spheroid but with a slightly flatter front and more rounded rear, and a more rounded front and slightly flatter rear, respectively.

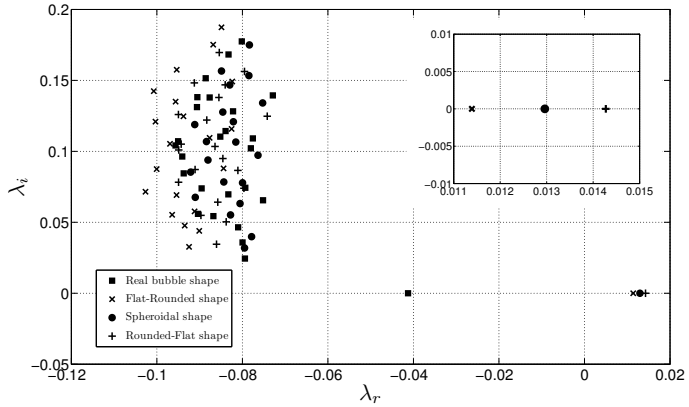

Figure 5.6: Eigenvalue spectrum for different bubble shapes, all corresponding to $\chi_p = 2.306$, at $Re_p = 888.55$. The inset shows the growth rates (λ_r) of the three unstable modes respectively obtained with the spheroidal, rounded-flat, and flat-rounded bubbles.

In order to better understand the influence of the bubble shape, employing these values of the parameters, $\chi = \chi_p$, $Re = Re_p$, to carry out the LSA of the flow past several bubbles with slightly different shapes. The various bubble shapes are displayed on Fig. 5.5 in polar coordinates. Four different shapes are investigated, including the "real" shape computed from Gerris and the spheroidal one. The other shapes were obtained by slightly deforming either the front or the rear of the spheroidal bubble, thus inducing a controlled fore-aft asymmetry. These shape alterations, resulting in a flatter front and a more rounded rear (or vice versa), were kept small in order to maintain the bubble volume constant. By these means, the equivalent diameter (and thus all dimensionless parameters) remains unchanged, allowing to isolate the particular influence of the bubble shape.

Figure 5.6 shows the eigenvalue spectra obtained with the four different shapes. It appears that, for the same value of the aspect ratio, the flow past the real-shape bubble is more stable than any of the other three. Moreover, the flow past a bubble with a slightly flatter front and a slightly more rounded rear, referred to as "*flat-rounded*" in the caption of Fig. 5.6, is somewhat more stable than that past the spheroidal bubble. Not unlikely, the opposite is observed in the case of a bubble with a slightly more rounded front and a slightly flatter rear (referred to as "*rounded-flat*"). These conclusions are in line with those of the sensitivity analysis carried out in [150] for perfectly spheroidal bubbles. There it was shown that a positive normal velocity disturbance applied to the bubble surface (hence leading to a local increase of the bubble radius) is destabilizing (stabilizing) when applied on the front (rear) part of the surface. Of course Fig. 5.6 also agrees with the latter work in that it confirms that for both spheroidal and fore-aft asymmetric bubbles, the primary wake instability occurs through a stationary bifurcation (i.e. with $\lambda_i = 0$). In [150], the full LSA diagram in the (χ, Re) plane also contains a branch defining a region where the axisymmetric wake becomes unstable through an unsteady (Hopf) bifurcation. This branch was not plotted here, although it also exists with real-shape bubbles, for two main reasons. First of all, only the first bifurcation can allow a direct comparison with experiments, except when the stationary and Hopf bifurcations occur within a small Re interval, a situation which may result in nonlinear modes interaction and resonance. Second, in the region $\chi \geq 2.41$ where the flow is unstable to unsteady

modes in the case of a spheroidal bubble, the Weber number $We = Bo(Re/Ga)^2$ comparing the inertia and surface tension effects is typically large enough to induce some wobbling of the bubble. Therefore, as the bubble shape remains unaffected by the disturbance, conclusions drawn in that regime would be somewhat questionable.

5.3 LSA of the flow past freely rising bubbles with fore-aft asymmetry

In the second part of this chapter, the configuration is turned where the bubble is no longer fixed but instead is free to rise under buoyancy. As in the previous configuration, bubbles whose shapes are obtained with Gerris for a given set of Ga and Bo are firstly calculated, and then are used in FreeFem++ to analyze the stability of their initially vertical trajectory. This vertical rise is investigated following a recent approach defined in the studies of Tchoufag *et al.* [151, 148] which is able to predict the stability fate of axisymmetric bodies by carrying out the LSA of the fully coupled fluid+body system.

5.3.1 Problem formulation

Following the aforementioned studies, a system of axes (x, y, z) translating and rotating with the bubble is introduced, being x aligned with its minor axis. The fluid problem is expressed using a cylindrical coordinate system (r, θ, x) related to the Cartesian coordinates (x, y, z) through $y = r\cos\theta$, $z = r\sin\theta$. The set of equations governing the moving bubble in a fluid otherwise at rest is made of the Navier-Stokes equations for the fluid and the Newton equations expressing momentum and moment of momentum conservation for the bubble. In the latter two, it is assumed that the gas that fills the bubble has a negligibly small density, so that the bubble mass and moment of inertia are neglected. Written in an absolute reference frame and projected onto the (x, y, z) axes, the corresponding system of governing equations reads

$$\nabla \cdot \mathbf{U} = 0, \tag{5.21}$$

$$\partial_t \mathbf{U} + (\mathbf{U} - \mathbf{W}) \cdot \nabla \mathbf{U} + \mathbf{\Omega} \times \mathbf{U} = \nabla \cdot \mathbf{T}, \tag{5.22}$$

$$\int_s \mathbf{T} \cdot \mathbf{n} \, \mathrm{d}S = \frac{\pi}{6} \mathbf{g}, \tag{5.23}$$

$$\int_s \mathbf{r} \times (\mathbf{T} \cdot \mathbf{n}) \, \mathrm{d}S = \mathbf{0}, \tag{5.24}$$

$$\frac{\mathrm{d}\mathbf{\Xi}}{\mathrm{d}t} = \mathbf{\Omega}, \tag{5.25}$$

where $\mathbf{W} = \mathbf{V} + \mathbf{\Omega} \times \mathbf{r}$ is the local entrainment velocity, $\mathbf{V}$ and $\mathbf{\Omega}$ being the translational and rotational bubble velocities, respectively, and $\mathbf{r}$ the local position vector measured from the geometrical centre of the bubble. Equation (5.25) relates at any time the rotation rate $\mathbf{\Omega}$ to the bubble orientation vector $\mathbf{\Xi}$ whose components are the roll/pitch/yaw angles with respect to a system of axes with a fixed orientation (x_0, y_0, z_0). Equations (5.21)-(5.25) have been made dimensionless using $(gD)^{1/2}$ as characteristic velocity (instead of U_T in Section 5.2). Consequently, the dimensionless

stress tensor is now $\mathbf{T} = -P\mathbf{I} + Ga^{-1}\left(\nabla\mathbf{U} + \nabla\mathbf{U}^T\right)$. In addition, in (5.23), the dimensionless gravity vector $\mathbf{g}$ is merely the unit vector $\mathbf{e}_{x_0}$ and $\pi/6$ stands for the dimensionless bubble volume.

The associated boundary conditions read

$$\mathbf{T}\cdot\mathbf{n} = \Sigma\,\mathbf{n} \quad \text{on} \quad \partial_b, \tag{5.26}$$

$$\mathbf{U}\cdot\mathbf{n} = \mathbf{W}\cdot\mathbf{n} \quad \text{on} \quad \partial_b, \tag{5.27}$$

$$\mathbf{U} = \mathbf{0} \quad \text{on} \quad \partial_{in}, \tag{5.28}$$

$$\mathbf{T}\cdot\mathbf{n} = \mathbf{0} \quad \text{on} \quad \partial_{out}, \tag{5.29}$$

where Σ is the dimensionless normal component of $\mathbf{T}$ at the bubble surface. The formulation of the corresponding LSA problem is now slightly modified with respect to that described in Section 5.2. The complete state vector for the fluid+bubble system is $\mathbf{Q} = [\mathbf{Q}^f, \mathbf{Q}^b]$, where $\mathbf{Q}^f$ corresponds to the fluid unknowns already involved in the fixed bubble configuration, and $\mathbf{Q}^b = [\mathbf{V}, \mathbf{\Omega}, \mathbf{\Xi}]$ gathers the unknowns corresponding to the bubble degrees of freedom. Again the state vector is split into a base state $\mathbf{Q}_0$ and a linear perturbation $\mathbf{q}$. The base state corresponds to the steady vertical rise of the bubble with zero inclination ($\mathbf{Q}_0^b = [\mathbf{V}_0, \mathbf{0}, \mathbf{0}]$) while the disturbance is expanded in the normal mode form as

$$\mathbf{q} = [\hat{\mathbf{q}}^f(r,x)e^{\mathrm{i}m\theta}, \hat{\mathbf{q}}^b]e^{\lambda t}. \tag{5.30}$$

Injecting this decomposition into the linearized Navier-Stokes and Newton equations, the problem can be recasted into a generalized eigenvalue problem formally similar to that defined by (5.20). This procedure as well as the structure of the corresponding stiffness and mass matrices were detailed in the works of Tchoufag *et al.* [151, 148]. Once these matrices have been built with FreeFem++, the linear system can be inverted, yielding the eigenvalues and the associated global modes of the fluid+bubble system. A large number of axisymmetric DNS were run with Gerris so as to obtain bubbles with a fore-aft asymmetric shape over a broad range of Ga and Bo (hence of Mo and Re). The LSA of each of these bubbles was then carried out in order to determine the corresponding neutral curve.

5.3.2 Results

A series of Gerris simulations were run keeping the Morton number fixed and varying the bubble equivalent diameter, i.e. varying Bo and Ga. This process was repeated for several values of Mo. The results corresponding to the LSA of the whole set of computed situations are gathered in Fig. 5.7. It is first observed that the flow past a freely rising bubble is more unstable than that past a fixed bubble since, for a given Bo, the transition to instability always takes place at a lower Ga. However, the two neutral curves actually coincide in the range $1.2 \lesssim Bo \lesssim 5.5$ and it is essentially for both low and large Bond numbers that the fore-aft asymmetry makes a significant difference.

Unlike the case of fixed bubbles, the neutral curve corresponding to freely moving bubbles with Mo of $\mathcal{O}(5\times10^{-7})$ exhibits a destabilization-restabilization behavior in the range $4.2 \lesssim Bo \lesssim 5$. Here, increasing the bubble size, i.e. varying Bo and Ga, the system first changes from stable to

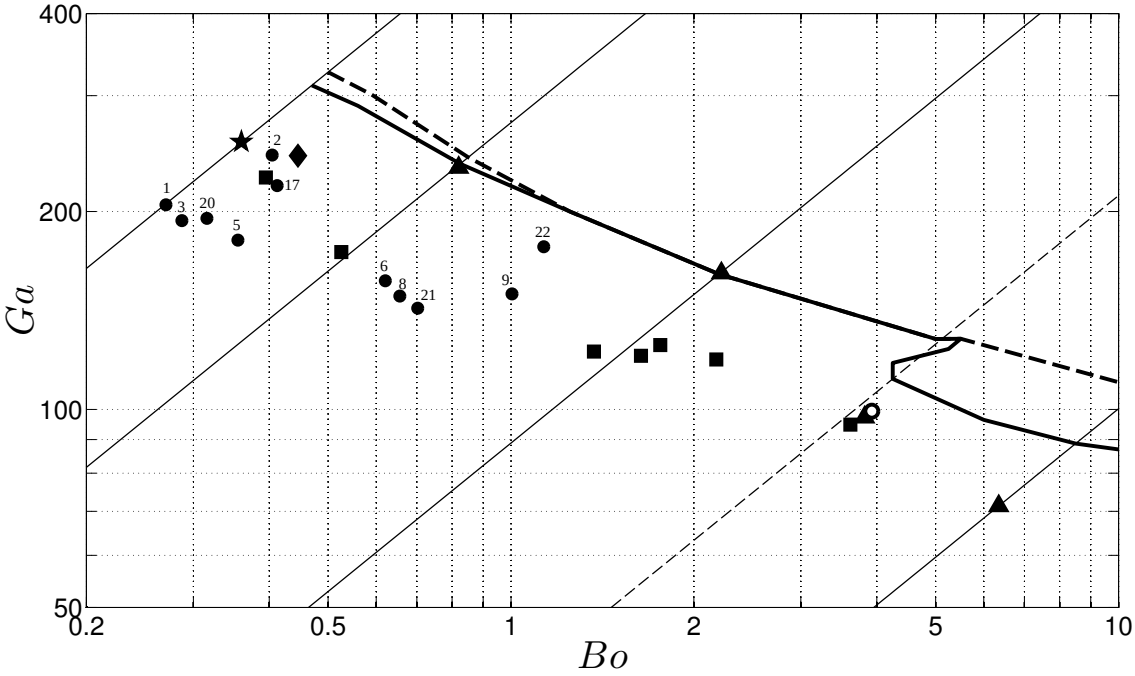

Figure 5.7: Neutral curves obtained in the (Bo, Ga) plane using LSA with fore-aft asymmetric bubbles. The dashed and solid lines correspond to the fixed and freely moving configurations, respectively. Experimental data corresponding to incipient path instability observed in various liquids are also included (■[163], ★ [29], ♦[34], ▲[182] and ○[183], •[55]; numbers associated with the latter data refer to those of Table 1 in [55]). The thin solid (dashed) lines correspond to iso-Mo lines (from left to right): 1.109×10^{-11} (water under standard conditions), 1.8×10^{-10}, 1.6×10^{-8}, 9.9×10^{-6} (5×10^{-7}).

unstable, then restabilizes for some time until it becomes unstable again. Thus, for a given Bo in the above range, there exists regions where, as Ga is increased, the system recovers its stability after the base state has been found unstable. This destabilization-restabilization process was already noticed with freely moving solid disks and thin cylinders [148] and perfectly spheroidal bubbles [151]. It may be relevant to phase change and mass transfer situations in which the bubble size varies in time.

Figure 5.7 also shows, along with LSA results, data points collected from various experimental studies [163, 29, 34, 182, 183, 55]. Although the general trend revealed by these data are similar to that displayed by the theoretical neutral curve, most of them fall below the LSA prediction. This may have several well distinct causes. First, it must be kept in mind that most experiments reported in [163] and [55] were carried out with polar liquids (water, mixtures involving water, alcohols). At the time of these experiments, and despite the care taken to purify these liquids, there were no means to eliminate entirely surfactants from them, so that the amount of contamination of the bubble surface is unknown. Since contamination is known to dramatically lower the critical Reynolds number (hence the Galilei number) of the transition [55, 83], one can suspect that a good part of the shift between LSA predictions and experiments is due to this phenomenon. In contrast, experiments corresponding to [34] and [29] were carried out in ultra pure water, whereas those corresponding to [182] and [183] employed various silicone oils, and these are nonpolar liquids

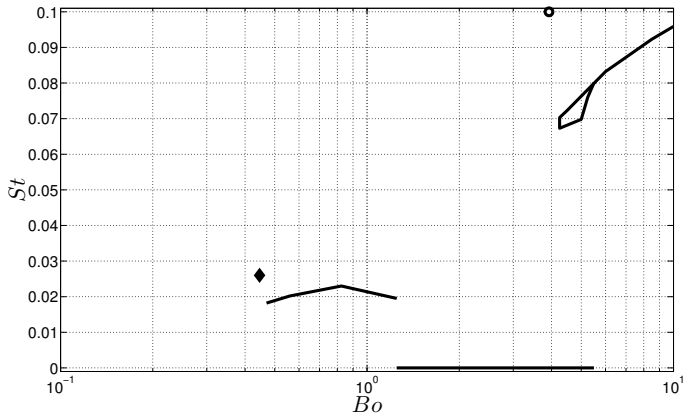

Figure 5.8: Frequency diagram (Bo,St) provided by the LSA approach for a freely moving bubble with a fore-aft asymmetric shape, together with experimental data from [33] (⧫) and [183] (○).

with which the bubble surface is easily kept clean. These are the two most stringent data sets to assess the validity and limitations of the LSA results. In pure water, transition to an unstable path has been reported to take place at $Re \approx 660$, i.e. $Ga \approx 246$ [34]. This is clearly lower than the LSA prediction which at the corresponding Bond number indicates a critical Galilei number slightly larger than 300. The most probable reason for this difference is that at such large Re, the flow past the bubble never reaches a strictly steady state: starting from rest, the rise velocity goes on increasing, although slightly, until path instability occurs. This is because the diffusion time $\rho D^2/\mu$ is much longer than the advective time D/U_T, so that physical processes governed by viscous diffusion, especially vorticity generation at the bubble surface, still evolve at the time the bubble has almost reached its terminal velocity. For this reason, the LSA approach based on a strictly steady base flow is probably not fully relevant and it would be more realistic to consider a slowly evolving base flow captured for instance in the relevant development stage of an axisymmetric DNS. Comparison of LSA results with data obtained in silicone oils shows an excellent agreement for the critical conditions corresponding to the smallest two values of the Morton number, i.e. to the range $0.8 \lesssim Bo \lesssim 2.2$. Here the critical Reynolds number ranges from 467 to 240 and the flow past the bubble has certainly reached a steady state before the instability manifests itself. The situation is different with the highest two values of the Morton number, where the data clearly fall below the theoretical critical curve. The corresponding Bond numbers being of $\mathcal{O}(4)$ or larger, the frozen shape assumption is not tenable any more: since surface tension effects get weak, flow disturbances probably induce slight deformations of the bubble surface, and this tends to accelerate the transition. To finish with this comparison, let point out that another scenario might have explained discrepancies between LSA predictions and experiments, namely the possible subcritical nature of the primary bifurcation, a situation that cannot be predicted by LSA. However, with spheroidal bubbles, DNS [98] and properties of the normal form derived from the system of governing equations (5.21)-(5.24)[149] confirmed the supercritical nature of the bifurcation throughout the whole range of aspect ratios covered by the LSA approach. Therefore it would be very unlikely that a subcritical bifurcation exists with fore-aft asymmetric shapes which remain close to an oblate spheroid. The conclusion of this analysis is that the present LSA seems to provide reliable quantitative predictions only within a limited range of Bond numbers, typically

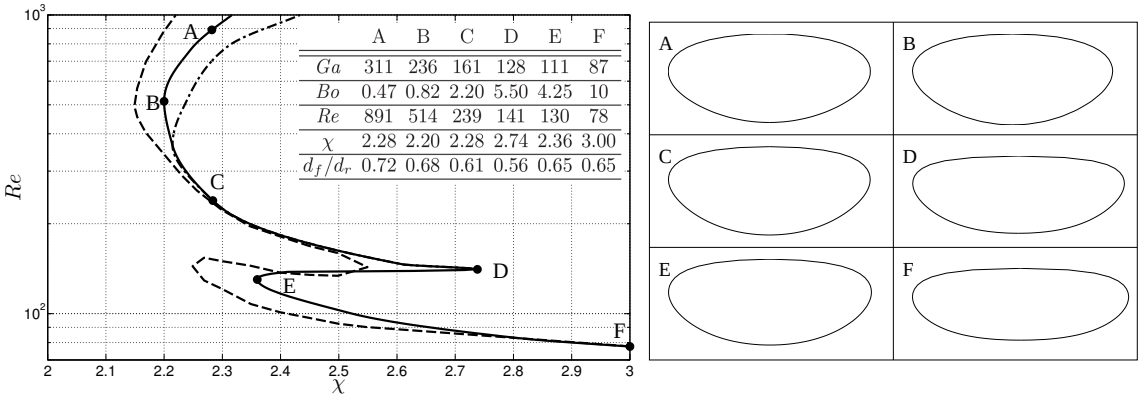

	A	B	C	D	E	F
Ga	311	236	161	128	111	87
Bo	0.47	0.82	2.20	5.50	4.25	10
Re	891	514	239	141	130	78
χ	2.28	2.20	2.28	2.74	2.36	3.00
d_f/d_r	0.72	0.68	0.61	0.56	0.65	0.65

Figure 5.9: Stability diagram of the flow about freely moving bubbles in the (χ,Re) plane. The solid and dashed lines correspond to the neutral curves obtained via LSA with a freely moving fore-aft asymmetric and a perfectly spheroidal bubble [151], respectively. The dash-dotted line corresponds to the neutral curve of a fixed, fore-aft asymmetric bubble (solid line in Fig. 5.4); for $Re \lesssim 370$, it almost coincides with the part of the solid line that ends at point D. Bubbles shapes at points A-F are shown in the right part of the figure; the table in the left part provides the coordinates (χ, Re) and (Bo, Ga) of these points and the ratio d_f/d_r of the front and rear semi-axes lengths of the corresponding bubbles.

$0.8 \leq Bo \leq 3-4$. Out of this range, present assumptions appear to be too restrictive.

Figure 5.8 reveals the evolution of the dimensionless frequency $St = \lambda_i/2\pi$ along the neutral curve. It turns out that, in contrast with the fixed-bubble situation where the first instability always occurs through a stationary bifurcation, the first unstable mode encountered with a freely moving bubble is generally oscillatory (i.e. the bifurcation is of Hopf type), yielding a periodic bubble path which may be planar (hence a zig-zag) or three-dimensional (a circular helix). A similar difference was noticed in [151] with spheroidal bubbles. However, in the intermediate range $1.2 \lesssim Bo \lesssim 5.5$, the primary bifurcation is still stationary, which yields a steady oblique bubble path beyond the threshold. This is why the two neutral curves corresponding to LSA predictions in Fig. 5.7 coincide in this intermediate range. At higher Bo, the first unstable mode exhibits "high frequency" oscillations with $St = \mathcal{O}(0.1)$. For $Bo \lesssim 1.2$, the primary bifurcation is again of Hopf type but the associated unstable mode exhibits "low-frequency" oscillations with $St = \mathcal{O}(0.02)$. Similar behaviors have been found experimentally, being the low-frequency path oscillation identified in the work of Duineveld [33] at $Bo \approx 0.44$ or the high-frequency zig-zag reported by Zenit & Magnaudet [183] at $Bo \approx 3.92$. The differences found between the experimental values of St and those predicted by the LSA are presumably due to the significant variations of the Strouhal number with the distance to the threshold, a shift that LSA can barely predict since it results in good part from nonlinear processes.

In order to facilitate the comparison of LSA results obtained with a fore-aft asymmetric bubble with those found with a perfectly spheroidal bubble, the two neutral curves have also been drawn in the (χ, Re) plane in Fig. 5.9. The figure also shows, for completeness, the bubbles shapes at six characteristic points along the neutral curve along with a table providing their coordinates (χ, Re) and (Bo, Ga) and the ratio of the front and rear semi-axes lengths, d_f/d_r. First, comparing

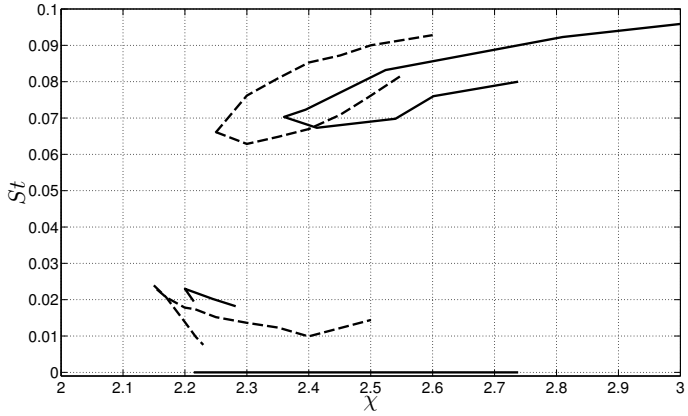

Figure 5.10: Frequency diagram (χ,St). Same convention as in Fig. 5.9.

with the corresponding neutral curve in Fig. 5.4, it appears that the lower part of the neutral curve obtained in the case in which the bubble is free to move has dramatically shifted towards lower Re. For instance the critical Reynolds number corresponding to $\chi = 2.5$ is about 161 in the fixed-bubble case, whereas it is close to 100 with a freely-moving bubble. Hence, as already mentioned, the flow around freely moving bubbles is generally significantly more unstable than that past fixed ones. What is specific to freely moving bubbles is the existence of the "high-frequency" branch that starts at the "trough" located at $\chi \approx 2.74, Re \approx 141$ and develops toward low Re. For increasing Reynolds numbers, this branch which has no counterpart in the fixed-bubble case provides the first bifurcation for bubbles with an aspect ratio larger than 2.36, i.e. a Bond number larger than 4.2. The comparison of the two neutral curves corresponding to freely moving bubbles in Fig. 5.9 reveals both differences and similarities. Roughly speaking, the neutral curve is shifted towards the right, i.e. towards higher χ, when the shape asymmetry is taken into account. Hence, the main difference is that the flow past bubbles with a fore-aft asymmetry (hence their path) is slightly more stable than that past a perfectly spheroidal bubble with the same aspect ratio. In particular it is seen that instability can only take place beyond a critical aspect ratio $\chi_c \simeq 2.15$ with spheroidal bubbles, whereas this threshold is increased up to $\chi_c \simeq 2.2$ with fore-aft asymmetric bubbles. However, one also observes that the global shape of the neutral curve is preserved, whether or not shape asymmetry is taken into account.

Figure 5.10 also shows that all three branches of high, low and zero frequency modes exist at quite similar locations in the (χ, St) plane for both bubble geometries; the associated frequencies are also close in the two of them. Last, the spatial structure of the unstable global modes are very similar. For instance, Fig. 5.11 displays the real and imaginary parts of the axial velocity and vorticity of the oscillating unstable mode corresponding to $Re = 134.6$ and $\chi = 2.54$ (i.e. $Bo = 5$, $Ga = 119.2$) for a bubble with fore-aft asymmetry. The observed structure is very close to that found with a spheroidal bubble (see Fig. 3 (c) and (d) of [151] which correspond to $Re = 90.6$ and $\chi = 2.5$). In Fig. 5.11(a) it may be noticed that the real part of the axial velocity and vorticity keep a constant sign along the streamwise direction, except in the very near wake. In contrast their imaginary parts are seen to change sign periodically in Fig. 5.11(b). This structural difference has been shown to be the generic footprint of a strong coupling between the body and the surrounding

fluid [148]. Therefore Fig. 5.11 indicates that the flow in the wake and the bubble path are strongly coupled in this region of the (χ, Re) plane.

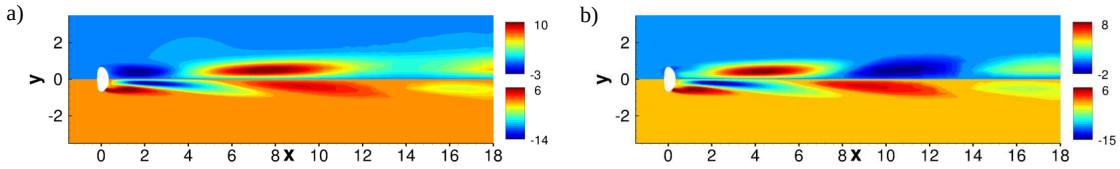

Figure 5.11: Unstable global mode at $Re = 134.6$ and $\chi = 2.54$ ($Bo = 5$, $Ga = 119.2$). Axial velocity (resp. vorticity) is on the top (resp. bottom) half; (a) real part, (b) imaginary part.

5.4 Conclusions

In this chapter, a global Linear Stability Analysis of the wake and path of gas bubbles rising in a stagnant Newtonian liquid, has been assessed focusing on the effect of the real bubble shape on the stability properties. This analysis has been performed in two-step approach. In the first step, the bubble shape and terminal velocity of the bubbles were obtained over a wide range of Galilei and Bond numbers from axisymmetric time-dependent numerical simulations implemented within Gerris Flow Solver. Then, the global Linear Stability Analysis has been carried out, keeping frozen the previously obtained shape, along two different scenarios. On the one hand we considered bubbles whose velocity and orientation were kept fixed, interacting therefore with the fluid only, like fixed bodies. On the other hand, bubbles were considered free to move and rotate, which required the coupled fluid+bubble system of linearized governing equations to be solved.

As in the case of spheroidal bubbles, the primary instability always occurs through a stationary bifurcation when bubbles are kept fixed. The results show that, for sufficiently large Reynolds numbers, the flow past a fixed fore-aft asymmetric bubble is significantly more stable than that past a perfectly spheroidal bubble. Hence, the fact that real bubbles with a given aspect ratio exhibit a flatter front and a more rounded rear than the corresponding oblate spheroid has been proven to stabilize the wake, confirming recent results provided by a sensitivity analysis [150]. In contrast, virtually no difference was found between the two geometries for Reynolds numbers less than approximately 370, leaving the lower branch of the neutral curve almost unaffected by the shape asymmetry.

To be in position to perform a direct comparison with experimental results, the global Linear Stability Analysis have been extended to freely rising bubbles with fore-aft asymmetry. As in the case of purely spheroidal bubbles, the neutral curve of the coupled fluid+bubble system was found to exhibit a much richer behavior than the fixed-bubble configuration. Indeed the first instability arises through a Hopf bifurcation associated to a low-frequency mode ($St \approx 0.02$) at low Bond numbers (high Galilei numbers, i.e. $Ga \gtrsim 200$) and to a high-frequency mode ($St \approx 0.10$) at high Bond numbers (low Galilei numbers, i.e. $Ga = \mathcal{O}(100)$), whereas it occurs through a stationary bifurcation in the intermediate range $1.2 < Bo < 5.5$. Compared to the flow past a perfectly oblate spheroidal bubble, that past a bubble with fore-aft asymmetry has been found to be more stable

for both low (typically $\lesssim 1$) and large (typically $\gtrsim 5$) Bond numbers, whereas the asymmetry does not modify its stability in the intermediate range corresponding to the stationary bifurcation. For liquids with Morton numbers of $\mathcal{O}(5 \times 10^{-7})$, there is a subregion in the range $4.2 < Bo < 5$ with no counterpart in the fixed-bubble configuration, where the flow becomes unstable beyond a critical Galilei number of $\mathcal{O}(110)$, then restabilizes at slightly higher Galilei numbers until it eventually becomes unstable again beyond $Ga = \mathcal{O}(130)$ (see Fig. 5.7).

Present results clearly improve over those of [151] by considering realistic bubble shapes on which the normal stress balance is satisfied everywhere as far as the flow is steady and axisymmetric. However, consistent quantitative discrepancies with respect to recent experimental data obtained in uncontaminated liquids remain, regarding critical conditions in the low- and high-Bo ranges defined above. In the low-Bo range, the discrepancies can be suspected that they are due to the remaining unsteadiness of the base flow at the time the instability starts to manifest itself, a feature not taken into account in the present LSA where a strictly stationary base state is assumed. In the high-Bo range, small amounts of energy are sufficient to induce local changes in the bubble shape and it is likely that pressure disturbances associated with the onset of the instability result in significant shape disturbances whose effect on the stability of the whole system is not taken into account in the present LSA scheme. At low Bond numbers, where the transition occurs at high Galilei numbers, the Reynolds numbers are large and it could be possible that in this range of Reynolds numbers, the flow evolves in time when the bubble is experimentally injected while the LSA assumes a stationary base flow. To overcome these limitations, three-dimensional numerical simulations have been performed in which the above two restrictions are removed since the flow and the bubble shape are allowed to evolve all along the simulation. The corresponding results, primarily aimed at elucidating the differences observed between LSA results and experimental measurements, will be discussed in the following Chapter 6.

CHAPTER
SIX

Wakes and paths of real shape bubbles

Direct Numerical Simulations (DNS) of a bubble freely rising in still liquids have been performed to analyze the bubble dynamics behaviour in the region near the transition between stable and unstable modes. These have been previously defined by the neutral curve described in Chapter 4, the curve generated by the Linear Stability Analysis (LSA) in Chapter 5 and the experiments carried out by other authors, see Fig. 1.2 in Chapter 1. The path and the vortical structure developed in the wake are assessed for each of the different simulated bubbles, by describing the flow regimes that characterize the motion. The numerical results reveal new regimes, such as chaotic or Reflectional-Symmetry-Breaking (RSB), as well as the traditional regimes with rectilinear, zig-zag and spiral paths. In addition, the temporal evolution of the terminal velocity, i.e. the Reynolds number, has also been studied to analyze its variation during the rising motion.

This chapter is included in the paper "Wakes and paths of bubbles with fore-aft asymmetry", by J.C. Cano-Lozano, C. Martínez-Bazán, J. Tchoufag, and J. Magnaudet, under preparation to be submitted to Phys. Fluids.

6.1 Introduction

Leonardo's paradox [114] was the name employed by the science community to define the phenomenon whereby a bubble rising in a still liquid may follow a rectilinear, zig-zag or spiral trajectory depending on the fluids properties, the bubble size and the gravitational acceleration. This phenomenon, in which the bubble shape, path and wake are intimately related, has been widely studied. However, its hydrodynamic behaviour is not fully understood yet. As discussed in Chapter 4, the first studies were performed by Haberman & Morton [53], who fixed the Morton number, $Mo = g\mu^4/\rho\sigma^3$, being g, μ, ρ and σ the gravitational acceleration, liquid viscosity, liquid density, and surface tension, respectively. Their study described three different paths: rectilinear, spiral and straight rocking as a function of the bubble size and the Mo number (water). Then, a great deal of experimental and numerical studies have been performed to analyze the bubble shape, terminal velocity, wake and path, see the studies [25, 29, 170, 37] and references therein.

The transition from rectilinear to oscillatory motion, i.e. from a stable to an unstable bubble, has tried to be defined by means of experimental data carried out by different researchers [125, 163, 34, 29, 170, 88, 182, 133]. Some of these data can be seen in Fig. 6.1. However, the transition region concerns a wide area in the $\{Bo,Ga\}$-plane, due to, among other things, the influence of the experimental set-up on the threshold, which was analyzed by Sanada *et al.* [130].

Moreover, the surfactants may affect the interface, modifying the shear-free boundary condition and therefore, the path instability [145].

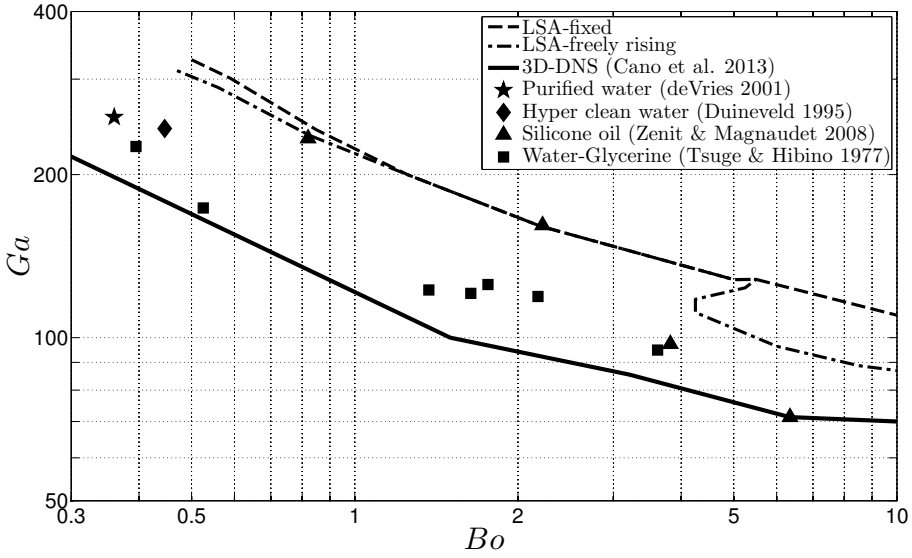

Figure 6.1: Phase Diagram (Bo,Ga) showing the transition curve obtained with three-dimensional simulations performed in Chapter 4 using the real bubble shape (solid line), the neutral curves defined with the LSA (dashed and dot-dashed lines), Chapter 5, and experimental data in the transition region from rectilinear to oscillatory motion obtained by other researchers [163, 34, 29, 182].

In addition to the experimental studies, the transition has also been numerically assessed. The neutral curve has been obtained by means of Direct Numerical Simulations (DNS) where the bubbles have been considered to have realistic shapes, see Chapter 4, but without deformations at the interface, i.e. using a frozen shape (Fig. 6.1, solid line), and employing a global Linear Stability Analysis (LSA), see Chapter 5, by both fixing and letting the movement of the bubble free (Fig. 6.1, dashed and dot-dashed lines).

Despite the disagreement between the experiments and simulations shown in Fig. 6.1, previous studies have allowed us to assess the bubble wake behaviour. It is known that the wake changes from presenting an axisymmetric pattern in a stable bubble to the disposal of two counter rotating vortices in an unstable one, as experimentally demonstrated by de Vries *et al.* [30], Zenit & Magnadut [182] and numerically reported by Mougin & Magnaudet [98, 84]. Those studies showed that the zig-zagging bubble develops two threads with a symmetry plane. In addition, the bubble wake has recently been numerically analyzed via the application of three-dimensional numerical simulations performed by some researchers [46, 184, 159], who allowed the presence of bubble surface deformations during the ascent. Nevertheless, those studies do not show a clear structure as the one achieved by Mougin & Magnaudet [98, 84] using spheroidal shapes or the numerical results shown in Chapter 4 with the frozen real shape.

The aim of this chapter is to analyze the bubble hydrodynamic behavior during the ascent in still liquids between the neutral curves obtained via a real frozen shape, as obtained in previous

chapters, i.e. from stable to unstable motion as a consequence of the discrepancy between the experimental results and the aforementioned neutral curves. Paths and wakes of different bubbles are shown as a function of the Bond and Morton numbers, as well as of the temporal evolution of the Reynolds number. The chapter is organized as follows: the numerical method and validation are described in section 6.2. Then, in section 6.3, the numerical results of the paths and wakes are shown together with the evolution of the Reynolds number. The different flow regimes detected are also described and their main features are highlighted. Finally, the conclusions are summarized in section 6.4.

6.2 Numerical method and validation

Three-dimensional DNS of a bubble rising have been carried out, being the movement freely driven by the buoyancy, to analyze the path and wake of bubbles in the transition region. In these simulations the bubble's inner and outer flow fields are resolved, i.e. the gas and liquid flows, allowing deformations at the surface during the upward movement, in opposition to the frozen shapes employed in Chapters 4 & 5. These numerical simulations were performed by employing Gerris Flow Solver [110] and the VOF technique to track the interface. The equations implemented in the solver, as applied to bubble rising, were described previously in Chapter 3. Furthermore, the discretization technique and additional computational details on the Gerris code can be read in Popinet's studies [110, 111].

In this chapter, the numerical simulations were performed in a three-dimensional domain of $8D \times 8D \times 120D$ size. The domain was discretized in square finite volumes, hierarchically organized as a quadtree, which allows for a concentration of the mesh cells at the interface and, specially, in wake region, by refining therefore a region of $2D \times 2D \times 10D$ in the bubble and wake zone. Moreover, in some bubbles with bigger lateral movement, the fine region was increased to a $4D \times 4D \times 20 \sim 30D$ size depending on the wake length. The resolution mesh was the same as the one employed in Chapter 3, where a comparison between two and three-dimensional simulations was carried out obtaining a good agreement. This comparative analysis was employed afterwards to validate the numerical results obtained in this chapter. The mesh at the interface has a lower density grid than the one employed in Chapter 4, namely, level 3, as shown in table 4.1. Additionally, the bubble tail has a lower refinement level with regard to the resolution mesh at the interface. This grid size and its refinement level provide accurate resolution to distinguish the actual vortical structure in the wake, with respect to the erroneous numerical vorticity, thus avoiding its numerical diffusion. The boundary conditions applied to the domain, were slip at the bottom and lateral walls and outflow in the top boundary, equally to the ones used in the axisymmetric configuration. In addition, a sphere at rest was employed for the initial condition, as it has been done in previous chapters. It should be pointed out the high computational cost of these simulations due to the great number of necessary cells to resolve the wake in a coherent manner, thus reducing the numerical error. Contrary to Chapter 4, where the simulations were performed using the frozen shape obtained in the axisymmetric simulations, such shapes were later run in a three-dimensional domain where the surface cannot be modified. However, in this part of the dissertation the bubble surface has the ability of being deformed during the rising motion,

thereby attaining a good bubble-fluid iteration.

6.3 Results

The present section shows the main results obtained in the numerical simulations of the bubble rising in order to determine its dynamic behavior. Paths and wakes of different bubbles are shown in the following subsection, as a function of the Morton and Bond numbers, together with the temporal evolution of the shape and the vortical structure. In addition, the progress of the Reynolds numbers is analyzed for different flow regimes.

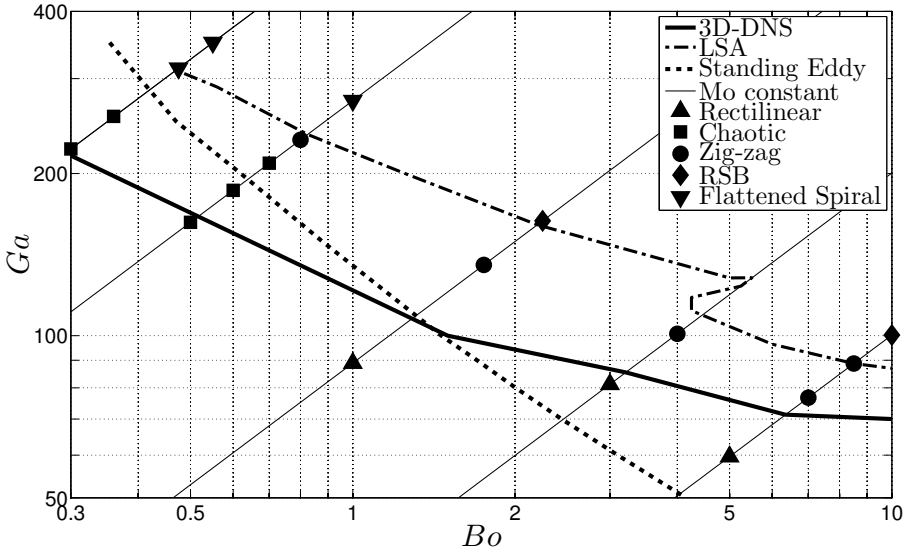

Figure 6.2: Phase diagram (Bo,Ga) showing the three-dimensional numerical simulations carried out in this study, distinguishing between the different flow regimes obtained, together with the neutral curves described in Fig. 6.1. The dotted line represents the onset of the standing eddy.

Figure 6.2 represents a summary of the different numerical simulations performed in this part of the dissertation, defining the motion described during bubble rising. The simulations were carried out by using five Morton numbers (see table 6.1), $Mo = g\mu^4/\rho\sigma^3$, and varying the Bond number, $Bo = \rho g D^2/\sigma$, where D is the equivalent diameter, following the process described in the previous chapter. In this case, the Mo numbers correspond to ultra pure water and different silicone oils, which were experimentally employed by de Vries *et al.* [30] and Zenit & Magnaudet [182] respectively to study the transition mode from an experimental point of view. Moreover, table 6.1 shows the dimensionless numbers, including the Galilei number $Ga = \rho_l\, g^{1/2}\, D^{3/2}/\mu_l = Bo^{3/4}/Mo^{1/4}$, the motion characteristics identified during the ascension and the Strouhal number, $St = fD/U_T$, where f is the frequency and U_T is the average terminal velocity. Hereafter, the characteristic scales are the equivalent diameter D for the length and $\sqrt{D/g}$ for the time, being the figures non-dimensionally plotted. Moreover, the vortical structure will be drawn by employing

the streamwise vorticity as,

$$\omega_x = \frac{\partial w}{\partial y} - \frac{\partial v}{\partial z}, \tag{6.1}$$

as well as the λ_2 criterion defined by Jeong & Hussain [64].

6.3.1 Bubble motions: shapes, paths and wakes

Rectilinear regime

Initially, we consider bubbles with spherical or spheroidal shape and a little fore-aft asymmetry, i.e. a bubble with an aspect ratio χ close to 1.1, see Chapter 4. They rise following a rectilinear path as can be observed in Fig. 6.3 for bubble number 15 in table 6.1. The straight trajectory is identical to the simulated bubbles number 10, 13 and 15, being the flow axisymmetric in all cases and considering the stable mode for this regime. In such stable regime, the bubble rising keeps the bubble shape without alterations and therefore, the aspect ratio does not change during the ascent. Additionally, Fig. 6.3(c) shows the streamlines in a bubble with a standing eddy, which confirms that the recirculation region in the wake is axisymmetric with a toroidal vortex.

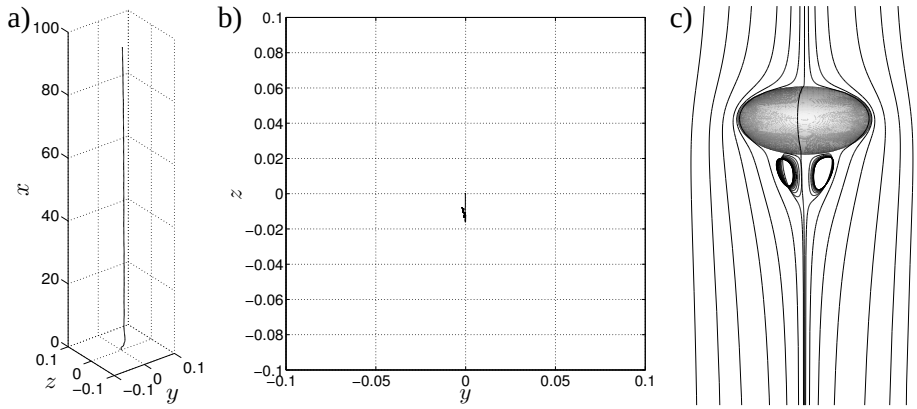

Figure 6.3: a) Three-dimensional reconstruction and b) projection onto a horizontal plane, of the trajectory corresponding to a rectilinear motion (Bubble number 15 in table 6.1). c) Streamlines of the flow around the bubble showing the standing eddy.

Chaotic regime

The name chaotic has been used to describe the path drawn by a body with irregular motion, i.e. a nonstraight trajectory with a chaotic flow field. This irregular motion occurs in some bodies, such as spheres, thin disks and flat cylinders [37], appearing after helical motions, including the case of bubbles as pointed out by Veldhuis *et al.* [169]. In those studies, the flow becomes chaotic too. Regarding our study, an irregular motion has been attained in the first transition between rectilinear and spiral trajectories for low Morton numbers, see the Fig. 6.2. Nevertheless, despite the existence of irregularities in the path, as can be observed in Fig. 6.4, the flow does not develop a chaotic wake. The figure shows the chaotic trajectory for bubble number 2 in table 6.1, similarly

Case	*Liquid*	*Mo*	*Bo*	*Ga*	*St*	Path	Wake	Regime
1	Water	1.109×10^{-11}	0.3	222.13	-	Chaotic	2CRV aperiodically	Chaotic
2	Water	1.109×10^{-11}	0.36	255.28	-	Chaotic	2CRV aperiodically	Chaotic
3	Water	1.109×10^{-11}	0.475	313.54	0.042	Elliptical spiral	2CRV-Hairpin vortex	Flattened Spiral
4	Water	1.109×10^{-11}	0.55	350.20	0.045	Elliptical spiral	2CRV-Hairpin vortex	Flattened Spiral
5	T00	1.8×10^{-10}	0.5	162.34	-	Chaotic	2CRV aperiodically	Chaotic
6	T00	1.8×10^{-10}	0.6	186.12	-	Chaotic	2CRV aperiodically	Chaotic
7	T00	1.8×10^{-10}	0.7	208.93	-	Chaotic	2CRV aperiodically	Chaotic
8	T00	1.8×10^{-10}	0.8	230.94	0.054	Zig-zag	2CRV	Zig-zag
9	T00	1.8×10^{-10}	1	273.01	0.060	Elliptical spiral	2CRV-Hairpin vortex	Flattened Spiral
10	T02	1.6×10^{-8}	1	88.92	0	Rectilinear	Axisymmetric	Rectilinear
11	T02	1.6×10^{-8}	1.75	135.3	0.073	Zig-zag	2CRV	Zig-zag
12	T02	1.6×10^{-8}	2.25	163.35	0.090	Elliptical spiral	2CRV-RSB	RSB
13	T05	6.2×10^{-7}	3	81.23	0	Rectilinear	Axisymmetric	Rectilinear
14	T05	6.2×10^{-7}	4	118	0.104	Zig-zag	2CRV	Zig-zag
15	T11	9.9×10^{-6}	5	59.61	0	Rectilinear	Axisymmetric	Rectilinear
16	T11	9.9×10^{-6}	7	76.72	0.120	Zig-zag	2CRV	Zig-zag
17	T11	9.9×10^{-6}	8.5	88.74	0.132	Zig-zag	2CRV	Zig-zag
18	T11	9.9×10^{-6}	10	100.25	0.174 (0.136)	Helix (Spiral)	2CRV-RSB	RSB

Table 6.1: Characteristic properties and dimensionless numbers of the three-dimensional DNS performed in this chapter. 2CRV (two Counter Rotating Vortices). RSB (Reflectional Symmetry Breaking).

to the one observed in the disks-spheroids described by Ern *et al.* [37], Chrust *et al.* [24] or in the spheres reported by Zhou & Dušek [185]. It is remarkable to note the absence of standing eddy in the bubble tail, see the standing eddy curve in Fig. 6.2, and the development of two counter rotating vortices, which demonstrates that the presence of a recirculation region is not necessary to achieve an unstable motion, as reported by de Vries [29] and numerically demonstrated in Chapter 4.

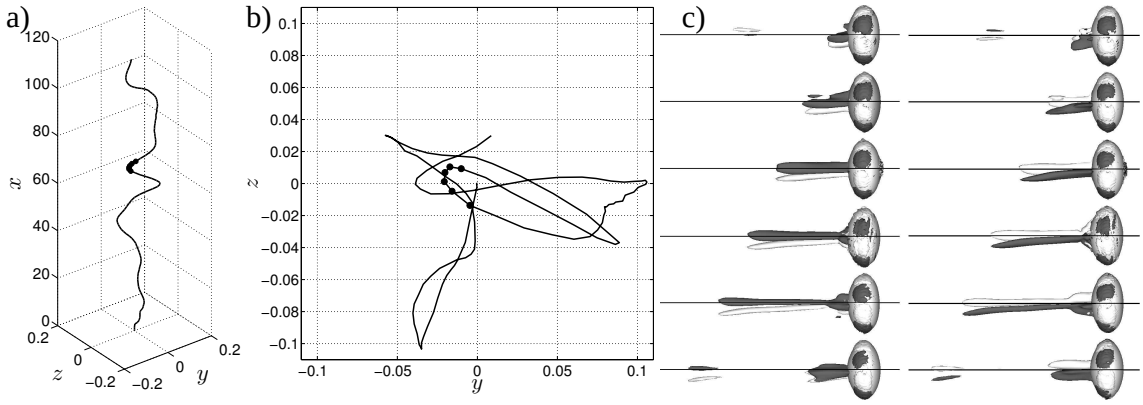

Figure 6.4: a) Three-dimensional reconstruction and b) projection onto a horizontal plane, of the trajectory corresponding to a chaotic regime (Bubble number 2). c) Temporal evolution (figures decrease as time and x position increase) of the streamwise vorticity isocontours $\omega_x D/U_T = \pm 0.24$ corresponding to the bullets in (a,b). The right column corresponds to the view twisted 90°. The solid line marks the x-axis of the initial bubble position.

The path undergoes abrupt changes due to the aperiodically growth and shedding of double thread structure, which ensures an unstable flow, Fig. 6.4(c). In this regime, the streamwise vorticity is not strong enough to produce a lift force sufficient to get a greater oscillation motion, and therefore it becomes irregular. Figure 6.4(b) shows that in this bubble, the lateral displacement is very small (max. 15% of the D), but nevertheless this should not be considered a rectilinear trajectory, where the maximum lateral displacement is less than 1%, see Fig. 6.3. In addition, the threads are connected to the bubble in its rear stagnation point, which prevents inducing a torque on the bubble. Otherwise, an even higher torque would lead to its inclination.

Figure 6.4(c) shows the bubble shapes, which exhibit little oscillations. Nevertheless, these variations are below 5% with respect to the aspect ratio χ. Moreover, the vortical structure presents a symmetry plane, its orientation being defined as a function of the bubble position, which is opposite to a zig-zaging behavior, where the symmetry plane is constant independently of the bubble position. The orientation of the symmetry plane can be considered as a constant if the reference system is positioned in the bubble in this regime. Figure 6.5 shows the vortical structure employing the λ_2-criterion, which allows us to observe the vortex loop in the wake.

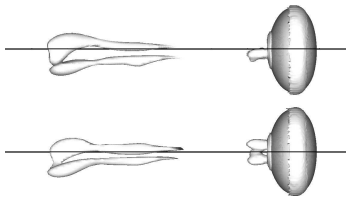

Figure 6.5: λ_2-criterion showing the vortical structure in a chaotic regime (Bubble number 2). The solid line marks the x-axis of the initial bubble position.

Zig-zag regime

In general, the zig-zag motion is characterized by a constant movement from one side to the other in a plane, a phenomenon that can be seen in Fig. 6.6(a,b), where the bubble path of this regime is plotted. The bubble follows the motion with the swinging of the shape in one direction, although without any deformations, as can be observed in Fig. 6.6(c). This unstable motion is characterized by a vortical structure that consists of two counter rotating trailing vortices, with a symmetry plane, as can be appreciated in Fig. 6.7. Moreover, the threads interleave their signs during the vortex shedding in each half-period cycle. This mode was experimentally reported by Brücker [18], Zenit & Magnaudet [183] and numerically analyzed by Mougin & Magnaudet [98, 84]. It is worth noting that the frequency decreases as the *Mo* number decreases, increasing therefore the thread length (see the Strouhal number, *St*, in table 6.1).

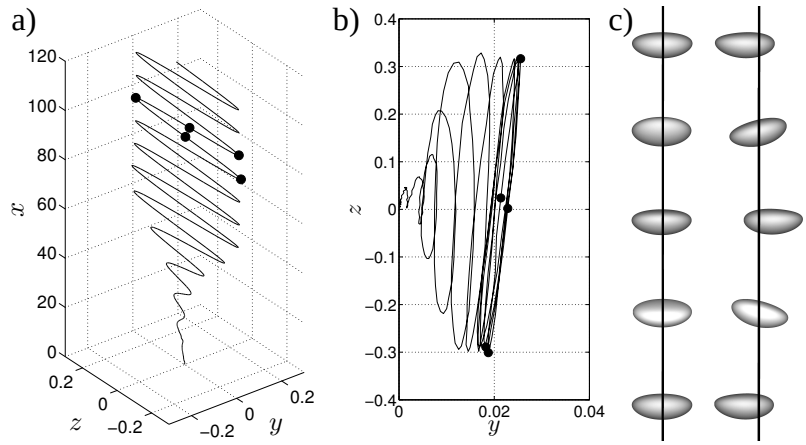

Figure 6.6: a) Three-didensional reconstruction and b) projection onto a horizontal plane, of the trajectory corresponding to a zig-zag regime (Bubble number 14). c) Temporal evolution of the bubble shape corresponding to the bullets in (a,b). The solid line marks the x-axis of the initial bubble position.

In addition, the vortical structure plotted in Fig. 6.8, shows the wake by using the $\lambda_2 < 0$ criterion, which allows the periodic visualization of the hairpin vortex shedding. This unsteady state is similar to the one reported for the sphere by [67, 109] and for the circular disk by [180, 138] by using the Q and λ_2 methods [64].

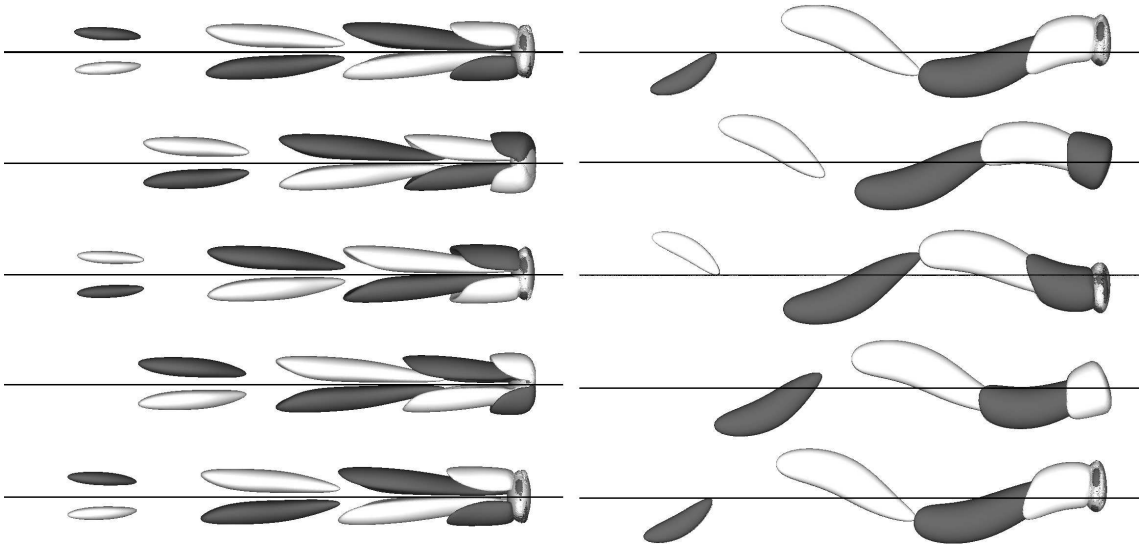

Figure 6.7: Temporal evolution of the streamwise vorticity isocontours $\omega_x D/U_T = \pm 0.24$ corresponding to the bullets shown in Fig. 6.6(a,b) for bubble number 14.

Figure 6.8: λ_2-criterion showing the vortical structure in a zig-zag regime (Bubble number 14).

Flattened spiral regime

Subsenquently to the chaotic regime, there appears an unsteady motion with flattened spiral path for low *Mo* numbers. The trajectory of this regime is plotted in Fig. 6.9(a,b), which is similar to that described in the experimental work of Veldhuis *et al.* [169], where an elliptic spiral was reported. As it occurs in the unstable case, the vortical structure is formed by two counter rotating vortices of opposite sign with small downstream instabilities, as can be seen in Fig. 6.10. The figure presents perpendicular images of the wake showing the loss of the symmetry plane, and hence distinguishing this regime from the zig-zag one. Moreover, the temporal evolution of the bubble shape shown in Fig. 6.9(c) confirms this difference.

In this mode, besides the hairpin vortices similar to those shown in the zig-zag regime, secondary vortices corresponding to the wake ondulations drawn in Fig. 6.10 are developed. The big hairpin (primary), which matches a change of a predominant direction in the path, is followed by small hairpin vortices (secondary) which can be highlighted by plotting the λ_2-criterion, Fig. 6.11. This peculiarity has been observed in spheres [127, 60] and bubbles [128, 169, 46]. These secondary vortex loops can produce oscillations at the bubble surface, thus altering the bubble shape and generating changes in the aspect ratio χ. However, the bubbles in this region, i.e. for the given

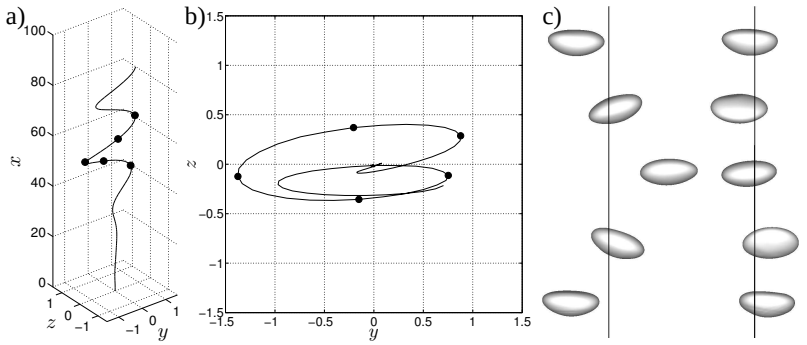

Figure 6.9: a) Three-dimensional reconstruction and b) projection onto a horizontal plane, of the trajectory corresponding to a flattened spiral regime (Bubble number 4). c) Temporal evolution of the bubble shape corresponding to the bullets in (a,b).

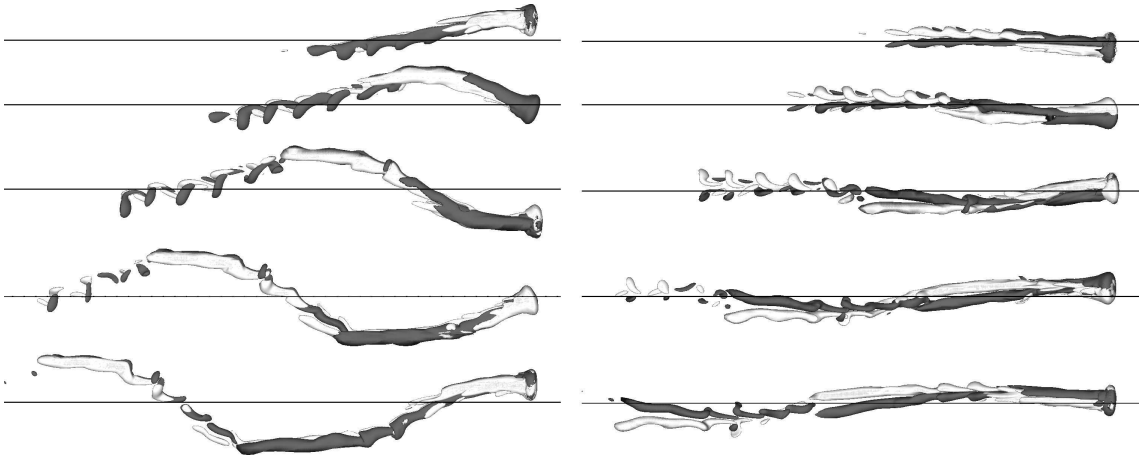

Figure 6.10: Temporal evolution of the streamwise vorticity isocontours $\omega_x D/U_T = \pm 0.24$ corresponding to the bullets shown in Fig. 6.9(a,b) for bubble number 4.

Mo and *Bo* numbers, correspond to wobbling bubbles and, therefore, oscillations at the surface are presented with their corresponding variation in the aspect ratio. A new study focusing on wobbling bubbles should be performed to determine whether the oscillations are the cause or the effect of secondary vortex shedding, or even whether the oscillations may be excited by the vortex shedding. This follows the proposal made by Lunde & Perkins [82].

In addition, it is important to highlight the good agreement between the wake and the experimental images achieved by de Vries [29] with the same *Mo* and *Bo* numbers. However, this unstable mode was called zig-zag in that study, as it presented a predominant lateral displacement in one of its planes. Furthermore, this chain of secondary hairpin vortices was experimentally reported by other authors [128, 169, 126] for low *Mo* numbers. Their experimental results agree with the numerical results discussed in this chapter.

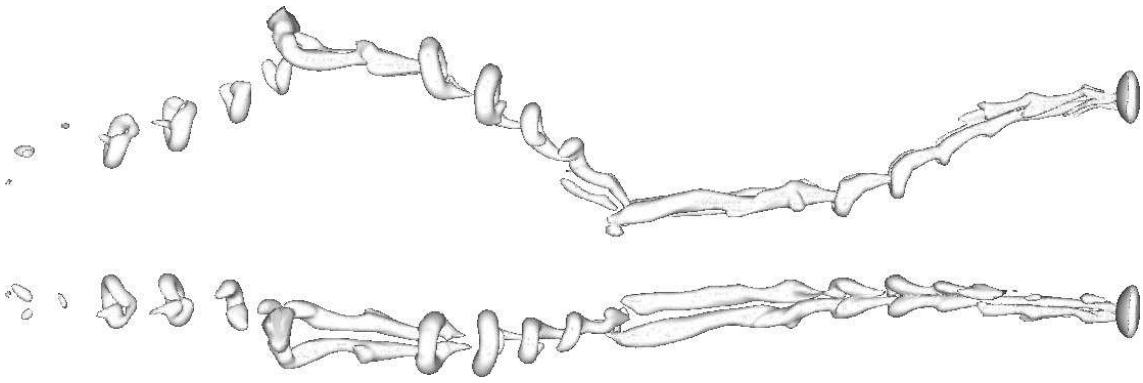

Figure 6.11: λ_2-criterion showing the vortical structure in bubble number 4.

Reflectional-Symmetry-Breaking regime

The Reflectional-Symmetry-Breaking (RSB) mode was observed and described in different studies [38, 138, 180, 7] when applied to disks with different aspect ratios ($\chi = \infty$, 10, 5 and 3). Moreover, it was also obtained for oblate spheroids by Chrust *et al.* [24]. The main characteristic of this regime is the loss of the symmetry plane being in the wake, even when the reference system is located in the bubble. This mode has not been observed in the case of a sphere [37]. In the case of a disk, the recuperation of the symmetry plane was demonstrated in the following state, called standing wave mode or Reflectional-Symmetry-Preserving (RSP). Focusing on bubbles, this mode ends in a spiral motion, as it can be seen in the paths described by the bubbles with this regime, Figs. 6.12(a,b) and 6.13(a,b). Nevertheless, it is worth noting that bubble number 12 describes an elliptic path and bubble number 18 begins with an elliptic spiral and ends with a circular spiral path, drawing a helix. Futhermore, the amplitude of the lateral movement is higher in bubble 12. Observing the bubble shapes in Figs. 6.12(c) and 6.13(c), we can appreciate the deformations experimented during the rising.

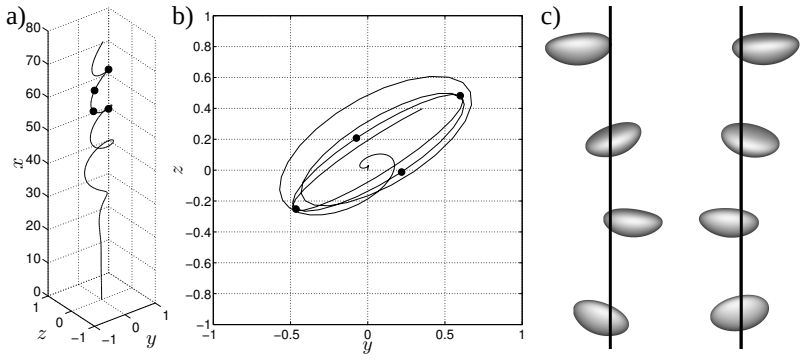

Figure 6.12: a) Three-dimensional reconstruction and b) projection onto a horizontal plane, of the trajectory corresponding to bubble number 12. c) Temporal evolution of the bubble shape corresponding to the bullets in (a,b).

The vortical structure is characterized by two streamwise intertwined vortices around themselves, producing a rotation in the bubble, Figs. 6.14 and 6.15. However, while in bubble 12 the

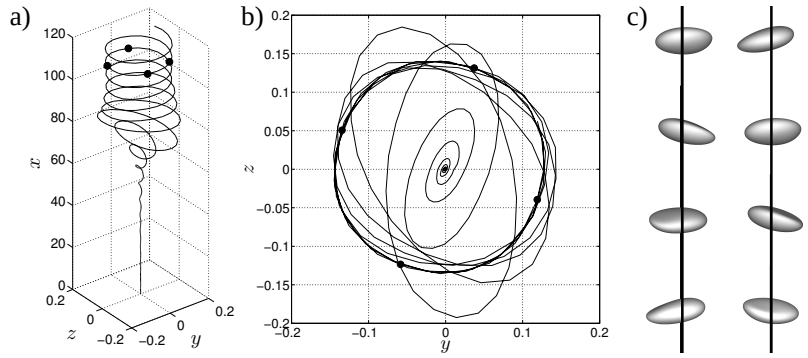

Figure 6.13: a) Three-dimensional reconstruction and b) projection onto a horizontal plane, of the trajectory corresponding to bubble number 18. c) Temporal evolution of the bubble shape corresponding to the bullets in (a,b).

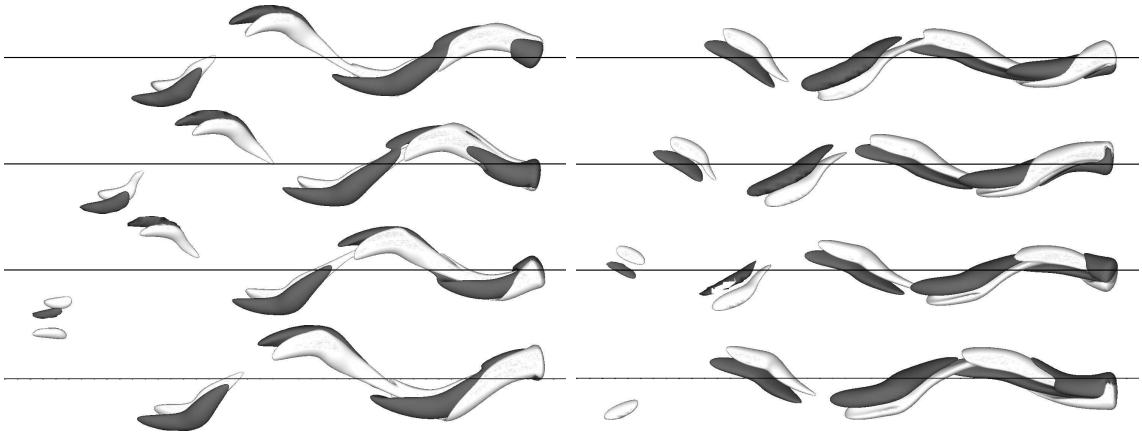

Figure 6.14: Temporal evolution of the vorticity isocontours $\omega_x D/U_T = \pm 0.24$ corresponding to bubble number 12. The positions correspond to the bullets shown in Fig. 6.12.

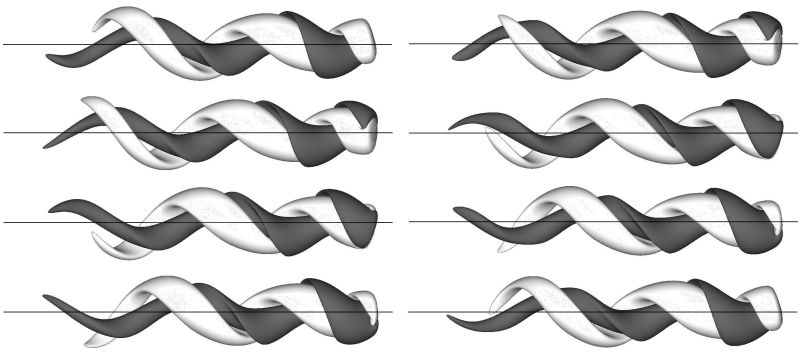

Figure 6.15: Temporal evolution of the vorticity isocontours $\omega_x D/U_T = \pm 0.24$ corresponding to bubble number 18. The positions correspond to the bullets shown in Fig. 6.13.

wake is defined by two threads spinning around the symmetry axis, see Fig. 6.16 for a clarification of the intertwining concept, bubble number 18 is identified by one thread in the inside zone with a zig-zag structure and another one with a helix structure outside, which induces a rotation in the

bubble, Fig. 6.17. In the case of bubble 12, the threads are linked by a hairpin as a consequence of the vortex shedding, which can be observed downstream. Moreover, the remaining threads are dissipated with time due to the viscosity diffusion, as it is the case in the zig-zag mode. In the other case, bubble number 18, the wake structure shown in Fig. 6.15 may be considered a frozen mode when the reference system is located in the bubble, and the rotation velocity is equal to the swirl speed of the vortical structure. It is important to highlight that the appearance of this RSB mode in a bubble rising has not been previously observed in either an experimental or a numerical way. However, the straight rocking path described in the first experimental studies [53, 8] might be assumed to be a RSB regime, which permits observing the rotation of the bubble with an apparently rectilinear motion. Figure 6.13(c) shows that the bubble rise with a small lateral motion (25% of the D) is hardly noticeable, mistaking it for a straight movement.

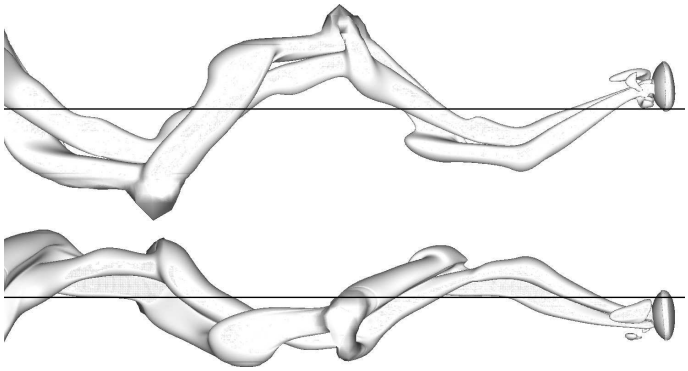

Figure 6.16: λ_2-criterion showing the vortical structure in bubble number 12.

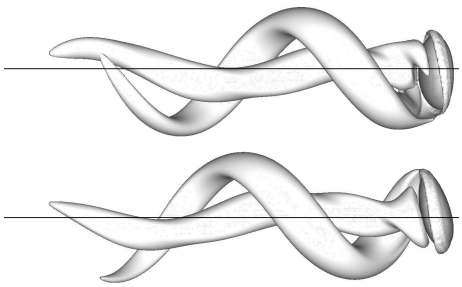

Figure 6.17: λ_2-criterion showing the vortical structure in bubble number 18.

The vortical structures obtained in this flow regime, are similar to those reported by Jiménez-González *et al.* [65, 66] when an angular velocity is applied to solid bodies. Additionally, this regime was divided into two modes: kin-knot and yin-yang, as described by Auguste *et al.* [7]. In this sense, Fig. 6.18 shows the vortical structure by using the streamwise vorticity in different planes downstream. Focusing on the left picture, the mode shown is similar to the ying-yang one [7, 37]. By contrast, the mode shown in the right picture has not been previously reported. We will call it the "corkscrew" mode, due to its wake structure shown in Fig. 6.15 & 6.17.

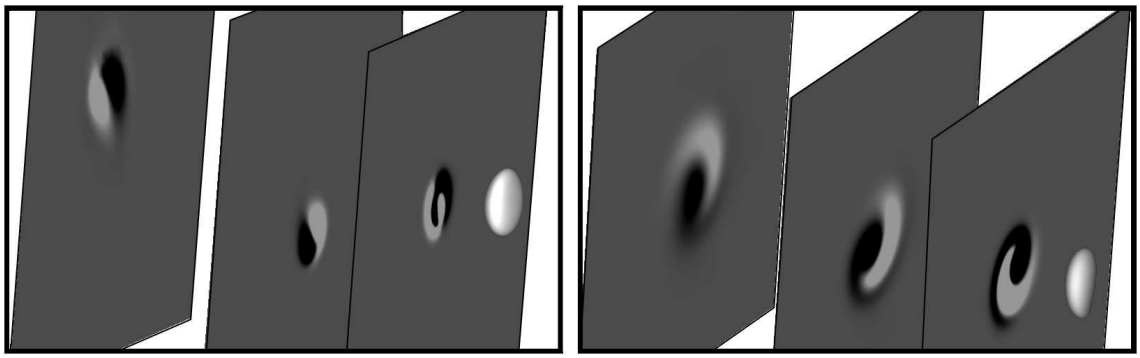

Figure 6.18: Transversal cuts plotting the streamwise vorticity $\omega_x D/U_T = \pm 0.24$ (white + and black - values) of bubble number 12 (left) and 18 (right) performed for $0.5D$, $2D$ and $4D$ of the bubble rear.

6.3.2 Terminal velocity and Reynolds number

In general, for a constant Morton number, the terminal velocity increases and then decreases as the Bond number increases, as reported in Fig. 3.3 in Chapter 3. In fact, the terminal velocity decreases due to the increment of the drag force during the transition into unstable motion [37]. However, in the case of two-dimensional simulations, where the axisymmetry boundary condition forces an axisymmetric wake, and therefore a rectilinear path, the terminal velocity decreases with the Bond number, as can be seen in Fig. 6.19, which represents the Drag coefficient $C_d = 4Re^2/3Ga^2$. The figure shows the experimental data reported by Maxworthy *et al.* [88] (black markers) and the axisymmetric simulations (white markers) for two Morton numbers $Mo = 2.174 \times 10^{-7}$ (squares) and $Mo = 1.112 \times 10^{-9}$ (circles), together with the maximum terminal velocity curve $Re/Ga = 2.14Bo^{-1} + 0.505$ defined in Chapter 3. The configuration of the axisymmetric simulations was the same as the one described in Chapter 3. In fig. 6.19 is possible to observe how, once the terminal velocity achieves its minimum C_d (maximum terminal velocity), the Drag coefficient starts to increase (terminal velocity decreases), which may be motivated by changes in the shape experimented as a function of the Bo and Mo numbers, see Chapter 4. The maximum velocity point should be the one which presents a more aerodynamic shape, i.e. the point of minimum Drag force. Thus, bubbles obtained from that point, if their Bo number increasing, will be less aerodynamics and as a consequence their terminal velocity will decrease and their C_d will increase.

Following the discussion related to the three-dimensional simulations, Fig. 6.20 shows the temporal evolution of the Reynolds number, $Re = \rho D U_T/\mu$, for the different flow regimes defined in table 6.1. In general, the different regimes begin with a rectilinear motion, as it has been previously observed in the figures describing their trajectories in subsection 6.3.1. At the end of the straight rise, the bubble reaches its maximum velocity in a short period of time, and subsequently it decreases as a consequence of the unstable motion. Only in the case of a bubble with a rectilinear path, its terminal velocity and therefore the Reynolds number, remain constant independently of time. In the rest of bubbles, once the motion is unstable, i.e. the path describes a non-straight line, the Reynolds number starts to oscillate with an amplitude dependent on the lateral shift experimented by the bubble, motivated by the vortex shedding, which is created in the bubble wake region. The case of a chaotic motion, Fig. 6.20(b), shows small oscillations due to the existence of little lateral shifts made by the bubble. In the contrary case, the bubbles which describe zig-zag

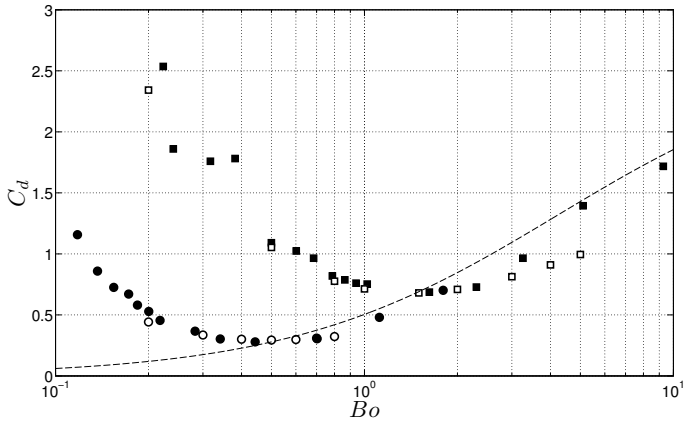

Figure 6.19: Drag evolution versus the Bo for two Morton numbers, $Mo = 2.174 \times 10^{-7}$ (squares) and $Mo = 1.112 \times 10^{-9}$ (circles), experimentally obtained by Maxworthy *et al.* [88] (solid markers) and two-dimensional numerical simulations (white markers), together with the maximum terminal velocity curve defined in Chapter 3.

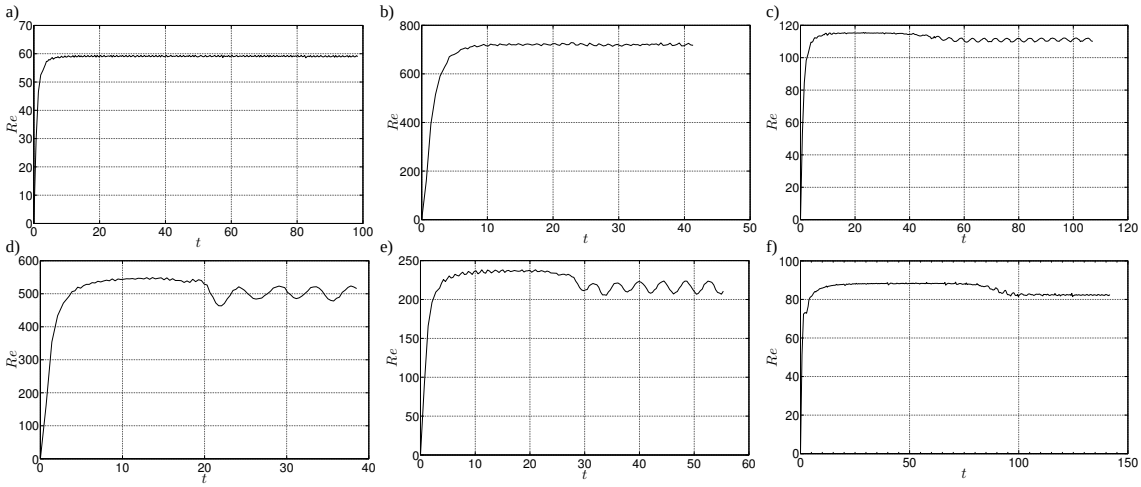

Figure 6.20: Temporal evolution of the Reynolds number for different bubbles in table 6.1. a) Rectilinear regime (Bubble n. 15), b) Chaotic regime (Bubble n. 2), c) Zig-zag regime (Bubble n. 14), d) Flattened Spiral regime (Bubble n. 9), e) and f) RSB regime (Bubbles n.12 & n.18).

or flattened spiral (elliptical spiral) motions exhibit an higher amplitude in the oscillated period caused by their lateral motion, Fig. 6.20(c,d,e). Finally, the bubbles with helix motion (circular spiral) reach a constant velocity, although such velocity is slower than that obtained in the previous stage, Fig. 6.20(f). In general, the beginning of the oscillatory period depends on the Bond number as observed in the time sequences shown in Fig. 6.20, and therefore, so does the vertical positions at which the unstable transition takes place. Moreover, these oscillatory velocities are similar to the ones experimentally shown by Aybers & Tapucu [8], Shew *et al.* [140] and numerically reported by Mougin & Magnaudet [98].

6.4 Conclusions

In this chapter, three-dimensional numerical simulations of bubbles have been performed and their behaviour during the rising in a still liquid has been assessed. Paths and wakes have been shown for different bubbles by changing the Bond and Morton numbers. The results show the following flow regimes: rectilinear, chaotic, zig-zag, flattened spiral and RSB. Furthermore, the transition to unstable motion occurs through a Hopf bifurcation, with the development of two counter rotation trailing vortices. However, the steady state reported in the LSA, Chapter 5, and by other researches [84, 3] has not been observed in the numerical results. Nevertheless, it is important to highlight that it is the first time in which the RSB regime has been applied to study the bubbles behavior. The novelty of this study lies in the fact that the RSB regime has been assessed in both the yin-yang and "corkscrew" modes. Notice that "corkscrew" mode has not been previously reported in the literature.

Analyzing the dimensionless variables, it can be observed that in the case of constant Mo numbers, the St increases with the bubble size, i.e. with the Bo number, as previously reported by [82]. Otherwise, in the case of the constant Ga number, the St increases with the Bo number too. Moreover, the numerical results coincide with the ones reported by Saffman [125]: *"The observations that the zig-zag motion occurs first and sometimes changes into the spiralling motion, whereas the spiralling motion never changes into the zig-zag motion, indicate that the spiralling motion arises from a later instability than the zig-zag motion"*. Futhermore, the results derived from this study are similar to the experimental results achieved by other researchers [157, 78]. Those studies show different paths (spiral or zig-zag) depending on the liquid properties and bubble diameter, i.e. the Bond and Morton numbers.

It is worth noting that the difficulty of experimentally observing a chaotic motion due to the small lateral shift. Therefore, the first unstable motion for low Morton numbers has always been identified with a spiral trajectory as experimentally was reported by [125, 77, 157, 78]. Moreover, the irregular mode may occur without a standing eddy, as described in Chapter 4.

In addition, the decrement of the terminal velocity in function of the bubble size has been checked to understand the bubble speed behavior, by carrying out two-dimensional axisymmetric numerical simulations. These show that the bubble velocity decreases, once obtained the maximum velocity, when increasing the Bo number, independently of the unstable motion. Moreover, the temporal evolution of the Reynolds number has also been plotted, noticing oscillations in the case of lateral movements and reaching a constant velocity in the case of a helical path.

CHAPTER
SEVEN

Conclusions and future work

7.1 General conclusions

The main purpose of this dissertation is to contribute to improve the knowledge of the bubbles dynamics behavior both, during their formation process and in their subsequent rise motion. In this sense, the study has been focused on the generation of bubbles under intermediate injection conditions, i.e. conditions where neither the gas flow rate nor the feeding pressure remain constant during the bubble formation process. Additionally, the bubble ascension motion has been analyzed numerically, characterizing the bubble shape, path and wake as functions of the fluids properties and bubble size. Thus, the neutral curve that defines the transition from a stable to an unstable ascending motion has been established by means of Linear Stability Analysis and Direct Numerical Simulations. In the following, the main conclusions and ideas developed along the present dissertation are summarized.

Initially, Chapter 2 has been devoted to analyze the bubble formation process from a submerged vertical needle under coupled conditions, both by means of experiments and theoretical analysis. The theoretical model describes the formation process including the liquid flow inside the needle during the holding stage, which contributes to increase the pressure inside the gas chamber. Furthermore, the contact angle varies throughout the holding stage as the water column moves. In general, the model predicts fairly well the temporal evolution of the chamber pressure during the generation process, and allows knowing if the weeping phenomenon occurs. In addition, the main parameters governing the bubble formation process, i.e. the chamber volume, the gas input, and the needle radius, has also been assessed to analyze their influence on the chamber pressure and the bubble size. It has been found that the pressure variations decrease and larger bubbling times are induced for increasing chamber volumes. The bubble size increases with larger chambers and for increasing gas flow rates. Regarding the influence of the needle radius, it has been observed that a monotonic bubble growth occurs for small radii, and, that for large needle radii, the pressure inside the bubble may eventually become larger than that of the chamber, inducing a reverse flow of gas from the bubble towards the chamber, therefore reducing the bubble volume before its detachment.

In Chapter 3 the bubble rising process in a stagnant liquid has been assessed, mainly focused on the terminal velocity, U_T, bubble aspect ratio, χ, also considering the effect of the gas properties on the dynamics behavior. A new correlation, given by $U_T/\sqrt{gD} = (2.14\,Bo^{-1} + 0.505)^{1/2}$, has been proposed to determine the bubble terminal velocity in the unstable region for a wide range of fluid properties and bubble sizes, based on the approximation by Clift *et al.* [25]. The same correlation,

expressed in terms of the Re, We, and Mo numbers as $Re = [We^2\,(We - 2.14)/(0.505\,Mo)]^{1/4}$, reproduces the experimental values of Re for different Mo in the unstable region. In addition, equating this correlation with that given by Rastello *et al.* [116], valid for bubbles rising with rectilinear paths, an expression for the critical Weber number, We_c, at which the transition from a rectilinear to a zig-zag motion takes place, has been also proposed, as a function of Mo, which writes $We_c^{-2/3}(We_c - 2.14) = 8.92\,Mo^{1/5}$.

Furthermore, in this chapter, two different open source solvers implementing a VOF interface-capturing technique have been used, specifically, InterFoam and Gerris Flow Solver, to evaluate the suitability of both solvers. The numerical results have shown that the terminal velocity obtained with Gerris does not vary regardless the grid resolution, whereas very different values are obtained from InterFoam. Moreover, the presence of parasitic currents is observed with InterFoam solver, being their intensity also a function of the grid resolution. Additionally, the Adaptive Mesh Refinement technique and the surface tension treatment implemented in Gerris, make this solver more suitable for the case at hand, i.e. surface tension dominated flows. Subsequently, the validated numerical method has been employed to study in detail the effects of the gas properties on the dynamics of a bubble rising in still liquid. To this aim, the effects of both, the gas density and viscosity have been analyzed by performing simulations with different gas-to-liquid density, $\lambda = \rho_g/\rho_l$, and viscosity ratios, $\beta = \mu_g/\mu_l$, to determine the differences on the bubble dynamics, their effect on the bubble shape and terminal velocity, as well as on the inner and outer velocity fields. In general, increasing values of λ and β exhibit the same features: the bubble terminal velocity decreases, it becomes more rounded, and the standing eddy formed behind the bubble becomes smaller. However very small differences have been found for the typical liquid-gas values of λ and β. Therefore, the effect of the inner gas can be neglected, that is, numerical simulations can be performed without taking into account the inner gas, with the resulting reduction of the computational time, in case only the outer liquid flow and the bubble shape are needed. This conclusion has a direct impact on the computation of the axisymmetric base flow, and bubble shape in hydrodynamic stability studies. Nevertheless, the gas density and viscosity variations have shown a strong influence on the inner flow field, which is of special importance in mass and heat diffusion processes across the interface.

Chapter 4 has been devoted to the study of the transition from rectilinear to zig-zag motion of a single bubble freely rising in a stagnant liquid, analyzing the characteristics of the wake and the final shape adopted by the bubble. The real bubble shape has been taken into account, stressing the fact that it cannot be defined only by its aspect ratio, χ, since it is possible to obtain different bubble shapes with the same aspect ratio but different fore-and-aft asymmetries, by varying the Galilei and Bond numbers. Moreover, axisymmetric simulations have been performed to determine the curve which defines the presence of a standing eddy in the bubble wake.

In addition, three-dimensional numerical simulations have been performed to determine the stability characteristics of the flow around a bubble using the shape and terminal velocity provided by the axisymmetric numerical simulations. The unstable character of the axisymmetric base flow can be associated with the development of a pair of counter-rotating vortices as suggested by Mougin and Magnaudet [98]. This transition from straight to zig-zag motion agrees with previous

experimental results. Thus, a transition curve for the development of an unstable motion has been defined as a function of the bubble aspect ratio, χ, which depends on the bubble shape, and the Reynolds number based on the bubble terminal velocity, Re. It is shown that spherical bubbles are always stable independently of Re and that the critical value of Re for which the bubble becomes unstable decreases as the aspect ratio increases. The larger critical values of Re at low χ correspond to smaller asymmetries in the bubble shape, i.e. shapes tending to spheres, as higher terminal velocities are required to deform the bubble generating azimuthal vorticity and a rotational flow field. The results differ from those reported by Magnaudet and Mougin [84], who varied the aspect ratio considering a prescribed shape for the bubble (ellipsoid of revolution). Such differences highlight the importance of obtaining the real bubble shape in order to accurately determine the transition diagram. Furthermore, the results provided by the combination of axisymmetric and three-dimensional numerical simulations also report the existence of unstable bubbles without a standing eddy in their wake, indicating that the presence of this eddy is not a necessary condition for the onset of unstable path. This bubble behavior differs from that of solid axisymmetric bluff bodies, which becomes unstable when a recirculating flow of a given length is already present behind the body. Such discrepancies are simply attributed to the different boundary conditions that prevail on the surface of the body. While a zero-shear-stress (or shear free) boundary condition is imposed on the bubble interface, a non-slip condition is present on the surface of solid bodies causing the boundary layer separation and the formation of a recirculating flow in their wake at lower Reynolds numbers. Although, according to Fig. 4.7, boundary layer separation can also take place for bubbles whose aspect ratio is larger than 1.74, the flow around a bubble may exhibit non-oscillating instabilities, without the presence of a standing eddy, caused by the transport of vorticity generated at its surface.

Later, in Chapter 5, a global Linear Stability Analysis of the wake and path of gas bubbles rising in a stagnant Newtonian liquid has been assessed focused on the effect of the real bubble shape on the stability properties. This analysis has been performed by means of a two-step approach. In the first step, the bubble shape and terminal velocity of the bubbles were obtained over a wide range of Galilei and Bond numbers from axisymmetric time-dependent numerical simulations implemented within Gerris Flow Solver. Then, the global Linear Stability Analysis has been carried out, keeping frozen the previously obtained shape, along two different scenarios. On the one hand, bubbles whose velocity and orientation were kept fixed, interacting therefore only with the fluid as fixed bodies, were considered. On the other hand, bubbles free to move and rotate were studied, which required the coupled fluid+bubble system of linearized governing equations to be solved. As in the case of spheroidal bubbles, the primary instability always occurs through a stationary bifurcation when bubbles are kept fixed. The results show that, for sufficiently large Reynolds numbers, the flow past a fixed fore-aft asymmetric bubble is significantly more stable than that past a perfectly spheroidal bubble. Hence, the fact that real bubbles with a given aspect ratio exhibit a flatter front and a more rounded rear than the corresponding oblate spheroid has been proven to stabilize the wake. In contrast, virtually no difference was found between the two geometries for Reynolds numbers below approximately 370, leaving the lower branch of the neutral curve almost unaffected by the shape asymmetry.

To be in position to perform a direct comparison with experimental results, the global Linear

Stability Analysis has been extended to freely rising bubbles with fore-aft asymmetry. As in the case of purely spheroidal bubbles, the neutral curve of the coupled fluid+bubble system was found to exhibit a much richer behavior than the fixed-bubble configuration. Indeed, the first instability arises through a Hopf bifurcation associated to a low-frequency mode ($St \approx 0.02$) at low Bond numbers (high Galilei numbers, i.e. $Ga \gtrsim 200$) and to a high-frequency mode ($St \approx 0.10$) at high Bond numbers (low Galilei numbers, i.e. $Ga = \mathcal{O}(100)$), whereas it occurs through a stationary bifurcation in the intermediate range $1.2 < Bo < 5.5$. Compared to the flow past a perfectly oblate spheroidal bubble, that past a bubble with fore-aft asymmetry has been found to be more stable for both low (typically $\lesssim 1$) and large (typically $\gtrsim 5$) Bond numbers, whereas the asymmetry does not modify its stability in the intermediate range corresponding to the stationary bifurcation. For liquids with Morton numbers of $\mathcal{O}(5\times10^{-7})$, there is a subregion in the range $4.2 < Bo < 5$ with no counterpart in the fixed-bubble configuration, where the flow becomes unstable beyond a critical Galilei number of $\mathcal{O}(110)$, then it restabilizes at slightly higher Galilei numbers until it eventually becomes unstable again beyond $Ga = \mathcal{O}(130)$ (see Fig. 5.7). Present results clearly improve over those of [151] by considering realistic bubble shapes on which the normal stress balance is satisfied everywhere as far as the flow is steady and axisymmetric. However, consistent quantitative discrepancies with respect to recent experimental data obtained in uncontaminated liquids remain, regarding critical conditions in the low- and high-Bo ranges defined above. To overcome these limitations, three-dimensional numerical simulations have been performed in Chapter 6, in which the above two restrictions are removed since the flow and the bubble shape are allowed to evolve all along the simulation.

Finally, in Chapter 6 three-dimensional Direct Numerical Simulations of bubbles have been performed analyzing their behavior as they are free to rise in still liquids. The path and wake topology have been described for different bubbles, varying the Bond and Morton numbers. The results allow to identify the following flow regimes: rectilinear, chaotic, zig-zag, flattened spiral and Reflectional-Symmetry-Breaking. Moreover, the temporal evolution of the Reynolds number has also been analyzed, observing oscillations in the cases where the bubbles suffer a lateral displacement and reaching a constant value in the case of rectilinear and helical paths. The numerical results show that the transition to unstable motion occurs through a Hopf bifurcation, with the development of two counter-rotating trailing vortices. It is important to highlight that it is the first time that the Reflectional-Symmetry-Breaking regime has been observed in the bubbles behavior, with the additional novelty that, in this regime, two different modes denoted yin-yang and "corkscrew" respectively, can manifest as a function of the flow properties. Within the unstable cases, it has been shown that, for a constant Morton number, the Strouhal number associated to the vortex shedding behind the bubble increases with the bubble size, i.e. with the Bo number. Likely, the numerical results have shown that, for a constant Ga, the Strouhal number also increases with the Bo. These simulations have helped to clarify previous experimental results where it is extremely difficult to observe a chaotic motion due to the small lateral shift suffered by the bubbles. Consequently, the first unstable regime established at low Morton numbers has always been identified with a spiral trajectory.

7.2 Future work

Despite the fact that the conclusions highlighted above provide a number of novel contributions related to the bubble formation and rising, there are many open questions that will require a future work on this fascinating topic.

In this sense, the study presented in the first part of this dissertation has been focused on the bubble formation from the experimental and analytical points of view. However, it should be interesting to numerically analyze the bubble formation process. The numerics will allow to determine the time evolution of the pressure inside the bubble and correlate it with that inside the feeding chamber for different chamber volumes. Additionally, from a numerical point of view, many work lines are also proposed: first, considering the case of bubble formation from a submerged vertical needle at constant flow rate conditions, it would be convenient to investigate the effect of the position of the contact line on the bubble shape and volume, as well as on the formation frequency. Thus, a numerical study pinning the contact line at different positions on the edge of the injection needle, or letting the contact line to freely move until an equilibrium of stresses is achieved, would help to develop models able to implement the proper boundary conditions in these types of simulations. Second, it is worth exploring numerically the bubble formation under intermediate conditions. To perform this study, the incompressible Navier-Stokes equations solved in the present numerical simulations need to be modified to allow small variations of density inside the feeding chamber. Finally, taking advantage of the numerical skills achieved during the development of the present dissertation, another interesting issue is to deeply analyze the bubble formation using a co-flow configuration. This last study is motivated by the interest of describing the pressure variations inside the bubbles during their formation period. The potential results would be used to corroborate analytical expressions previously developed by other authors [137, 51].

Additionally, changing to the experimental point of view, after characterizing the bubble size and formation frequency at intermediate conditions, nowadays it is mandatory to design new devices able to generate a large amount of bubbles of reduced size. Thus, the addition of a forcing mechanism inside the feeding chamber (for example a loud speaker) could help to generate smaller bubbles at higher frequencies. The experimental results would be complemented by numerical simulations of the process inducing pressure perturbations that would reproduce the experimental conditions.

Concerning the second part of this dissertation, where the bubble ascending motion has been analyzed, characterizing the wake topology and the bubble trajectory with the aim at defining the transition curve from stable to unstable motion, it is worth extending this work following two different paths. On the one hand, the differences observed between the Linear Stability Analysis and the experimental and numerical results suggest looking for the possible sources of discrepancy and extend the stability code to account for small variations on the bubble shape. In the present work, although the real bubble shape has been considered and the bubble has been let free to move, the shape of the bubble remains frozen without allowing small perturbations of the bubble surface. On the other hand, the study of bubble rising could be extended considering the case of CO_2 bubbles in water by means of Direct Numerical Simulations and Linear Stability Analysis.

This part of the work would be focused on the characterization of the time evolution of the bubble wake and path as the bubble rises. In this case, dissolution effects must be taken into account which induce changes in the bubble size as time evolves.

Finally, to conclude this section, an interesting aspect to explore and related to the bubble motion is to consider the case of bubbles in turbulent flows. This is a very complex problem that can be faced studying simplified cases. Thus, a simple model to describe the interaction of bubbles with the turbulent structures of the flow is to consider the interaction of a bubble with a vortex ring of a given size. Phenomenological models assume that a bubble in a turbulent flow will break if the turbulent eddies of sizes similar to that of the bubble are sufficiently energetic to overcome the confining surface tension stresses. Small vortices do not have enough energy to disturb and break the bubble and large ones would transport it without breaking it up. Thus, numerical simulations of bubbles injected in the neighbourhood of a vortex ring should help to elucidate the bubble break up mechanisms in a turbulent flow (see Martínez-Bazán [87]).

Bibliography

[1] A. Agarwal, C.F. Tai, and J.N. Chung. Unsteady development of a deformable bubble rising in a quiescent liquid. *Comput. Methods Appl. Mech. Engrg.*, 199(17-20):1080–1090, 2010.

[2] A. Albadawi, D.B. Donoghue, A.J. Robinson, D.B. Murray, and Y.M.C. Delauré. Influence of surface tension implementation in Volume of Fluid and couple Volume of Fluid with Level Set methods for bubble growth and detachment. *Int. J. Multiphase Flow*, 53:11–28, 2013.

[3] C. Albert, J. Kromer, A.M. Robertson, and D. Bothe. Dynamic behaviour of buoyant high viscosity droplets rising in a quiescent liquid. *J. Fluid Mech.*, 778:485–533, 2015.

[4] D. Antoniadis, D. Mantzavinos, and M. Stamatoudis. Effect of chamber volume and diameter on bubble formation at plate orifices. *Chem. Eng. Res. Des.*, 70:161–165, 1992.

[5] D. Arzoz, P. Rodríguez, and M. Izquierdo. Experimental study on the adiabatic absorption of water vapor into LiBr–H_2O solutions. *Appl. Therm. Eng.*, 25(5):797–811, 2005.

[6] G.H. Atefia, H. Niazmanda, and M.R. Meigounpoorya. Numerical analysis of 3D flow past a stationary sphere with slip condition at low and moderate Reynolds numbers. *J. Disp. Sci. Technol.*, 28(4):591–602, 2007.

[7] F. Auguste, D. Fabre, and J. Magnaudet. Bifurcations in the wake of a thick circular disk. *Theor. Comput. Fluid Dyn.*, 24:305–313, 2010.

[8] N.M. Aybers and A. Tapucu. The motion of gas bubble rising through stagnant liquid. *Wärme-Stoffübertragung*, 2:118–128, 1969.

[9] C.T. Barker and N. Nevers. Small-medium chamber volume boundary in the formation of bubbles. *Chem. Eng. Sci.*, 37(10):1569–1570, 1982.

[10] G.K. Batchelor. *An introduction to fluid dynamics*. Cambridge university press, 2000.

[11] E. Berberović, N.P. Van Hinsberg, S. Jakirlić, I.V. Roisman, and C. Tropea. Drop impact onto a liquid layer of finite thickness: Dynamics of the cavity evolution. *Phys. Rev. E*, 79(3):036306, 2009.

[12] D. Bhaga. *Bubbles in viscous liquids: shapes, wakes and velocities*. PhD thesis, McGill University, Montreal, 1976.

[13] D. Bhaga and M.E. Weber. Bubbles in viscous liquids: shapes, wakes and velocities. *J. Fluid Mech.*, 105:61–85, 1981.

[14] A. Blanco and J. Magnaudet. The structure of the axisymmetric high-Reynolds number flow around an ellipsoidal bubble of fixed shape. *Phys. Fluids*, 7(6):1265–1274, 1995.

[15] P. Bohorquez, E. Sanmiguel-Rojas, A. Sevilla, J. I. Jiménez-González, and C. Martínez-Bazán. Stability and dynamics of the laminar wake past a slender blunt-based axisymmetric body. *J. Fluid Mech.*, 676:110–144, 2011.

[16] R. Bolaños-Jiménez, A. Sevilla, C. Martínez-Bazán, and J.M. Gordillo. Axisymmetric bubble collapse in a quiescent liquid pool.II. Experimental study. *Phys. Fluids*, 20:112104, 2008.

[17] J.U. Brackbill, D.B. Kothe, and C. Zemach. A continuum method for modeling surface tension. *J. Comput. Phys.*, 100(2):335–354, 1992.

[18] C. Brücker. Structure and dynamics of the wake of bubbles and its relevance for bubble interaction. *Phys. Fluids*, 11(7):1781–1795, 1999.

[19] J.C. Cano-Lozano, P. Bohorquez, and C. Martínez-Bazán. Wake instability of a fixed axisymmetric bubble of realistic shape. *Int. J. Multiphase Flow*, 51:11–21, 2013.

[20] J.C. Cano-Lozano, R. Bolaños-Jiménez, C. Gutiérrez-Montes, and C. Martínez-Bazán. The use of Volume of Fluid technique to analyze multiphase flows: Specific case of bubble rising in still liquids. *Appl. Math. Model.*, 39:3290–3305, 2015.

[21] S.L. Ceccio. Friction drag reduction of external flows with bubble and gas injection. *Annu. Rev. Fluid Mech.*, 42:183–203, 2010.

[22] L. Chen, S.V. Garimella, J.A. Reizes, and E. Leonardi. The development of a bubble rising in a viscous liquid. *J. Fluid Mech.*, 387:61–96, 1999.

[23] I.-L. Chern, J. Glimm, O. McBryan, B. Plohr, and S. Yaniv. Front tracking for gas dynamics. *J. Comput. Phys.*, 62(1):83–110, 1986.

[24] M. Chrust, G. Bouchet, and J. Dušek. Parametric study of the transition in the wake of oblate spheroids and flat cylinders. *J. Fluid Mech.*, 665:199–208, 2010.

[25] R. Clift, J.R. Grace, and M.E. Weber. *Bubbles, drops and particles.* Academic Press, New York, 1978.

[26] D. Colombet, D. Legendre, A. Cockx, and P. Guiraud. Mass or heat transfer inside a spherical gas bubble at low to moderate Reynolds number. *Int. J. Heat Mass Transfer*, 67:1096–1105, 2013.

[27] B. Cuenot, J. Magnaudet, and B. Spennato. The effects of slightly soluble surfactants on the flow around a spherical bubble. *J. Fluid Mech.*, 339:25–53, 1997.

[28] J.F. Davidson and B.O.G. Schuler. Bubble formation at an orifice in an inviscid liquid. *Trans. Instn. Chem. Engrs.*, 38:335–342, 1960.

[29] A.W.G de Vries. *Path and Wake of a Rising Bubble.* PhD thesis, University of Twente, 2001.

[30] A.W.G de Vries, A. Biesheuvel, and L. Van Wijngaarden. Notes on the path and wake of a gas bubble rising in pure water. *Int. J. Multiphase Flow*, 28(11):1823–1835, 2002.

[31] S.S. Deshpande, L. Anumolu, and M.F. Trujillo. Evaluating the performance of the two-phase flow solver interFoam. *Computational Science & Discovery*, 5(1):014016, 2012.

[32] P.A. Dijkmans, L.J.M. Juffermansa, R.J.P. Mustersb, A. Wamelc, F.J. Catec, W. Gilstd, C.A. Vissera, N: Jongc, and O. Kamp. Microbubbles and ultrasound: from diagnosis to therapy. *Eur. J. Echocardiography*, 5:245–256, 2004.

[33] P.C. Duineveld. *Bouncing and coalescence of two bubbles in water.* PhD thesis, University of Twente, 1994.

[34] P.C. Duineveld. Rise velocity and shape of bubbles in pure water at high Reynolds number. *J. Fluid Mech.*, 292:325–332, 1995.

[35] P. Dzienis and R. Mosdorf. Stability of periodic bubble departures at a low frequency. *Chem. Eng. Sci.*, 109:171–182, 2014.

[36] K. Ellingsen and F. Risso. On the rise of an ellipsoidal bubble in water: Oscillatory paths and liquid-induced velocity. *J. Fluid Mech.*, 440:235–268, 2001.

[37] P. Ern, F. Risso, D. Fabre, and J. Magnaudet. Wake-induced oscillatory paths of bodies freely rising or falling in fluids. *Annu. Rev. Fluid Mech.*, 44:97–121, 2012.

[38] D. Fabre, F. Auguste, and J. Magnaudet. Bifurcations and symmetry breaking in the wake of axisymmetric bodies. *Phys. Fluids*, 20:051702, 2008.

[39] X. Fan, X. Chen, X. Liu, H. Zhang, and Y Li. Bubble formation at a submerged orifice for aluminum foams produced by gas injection method. *Metall. Mater. Trans. A*, 44a:729–737, 2013.

[40] J.Q. Feng. A spherical-cap bubble moving at terminal velocity in a viscous liquid. *J. Fluid Mech.*, 579:347–371, 2007.

[41] K. Ferrara, R. Pollard, and M. Borden. Ultrasound microbubble contrast agents: Fundamentals and application to gene and drug delivery. *Annu. Rev. Biomed. Eng.*, 9:415–447, 2007.

[42] B. Figueroa-Espinoza and D. Legendre. Mass or heat transfer from spheroidal gas bubbles rising through a stationary liquid. *Chem. Eng. Sci.*, 65(23):6296–6309, 2010.

[43] M.M. Francois, S.J. Cummins, E.D. Dendy, D.B. Kothe, J.M. Sicilian, and M.W. Williams. A balanced-force algorithm for continuous and sharp interfacial surface tension models within a volume tracking framework. *J. Comput. Phys.*, 213(1):141–173, 2006.

[44] D. Fuster, G. Agbaglah, C. Josserand, S. Popinet, and S. Zaleski. Numerical simulation of droplets, bubbles and waves: State of the art. *Fluid Dyn. Res.*, 41(6):065001, 2009.

[45] F. García-Moreno, B. Siegel, K. Heim, A.J. Meagher, and J. Banhart. Sub-mm sized bubbles injected into metallic melts. *Colloids and Surfaces A: Physicochem. Eng. Aspects*, 473:60–67, 2015.

[46] D. Gaudlitz and N.A. Adams. Numerical investigation of rising bubble wake and shape variations. *Phys. Fluids*, 21(12):122102, 2009.

[47] D. Gerlach, G. Tomar, G. Biswas, and F. Durst. Comparison of volume-of-fluid methods for surface tension-dominant two-phase flows. *Int. J. Heat Mass Transfer*, 49:740–754, 2006.

[48] B. Ghidersa and J. Dušek. Breaking of axisymmetry and onset of unsteadiness in the wake of a sphere. *J. Fluid Mech.*, 423:33–69, 2000.

[49] J. Glimm, J.W. Grove, X.L. Li, K.-M. Shyue, Y. Zeng, and Q. Zhang. Three-dimensional front tracking. *SIAM J. Sci. Comput.*, 19(3):703–727, 1998.

[50] V.R. Gopala and B.G.M. van Wachem. Volume of fluid methods for immiscible-fluid and free-surface flows. *Chem. Eng. J.*, 141:204–221, 2008.

[51] J.M. Gordillo, A. Sevilla, and C. Martínez-Bazán. Bubbling in a coflow at high Reynolds numbers. *Phys. Fluids*, 19, 2007.

[52] C. Gutiérrez-Montes, B. Bolaños-Jiménez, A. Sevilla, and C. Martínez-Bazán. Experimental and numerical study of the periodic bubbling regime in planar co-flowing air-water sheets. *Int. J. Multiphase Flow*, 50:106–119, 2013.

[53] W.L. Haberman and R.K. Morton. An experimental investigation of the drag and shape of air bubbles rising in various liquids. Technical Report 802, Navy Department. The David W. Taylor Model Basin, 1953.

[54] F.H. Harlow and J.E. Welch. Numerical calculation of time-dependent viscous incompressible flow of fluid with free surface. *Phys. Fluids*, 8(12):2182–2189, 1965.

[55] R.A. Hartunian and W.R. Sears. On the instability of small gas bubbles moving uniformly in various liquids. *J. Fluid Mech.*, 3:27–47, 1957.

[56] D.J.E. Harvie, M.R. Davidson, and M. Rudman. An analysis of parasitic current generation in Volume of Fluid simulations. *Appl. Math. Model.*, 30(10):1056–1066, 2006.

[57] F. Hecht. New development in freefem++. *Numer. Math*, 20(3-4):251–265, 2012.

[58] S. Hernot and A. L. Klibanov. Microbubbles in ultrasound-triggered drug and gene delivery. *Adv. Drug Deliv. Rev.*, 60:1153–1166, 2008.

[59] C.W. Hirt and B.D. Nichols. Volume of Fluid (VOF) method for the dynamics of free boundaries. *J. Comput. Phys.*, 39(1):201–225, 1981.

[60] M. Horowitz and C.H.K. Williamson. The effect of Reynolds number on the dynamics and wakes of freely rising and falling spheres. *J. Fluid Mech.*, 651:251–294, 2010.

[61] J. Hua and J. Lou. Numerical simulation of bubble rising in viscous liquid. *J. Comput. Phys.*, 222(2):769–795, 2007.

[62] R.R. Hughes, A.E. Handlos, H.D. Evans, and R.L. Maycock. The formation of bubbles at simple orifices. *Ind. Eng. Chem. Res.*, 51:557–563, 1955.

[63] D. Jamet, D. Torres, and J.U. Brackbill. On the theory and computation of surface tension: The elimination of parasitic currents through energy conservation in the second-gradient method. *J. Comput. Phys.*, 182(1):262–276, 2002.

[64] J. Jeong and F. Hussain. On the identification of a vortex. *J. Fluid Mech.*, 285:69–94, 1995.

[65] J.I. Jiménez-González, E. Sanmiguel-Rojas, and C. Martínez-Bazán. Laminar flow past a spinning bullet-shaped body at moderate angular velocities. *J. Fluids Struct.*, 43:200–219, 2013.

[66] J.I. Jiménez-González, A. Sevilla, E. Sanmiguel-Rojas, and C. Martínez-Bazán. Global stability analysis of the axisymmetric wake past a spinning bullet-shaped body. *J. Fluid Mech.*, 748:302–327, 2014.

[67] T.A. Johnson and V.C. Patel. Flow past a sphere up to a Reynolds number of 300. *J. Fluid Mech.*, 378:19–70, 1999.

[68] A.M. Khokhlov. Fully Threaded Tree Algorithms for Adaptive Refinement Fluid Dynamics Simulations. *J. Comput. Phys.*, 143(2):519–543, 1998.

[69] A.K. Khurana and R. Kumar. Studies in bubble formation - III. *Chem. Eng. Sci.*, 24(11):1711–1723, 1969.

[70] J. Klostermann, K. Schaake, and R. Schwarze. Numerical simulation of a single rising bubble by VOF with surface compression. *Int. J. Numer. Meth. Fluids*, 71(8):960–982, 2013.

[71] A.A. Kulkarni and J.B. Joshi. Bubble formation and bubble rise velocity in gas-liquid systems: A review. *Ind. and Eng. Chem. Res.*, 44(16):5873–5931, 2005.

[72] I. Kumagai, Y. Takahashi, and Y. Murai. Power-saving device for air bubble generation using a hydrofoil to reduce ship drag: Theory, experiments, and application to ships. *Ocean Eng.*, 95:183–194, 2015.

[73] B. Lafaurie, C. Nardone, R. Scardovelli, S. Zaleski, and G. Zanetti. Modelling and merging and fragmentation in multiphase flows with surfer. *J. Comput. Phys.*, 113(1):134–147, 1994.

[74] R.D. LaNauze and I.J. Harris. Gas bubble formation at elevated system pressures. *Trans. Instn. Chem. Engrs.*, 52:337–348, 1974.

[75] D. Legendre, E. Lauga, and J. Magnaudet. Influence of slip on the dynamics of two-dimensional wakes. *J. Fluid Mech.*, 633:437–447, 2009.

[76] D. Legendre, R. Zenit, and J.R. Velez-Cordero. On the deformation of gas bubbles in liquids. *Phys. Fluids*, 24(6):043303, 2012.

[77] J.T. Lindt. On the periodic nature of the drag on a rising bubble. *Chem. Eng. Sci.*, 27(10):1775–1781, 1972.

[78] L. Liu, H. Yan, and G. Zhao. Experimental studies on the shape and motion of air bubbles in viscous liquids. *Exp. Therm. Fluid Sci.*, 62:109–121, 2015.

[79] X. Liu, Y. Li, and X. Chen. Bubble size control during the gas injection foaming process in aluminum alloy melt. *J. Mater. Res.*, 30:1002–1010, 2015.

[80] X. Liu, Y. Li, X. Chen, Y. Liu, and X. Fan. Foam stability in gas injection foaming process. *J. Mater. Sci.*, 45:6481–6493, 2010.

[81] K. Lunde and R.J. Perkins. Observations on wakes behind spheroidal bubbles and particles. *In: Proceedings of ASME Fluids Engineering Division Summer Meeting FEDSM 97, FEDSM97-3530.*, 1997.

[82] K. Lunde and R.J. Perkins. Shape oscillations of rising bubbles. *Appl. Sci. Res.*, 58(1-4):387–408, 1998.

[83] J. Magnaudet and I. Eames. The motion of high-Reynolds number bubbles in inhomogeneous flows. *Annu. Rev. Fluid Mech.*, 32:659–708, 2000.

[84] J. Magnaudet and G. Mougin. Wake instability of a fixed spheroidal bubble. *J. Fluid Mech.*, 572:311–337, 2007.

[85] A. Marmur and E. Rubin. A theoretical model for bubble formation at an orifice submerged in an inviscid liquid. *Chem. Eng. Sci.*, 31(6):453–463, 1976.

[86] M. Martín, F.J. Montes, and M.A. Galán. Numerical calculation of shapes and detachment times of bubbles generated from a sieve plate. *Chem. Eng. Sci.*, 61:363–369, 2006.

[87] C. Martínez-Bazán. About bubbles and vortex rings. *J. Fluid Mech.*, 780:1–4, 2015.

[88] T. Maxworthy, C. Gnann, M. Kürten, and F. Durst. Experiments on the rise of air bubbles in clean viscous liquids. *J. Fluid Mech.*, 321:421–441, 1996.

[89] D.J. McCann and R.G.H. Prince. Bubble formation and weeping at a submerged orifice. *Chem. Eng. Sci.*, 24:801–814, 1969.

[90] D.J. McCann and R.G.H. Prince. Regimes of bubbling at a submerged orifice. *Chem. Eng. Sci.*, 26(10):1505–1512, 1971.

[91] S. Mckee, M.F. Tomé, V. G. Ferreira, J.A. Cuminato, A Castelo, F.S. Sousa, and N. Mangiavacchi. The MAC method. *Comput. Fluids*, 37:907–930, 2008.

[92] D.I. Meiron. On the stability of gas bubbles rising in an inviscid fluid. *J. Fluid Mech.*, 198:101–114, 1989.

[93] H.D. Mendelson. The prediction of bubble terminal velocities from wave theory. *AIChE J.*, 13:250–253, 1967.

[94] D.W. Moore. The rise of a gas bubble in a viscous liquid. *J. Fluid Mech.*, 6(1):113–130, 1959.

[95] D.W. Moore. The boundary layer on a spherical gas bubble. *J. Fluid Mech.*, 16(2):161–176, 1963.

[96] R. Mosdorf and T. Wyszkowski. Experimental investigations of deterministic chaos appearance in bubbling flow. *Int. J. Heat Mass Transfer*, 54:5060–5069, 2011.

[97] G. Mougin and J. Magnaudet. The generalized Kirchhoff equations and their application to the interaction between a rigid body and an arbitrary time-dependent viscous flow. *Int. J. Multiphase Flow*, 28(11):1837–1851, 2002.

[98] G. Mougin and J. Magnaudet. Path instability of a rising bubble. *Phys. Rev. Lett.*, 88(1):145021–145024, 2002.

[99] K. Mukundakrishnan, S. Quan, D.M. Eckmann, and P.S. Ayyaswamy. Numerical study of wall effects on buoyant gas-bubble rise in a liquid-filled finite cylinder. *Phys. Rev. E*, 76(3):036308, 2007.

[100] S. Muzaferija and M. Perić. Computation of free surface flows using interface-tracking and interface-capturing methods. In O. Mahrenholtz and M. Markiewicz, editors, *Nonlinear water waves interaction*. Computational Mechanics Publications, Southampton, 1998.

[101] I. Nakamura. Steady wake behind a sphere. *Phys. Fluids*, 19(1):5–8, 1976.

[102] H.N. Oguz and A. Prosperetti. Dynamics of bubble growth and detachment from a needle. *J. Fluid Mech.*, 257:111–145, 1993.

[103] C.D. Ohl, A. Tijink, and A. Prosperetti. The added mass of an expanding bubble. *J. Fluid Mech.*, 482:271–290, 2003.

[104] M. Ohta, T. Imura, Y. Yoshida, and M. Sussman. A computational study of the effect of initial bubble conditions on the motion of a gas bubble rising in viscous liquids. *Int. J. Multiphase Flow*, 31(2):223–237, 2005.

[105] E. Olsson and G. Kreiss. A conservative level set method for two phase flow. *J. Comput. Phys.*, 210(1):225–246, 2005.

[106] Y. Park, A.L. Tyler, and N. de Nevers. The chamber orifice interaction in the formation of bubbles. *Chem. Eng. Sci.*, 32(8):907–916, 1977.

[107] J.E. Pilliod Jr. and E.G. Puckett. Second-order accurate volume-of-fluid algorithms for tracking material interfaces. *J. Comput. Phys.*, 199(2):465–502, 2004.

[108] W. Pinczewski. The formation and growth of bubbles at a submerged orifice. *Chem. Eng. Sci.*, 36(2):405–411, 1981.

[109] P. Ploumhans, G.S. Winckelmans, J.K. Salmon, A. Leonard, and M.S. Warren. Vortex Methods for Direct Numerical Simulation of Three-Dimensional Bluff Body Flows: Application to the Sphere at Re = 300, 500, and 1000. *J. Comput. Phys.*, 178:427–463, 2002.

[110] S. Popinet. Gerris: A tree-based adaptive solver for the incompressible Euler equations in complex geometries. *J. Comput. Phys.*, 190(2):572–600, 2003.

[111] S. Popinet. An accurate adaptive solver for surface-tension-driven interfacial flows. *J. Comput. Phys.*, 228(16):5838–5866, 2009.

[112] S. Popinet and S. Zaleski. A front-tracking algorithm for accurate representation of surface tension. *Int. J. Numer. Meth. Fluids*, 30(2):775–793, 1999.

[113] A. Prosperetti. Bubbles. *Phys. Fluids*, 16(6):1852–1865, 2004.

[114] A. Prosperetti, C.D. Ohl, A. Tijink, G. Mougin, and J. Magnaudet. Leonardo's paradox. Appendix to C. D. Ohl, A. Tijink and A. Prosperetti. *J. Fluid Mech.*, 482:286–289, 2003.

[115] S. Ramakrishnan, R. Kumar, and N.R. Kuloor. Studies in bubble formation-I. Bubble formation under constant flow conditions. *Chem. Eng. Sci.*, 24(4):731–747, 1969.

[116] M. Rastello, J.-L. Marié, and M. Lance. Drag and lift forces on clean spherical and ellipsoidal bubbles in a solid-body rotating flow. *J. Fluid Mech.*, 628:434–459, 2011.

[117] Y. Renardy and M. Renardy. Prost: A parabolic reconstruction of surface tension for the Volume-of-Fluid method. *J. Comput. Phys.*, 183(2):400–421, 2002.

[118] W.J. Rider and D.B. Kothe. Reconstructing volume tracking. *J. Comput. Phys.*, 141(2):112–152, 1998.

[119] J. Rodríguez-Rodríguez, A. Sevilla, C. Martínez-Bazán, and J.M. Gordillo. Generation of microbubbles with applications to industry and medicine. *Annu. Rev. Fluid Mech.*, 47:405–29, 2015.

[120] J. Rubio, M.L. Souza, and R.W. Smith. Overview of flotation as a wastewater treatment technique. *Miner. Eng.*, 15:139–155, 2002.

[121] H. Rusche. *Computational fluid dynamics of dispersed two-phase flows at high phase fractions*. PhD thesis, Imperial College, University of London, 2002.

[122] M.C. Ruzicka and R.B. Drahos. Meniscus dynamics in bubble formation. Part I: Experiment. *Chem. Eng. Res. Des.*, 87:1349–1356, 2009.

[123] G. Ryskin and L.G. Leal. Numerical solution of free-boundary problems in fluid mechanics. Part 2. Buoyancy-driven motion of a gas bubble through a quiescent liquid. *J. Fluid Mech.*, 148:19–35, 1984.

[124] A. Saboni, S. Alexandrova, A. M. Spasic, and C. Gourdon. Effect of the viscosity ratio on mass transfer from a fluid sphere at low to very high Peclet numbers. *Chem. Eng. Sci.*, 62(17):4742–4750, 2007.

[125] P.G. Saffman. On the rise of small air bubbles in water. *J. Fluid Mech.*, 1(3):249–275, 1956.

[126] T. Saito and M. Toriu. Effects of a bubble and the surrounding liquid motions on the instantaneous mas transfer across the gas-liquid interface. *Chem. Eng. J.*, 265:164–175, 2015.

[127] H. Sakamoto and H. Haniu. A study on wortex shedding from spheres in a uniform flow. *J. Fluids Eng.*, 112:386–392, 1990.

[128] T. Sanada, M. Shirota, and M. Watanabe. Bubble wake visualization by using photochromic dye. *Chem. Eng. Sci.*, 62(24):7264–7273, 2007.

[129] T. Sanada, M. Shirota, S. Yokojima, and S. Takagi. Drag force acting on an ellipsoidal bubble with fore-aft asymmetry. *Japanese J. Multiphase Flow*, 24(5):523–530, 2010.

[130] T. Sanada, K. Sugiara, M. Shirota, and M. Watanabe. Motion and drag of a single bubble in super-purified water. *Fluid Dyn. Res.*, 40:534–545, 2008.

[131] E. Sanmiguel-Rojas, A. Sevilla, C. Martínez-Bazán, and J.-M. Chomaz. Global mode analysis of axisymmetric bluff-body wakes: stabilization by base bleed. *Phys. Fluids*, 21:144102, 2009.

[132] M. Sano and K. Mori. Bubble formation from single nozzles in liquid metals. *Trans. Jpn. Inst. Met.*, 17:344–52, 1976.

[133] A. Sato. *Deformation, wake and collision of rising bubbles.* PhD thesis, Kyushu University, 2009.

[134] A. Satyanarayan, R. Kumar, and N.R. Kuloor. Studies in bubble formation-II. Bubble formation under constant pressure conditions. *Chem. Eng. Sci.*, 24(4):749–761, 1969.

[135] R. Scardovelli and S. Zaleski. Direct numerical simulation of free-surface and interfacial flow. *Annu. Rev. Fluid Mech.*, 31:567–603, 1999.

[136] J.A. Sethian and P. Smereka. Level Set methods for fluid interfaces. *Annu. Rev. Fluid Mech.*, 35:341–72, 2003.

[137] A. Sevilla, J.M. Gordillo, and C. Martínez-Bazán. Transition from bubbling to jetting in a coaxial air-water jet. *Phys. Fluids*, 17:018105, 2005.

[138] A.R. Shenoy and Kleinstreuer. Flow over a thin circular disk at low to moderate Reynolds numbers. *J. Fluid Mech.*, 605:253–262, 2008.

[139] W.L. Shew and J.-F. Pinton. Dynamical model of bubble path instability. *Phys. Rev. Lett.*, 97(14):144508, 2006.

[140] W.L. Shew, S. Poncet, and J.-F. Pinton. Force measurements on rising bubbles. *J. Fluid Mech.*, 569:51–60, 2006.

[141] D. Sipp and A. Lebedev. Global stability of base and mean flows: a general approach and its applications to cylinder and open cavity flows. *J. Fluid Mech.*, 593:333–358, 2007.

[142] M. Stöhr, J. Schanze, and A. Khalili. Visualization of gas-liquid mass transfer and wake structure of rising bubbles using pH-sensitive PLIF. *Exp. Fluids*, 47(1):135–143, 2009.

[143] M. Sussman. A Level Set Approach for Computing Solutions to Incompressible Two-Phase Flow. *J. Comput. Phys.*, 114:146–159, 1994.

[144] M. Sussman, E. Fatemi, P. Smereka, and S. Osher. An improved level set method for incompressible two-phase flows. *Comput. Fluids*, 27:663–680, 1998.

[145] Y. Tagawa, S. Takagi, and Y. Matsumoto. Surfactant effect on path instability of a rising bubble. *J. Fluid Mech.*, 738:124–142, 2014.

[146] S. Takagi and Y. Matsumoto. Surfactant effects on bubble motion and bubbly flows. *Annu. Rev. Fluid Mech.*, 43:615–636, 2011.

[147] R.B.H. Tan and I. Harris. A model for non-spherical bubble growth at a single orifice. *Chem. Eng. Sci.*, 41(12):3175–3182, 1986.

[148] J. Tchoufag, D. Fabre, and J. Magnaudet. Global linear stability analysis of the wake and path of buoyancy-driven disks and thin cylinders. *J. Fluid Mech.*, 740:278–311, 2014.

[149] J. Tchoufag, D. Fabre, and J. Magnaudet. Weakly nonlinear model with exact coefficients for the fluttering and spiraling motion of buoyancy-driven bodies. *Phys. Rev. Lett.*, 115:114501, 2015.

[150] J. Tchoufag, J. Magnaudet, and D. Fabre. Linear stability and sensitivity of the flow past a fixed oblate spheroidal bubble. *Phys. Fluids*, 25:054108, 2013.

[151] J. Tchoufag, J. Magnaudet, and D. Fabre. Linear instability of the path of a freely rising spheroidal bubble. *J. Fluid Mech.*, 751, 2014.

[152] K. Terasaka, J. Oka, and H. Tsuge. Ammonia absorption from a bubble expanding at a submerged orifice into water. *Chem. Eng. Sci.*, 57:3757–3765, 2002.

[153] K. Terasaka and H. Tsuge. Bubble formation at a single orifice in high viscous liquids. *J. Chem. Eng. Japan*, 23(2):160–165, 1990.

[154] A. Tezuka and K. Suzuki. Three-dimensional global linear stability analysis of flow around a spheroid. *AIAA J.*, 44(8):1697–1708, 2006.

[155] A. Theodorakakos and G. Bergeles. Simulation of sharp gas-liquid interface using VOF method and adaptive grid local refinement aroung the interface. *Int. J. Numer. Meth. Fluids*, 45(4):421–439, 2004.

[156] V. Theofilis. Global linear instability. *Annu. Rev. Fluid Mech.*, 43:319–352, 2011.

[157] A. Tomiyama, G.P. Celata, S. Hosokawa, and S. Yoshida. Terminal velocity of single bubbles in surface tension force dominant regime. *Int. J. Multiphase Flow*, 28(9):1497–1519, 2002.

[158] A.Y. Tong and Z. Wang. A numerical method for capillarity-dominant free surface flows. *J. Comput. Phys.*, 221(2):506–523, 2007.

[159] M.K. Tripathi, K.C. Sahu, and R. Govindarajan. Dynamics of an initially spherical bubble rising in quiescent liquid. *Nat. Commun.*, 6(6268), 2015.

[160] G. Tryggvason, B. Bunner, A. Esmaeeli, D. Juric, N. Al-Rawahi, W. Tauber, J. Han, S. Nas, and Y.-J. Jan. A front-tracking method for the computations of multiphase flow. *J. Comput. Phys.*, 169:708–759, 2001.

[161] G. Tryggvason, R. Scardovelli, and S. Zaleski. *Direct Numerical Simulations of Gas-Liquid Multiphase Flows*. Cambridge University Press, 2011.

[162] H. Tsuge and S. Hibino. Bubble formation from a submerged single orifice accompanied by pressure fluctuations in gas chamber. *J. Chem. Eng. Japan*, 11(3):173–178, 1978.

[163] H. Tsuge and S.I. Hibino. The onset conditions of oscillatory motion of single gas bubble rising in various liquids. *J. Chem. Eng. Japan*, 10:66–68, 1977.

[164] H. Tsuge, Y. Nakajima, and K. Terasaka. Behavior of bubbles formed from a sumerged orifice under high system pressure. *Chem. Eng. Sci.*, 47:3273–3280, 1992.

[165] Ž. Tuković and H. Jasak. A moving mesh finite volume interface tracking method for surface tension dominated interfacial fluid flow. *Comput. Fluids*, 55:70–84, 2012.

[166] S.O. Unverdi and G. Tryggvason. A Front-Tracking Method For Viscous, Incompressible, Multi-fluid flows. *J. Comput. Phys.*, 100:25–37, 1992.

[167] M. Van Sint Annaland, N.G. Deen, and J.A.M. Kuipers. Numerical simulation of gas bubbles behaviour using a three-dimensional volume of fluid method. *Chem. Eng. Sci.*, 60(11):2999–3011, 2005.

[168] G. Černe, S. Petelin, and I. Tiselj. Numerical errors of the volume-of-fluid interface tracking algorithm. *Int. J. Numer. Meth. Fluids*, 38(4):329–350, 2002.

[169] C. Veldhuis, A. Biesheuvel, and L. van Wijngaarden. Shape oscillations on bubbles rising in clean and in tap water. *Phys. Fluids*, 20(4):040705, 2008.

[170] C.H.J. Veldhuis. *Leonardo's paradox: Path and shape instabilities of particles and bubbles*. PhD thesis, University of Twente, 2007.

[171] M. Venegas, M. Izquierdo, P. Rodríguez, and A. Lecuona. Heat and mass transfer during absorption of ammonia vapour by $LiNO_3$–NH_3 solution droplets. *Int. J. Heat Mass Transfer*, 47(12):2653–2667, 2004.

[172] Verfürth. Finite element approximation of incompressible Navier-Stokes equations with slip boundary condition II. *Numer. Math*, 59:615–636, 1991.

[173] J.P. Wang, A.G.L. Borthwick, and R.E. Taylor. Finite-volume-type VOF method on dynamically adaptive quadtree grids. *Int. J. Numer. Meth. Fluids*, 45(5):485–508, 2004.

[174] P.P. Wegener and J.-Y. Parlange. Spherical-cap bubbles. *Annu. Rev. Fluid Mech.*, 5:79–100, 1973.

[175] M. Wu and M. Gharib. Experimental studies on the shape and path of small air bubbles rising in clean water. *Phys. Fluids*, 14(7):L49–L52, 2002.

[176] Z.Y. Xiao. *Bubble formation and bubble-wall interaction at a submerged orifice*. PhD thesis, National university of Singapore, 2004.

[177] Z.Y. Xiao and R.B.H. Tan. An improved model for bubble formation using the boundary-integral method. *Chem. Eng. Sci.*, 60:179–186, 2005.

[178] S. Xie and R.B.H. Tan. A model for bubble-bubble and bubble-wall interaction in bubble formation. *Chem. Eng. Sci.*, 58:4639–4647, 2003.

[179] B. Yang and A. Prosperetti. Linear stability of the flow past a spheroidal bubble. *J. Fluid Mech.*, 582:53–78, 2007.

[180] J. Yang, G. Wu, W. Zhong, and M. Liu. Numerical study on bifurcations in the wake of a circular disk. *Int. J. Comput. Fluid D.*, 28:187–203, 2014.

[181] D.L. Youngs. *Time-dependent multi-material flow with large fluid distortion.* In: Morton, K.W. and Bianes, M.J. (Eds.), Numerical Methods for Fluid Dynamics. Academic Press, New York, pp. 273-285, 1982.

[182] R. Zenit and J. Magnaudet. Path instability of rising spheroidal air bubbles: A shape-controlled process. *Phys. Fluids*, 20(6):061702, 2008.

[183] R. Zenit and J. Magnaudet. Measurements of the streamwise vorticity in the wake of an oscillating bubble. *Int. J. Multiphase Flow*, 35(2):195–203, 2009.

[184] J. Zhang and M.-J. Ni. Direct simulation of single bubble motion under vertical magnetic field: Paths and wakes. *Phys. Fluids*, 26:102102, 2014.

[185] W. Zhou and J. Dušek. Chaotic states and order in the chaos of the paths of freely falling and ascending spheres. *Int. J. Multiphase Flow*, 75:205–223, 2015.